U.H.F. RADIO ECHO SOUNDING OF YUKON GLACIERS

by

BRIAN BARRY NAROD

B.Sc., University of British Columbia, 1970

M.Sc., University of British Columbia, 1975

A THESIS SUBMITTED IN PARTIAL FULFILLMENT OF

THE REQUIREMENTS FOR THE DEGREE OF

DOCTOR OF PHILOSOPHY

in

THE FACULTY OF GRADUATE STUDIES

(Department of Geophysics and Astronomy)

We accept this thesis as conforming

to the required standard

THE UNIVERSITY OF BRITISH COLUMBIA

June, 1979

In presenting this thesis in partial fulfilment of the requirements for an advanced degree at the University of British Columbia, I agree that the Library shall make it freely available for reference and study. I further agree that permission for extensive copying of this thesis for scholarly purposes may be granted by the Head of my Department or by his representatives. It is understood that copying or publication of this thesis for financial gain shall not be allowed without my written permission.

Department of GEOPHYSICS & ANSTRONOMY

The University of British Columbia
2075 Wesbrook Place
Vancouver, Canada
V6T 1W5

Date June 25, 1979

Frontispiece. An aerial fisheye photograph taken over the Hazard Glacier. These photographs provide flight line control. The surface drainage feature seen in this photograph is visible on a government aerial photograph taken at 15,000 m elevation. The location of this photograph is marked by an asterisk on Figure A2.2.


0345

ABSTRACT

A high-resolution radio echo sounder operating at a frequency of 840 MHz has been developed for sounding of small and medium-sized polar glaciers and ice caps. The sounder uses a compact, high-gain antenna which improves the system performance, suppresses valley wall echoes and simplifies operation from light aircraft. Successful field trials were carried out on the Rusty, Trapridge and Hazard Glaciers, Yukon Territory, Canada.

Results of airborne surveys compare well with ice depths obtained from earlier ground-based soundings on the Rusty and Trapridge Glaciers. The maximum ice thickness encountered was 200 m on Hazard Glacier. Owing to the high operating frequency, random scattering from inhomogeneities within the ice is a major cause of signal degradation. For this reason the sounder cannot penetrate great thicknesses of temperate or debris-rich ice. Spatial averaging, an immediate result of operating from a moving platform, reduces the effects of back-scattered "clutter."

Results of ground-based tests on the Hazard Glacier yield a value for $f \tan \delta = 0.26$ at $-5^{\circ}C$, in agreement with predicted values. The total received power and the echo details have both been found to be very sensitive to small (<10 cm) changes in antennae position. Large fluctuations in power, caused by roughness at or near the ice/air surface, prevented using single coverage data to detect birefringence in glacier ice.

The results also indicate that the standard photographic records should be replaced by a recording medium capable of

storing more precise and accessible data. A storage medium such as magnetic tape should not degrade the radar data, and would at the same time relieve a data processing burden.

TABLE OF CONTENTS

LIST OF TABLES

LIST OF FIGURES

ACKNOWLEDGEMENTS

I wish to thank Dr. G. K. C. Clarke for his support of this project and for his invaluable assistance during all phases of the field trials.

I thank the National Research Council of Canada, Environment Canada and the University of British Columbia Committee on Arctic and Alpine Research for financial support. The system development was financed by National Research Council grants 67-3479 and 67-3809. Dr R. H. Goodman was generous with his time and advice. I am grateful to Parks Canada for allowing this work to be undertaken in Kluane National Park. While conducting the aerial surveys we were based at the Kluane Research Station of the Arctic Institute of North America; (I thank the Institute for logistic support extending over many field seasons.)

I thank P. Cary for his assistance during the 1975 Yukon field test. I thank Dr. S. G. Collins and J. G. Napoleoni for their assistance during the 1976 field work.

The U.B.C. computing centre supported the production of the thesis typescript.

I thank Dr. E. Hutchings for his editorial assistance.

CHAPTER 1: INTRODUCTION

This thesis is concerned with the development of Ultra High Frequency (UHF) radars for the purpose of echo sounding polar ice masses. The work reported here includes the development at U.B.C. of an 840 MHz radio echo sounder and the results of field tests made during the 1976 field season.

This chapter includes a brief background to UHF echo sounding as well as a description of the project development and the field work. Chapter 2 describes the radar developed at U.B.C. as well as the procedures and results of airborne tests. Appendix 1 is a complete technical description of the system. Chapter 3 with Appendix 3 describes the results of attempts to use the sounder to study glacier ice fabric and intraglacial structures. Chapter 4 summarizes the results and considers how to improve future experiments.

This research was motivated primarily by the desire to develop a radio echo sounder optimized for ice depths typically expected in the Canadian Arctic. Of particular interest were the cold valley glaciers of the northern St. Elias Mountains, and the ice caps of the Arctic Archipelago, although our field work did not include the latter area. Valley glaciers have sufficiently different flow characteristics from the more commonly studied ice caps, that we also wished to develop a technique for monitoring their physical properties. Features of interest included glacial properties such as bedrock roughness, and the distributions of scattering objects, layers and conduit systems (Clough, 1977; Harrison, 1973; Smith and Evans, 1972). Ice fabric properties included possible strain alignment of

optical axes and stress induced optical(R.F.) anisotropy (Campbell, and Orange, 1974; Johari, and Jones, 1975).

A high resolution UHF radar offered both an ice depth measurement capability for Arctic glaciers as well as a potential sensitivity to physical properties of glaciers. A wavelength in air of about 30 cm would make possible the use of high gain aperture antennae as well as simplifying the execution of most surface experiments. A wavelength in ice of about 20 cm would make a radar sensitive to effects caused by smaller variations in bedrock roughness, intraglacial structures, and crystallographic properties than those variations detectable at longer wavelengths.

Although instrumentation design and development were the most time-consuming parts of this research, the motivation was primarily glaciological. For this reason the detailed system description and operating manual are relegated to the appendix. The results presented here demonstrate the usefulness of UHF radio echo sounders for the study of glaciers.

1.1 BACKGROUND

The behaviour of UHF (300 MHz-3 GHz) electromagnetic waves in large ice masses and the utility of UHF radio echo sounding have received relatively little investigation compared with radio echo sounding in the lower VHF (30-300 MHz) band. Greater dielectric losses and higher susceptibility to scattering have limited the usefulness of UHF sounders on large polar ice sheets, the first regions of extensive radio echo sounding. Waite (1966), using an SCR-718 440 MHz aircraft altimeter in

northwest Greenland, reported loss of signal at depths exceeding 400 m. VHF sounders have no difficulty sounding ice many times this thickness. On small and medium-sized valley glaciers, valley-wall reflections and aircraft manoeuvrability, rather than ice penetration depth, are the main considerations; thus the small size and directivity of UHF antennae become attractive.

In 1970 on Roslin Gletscher, Davis and others (1973) used a UHF sounder to measure ice thicknesses in a cold valley glacier. Man-hauling a modified SCR 718 radio altimeter they were able to measure ice thicknesses up to 400 m; all previous soundings using the SCR 718 had been made on polar ice caps. They reported that scattered returns at many locations often made identification of a distinct bottom echo difficult (Smith and Evans, 1972).

The first UHF radar designed strictly as an ice depth sounder was a 620 MHz instrument built for the Department of the Environment of Canada (DOEC) by Goodman (1975). Results of man-hauled surveys of the Rusty and Trapridge Glaciers demonstrated that the DOEC system was capable of finer resolution than existing VHF systems, and that valley wall echoes and rapidly varying bedrock topography did not seriously affect the sounder's performance. As with the SCR 718, internal scatterers could have made the identification of a distinct bottom echo ambiguous.

Sondergaard and Skou (1976) using a 6 Kw, 300 MHz radar have reported some successes with airborne sounding of the Greenland Ice Cap, however as an ice depth measurement tool it

lacks the penetration of their 60 MHz system.

Bogorodskii has operated a 700 MHz system with a range limit of about 300 m (Bentley, 1979).

1.2 PROGRAM DEVELOPMENT

In 1973 we began development of a radio echo sounder for use in northern Canada. The need to operate on small glaciers dictated the sounder's properties. We chose 840 MHz in the ultra high frequency (UHF) band as the centre frequency for several reasons. Although dielectric losses and random scattering increase with frequency, a high-gain antenna can offset much of the loss; the small size of an UHF antenna simplifies airborne operation. Most Canadian polar ice masses are expected to be within the maximum range of an UHF sounder (Narod, unpublished).

The system development took place at U.B.C. We completed the system specifications in 1974, and completed the first working version of the sounder in the spring of 1975. The receiver, antennae, power supply, intercom and camera intervalometer were all designed at U.B.C. The transmitter design and fabrication were completed by Microwave Control Co., New Jersey, U.S.A.

We proposed several experiments, each designed to test the capability and limitations of the new sounder. By working with two antennae on a glacier surface we hoped to detect birefringence in the glacier ice. We felt that the short wavelength (20 cm in ice) would facilitate this test because the relatively small antennae (1.5 m) would be easily manipulated.

Using a single antenna we proposed to operate the system

from light aircraft. These flight tests would measure the sounder's ability to penetrate both polar and temperate ice. Two other aspects of these tests would be the determination of the interfering effects of valley walls, and the problems associated with operating aerial surveys in small valleys and in other areas where very precise flight line control is necessary. Photographic data records were to be used for all tests.

The first field trial took place in May, 1975 on the Athabasca Glacier, Alberta, Canada. The test was terminated early as a result of a failure of the transmitter high voltage supply, but not before we observed a very high level of returning scattered power.

Further preliminary field trials took place during June and July, in the St. Elias Mountains, Yukon Territory, Canada. Results of tests carried out on the surface of the Rusty Glacier prompted modifications to the antennae and to the transmitter trigger circuit. Airborne tests were carried out from a Hughes 500 helicopter. These resulted in modifications to the video amplifier. The 1975 flight tests were made without flight line control.

A final flight check, prior to the 1976 field work, took place in early August, in the Vancouver, Canada area. Operating from a Cessna 180 aircraft a successful systems check was performed with the modified radar, a new intercom and a flight line camera. The test was simply a hardware check, and although the flight included passes over several temperate glaciers no internal echoes were detected.

1.3 FIELD WORK

In August 1976 we tested the sounder on glaciers in the St. Elias Mountains, Yukon Territory, Canada. The field work took two forms, airborne sounding, and glacier physics experiments.

The airborne experiments took place primarily on three glaciers in the Steele Creek basin. Extensive glaciological work had previously been done on two of these glaciers, the Rusty and Trapridge, so the thermal regime and ice depth were known at a number of sites; a network of survey markers provided ground control points. To get similar information about Hazard Glacier we set up a field camp and carried out a levelling survey, ground-based experiments with the radar, hot-water drilling and ice temperature measurements. Later in August, using a Bell 206 helicopter, we did the aerial surveys of these glaciers.

The glacier physics experiments took place at our camp on the Hazard Glacier at drill site #1 (Appendix 2). These experiments involved rotating a receiver antenna about a vertical axis for one of two orthogonal transmitter antenna orientations. These experiments were designed to recover the ellipses of polarizaton of reflections from scattering objects and from the bedrock. The ellipses would provide information about anisotropy within the ice and about depolarization due to scattering (Beckmann and Spizzichino, 1963).

It is worth noting here that the instant photography used for data recording would not allow for any analysis in the field, and hence the quality of the data gathered from the Hazard Glacier surface could not be effectively judged there.

On the other hand, the instant photography was very successful at indicating data quality during the airborne tests. There the task mainly required the detection of a bedrock echo, a far simpler task than analysing an entire waveform. Oswald (1975) has also commented on the difficulty with which he used photographic records for statistical analyses.

The motivation for using frame by frame photography was two-fold. Photography is an easily acquired technique for recording broadband data both continuously and instantaneously. Also, other investigators have had a long history of using photographic recording (Robin, 1975; Gudmandsen and others, 1976). We were guided to some extent by their experience.

CHAPTER 2: AIRBORNE SOUNDING OF GLACIERS

The University of British Columbia (UBC) radio echo sounder, which is similar in concept to the DOEC system, has been specifically designed to sound the smaller polar glaciers and ice caps found in northern Canada (Narod, unpublished). Its centre frequency is 840 MHz, bandwidth 40 MHz and system performance is 124 dB. The 35% increase in frequency over that of the DOEC system brings increased susceptibility to internal scattering and higher dielectric losses, but these drawbacks are offset by the high gain and small size of the antenna and the ease with which the entire system is made airborne. Surface echograms demonstrate that scattering returns vary greatly with minute changes in antenna position (Bailey and others, 1964). By moving the antenna while continuously recording, (Fig. 2.1) the relatively constant bottom echo can be identified among the highly variable scattering returns. When airborne, the scattering returns vary too rapidly to be visible on an oscilloscope phosphor.

2.1 INSTRUMENTATION

The UBC echo sounder comprises a transmitter, receiver, circulator, antenna and oscilloscope display. Table 2.1 lists relevant system parameters; complete system details are included in Appendix 1. The system performance of the radar transceiver (transmitter, receiver and circulator) is 124 dB. Adding the two-way antenna gain of 31 dB, the effective system performance is 155 dB. Both the transmitter and receiver are internally

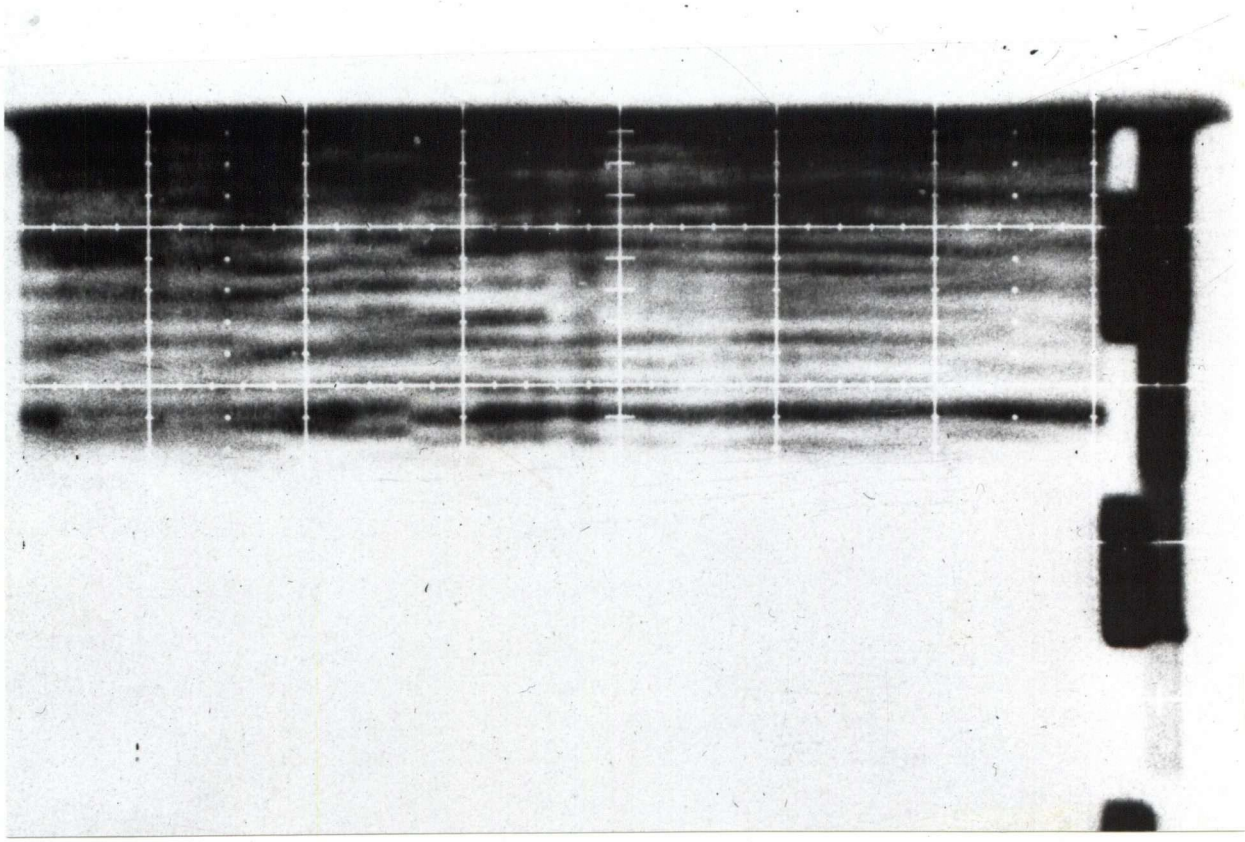

Figure 2.1 A Continuous Echogram From Hazard Glacier Surface

A continuous echogram taken on the surface, near drill site 1 on Hazard Glacier, showing significant scattered power returning both before and after the dominant bottom echo. This record was made by rotating the antenna 360° around a vertical axis. The bit code at the left is a system-generated data identifier (see Appendix 1.3).

protected against abnormal power surges caused by cable failures. A 120 MHz signal from a crystal oscillator is

Table 2.1 System Description And Parameters

Transmitter: Gated dual microwave cavity triode amplifier. Frequency is set by crystal.

Power	4.1 Kw peak rms (+66 dBm)
Pulse length & rate	50 ns at 10 KHz
Rise time	18 ns
Fall time	28 ns

Receiver: Thin film solid state hybrid. Logarithmic response.

Bandwidth	40 MHz
Intermediate frequency	120 MHz
Dynamic range	80 dB
Sensitivity	-70 dBm
System losses	12 dB
	(including I.F. conversion loss)

T/R Switch:	Passive circulator
Isolation	25 dB
1 dB Bandwidth	>40 MHz

Antenna: Two dipole colinear array with a third parasitic element and a 90° corner reflector.

1 dB Bandwidth	>40 MHz
VSWR	1.14
Forward gain	15.5 dB ± 1 dB
Depth	0.30 m
Width	0.59 m
Length	1.18 m
Weight	9 Kg

General: Total system weight	50 Kg
Power required	28V @ 10A
Estimated maximum range in cold ice	650 m

multiplied to 720 MHz and 840 MHz to provide the local oscillator and carrier frequencies respectively. The carrier is then amplified, gated and isolated at the 4 Kw level. The circulator is a three-port ferrite device which allows the system to operate with a single antenna. The receiver input is protected by a solid-state limiter. The signal is converted to

the 120 MHz intermediate frequency and filtered. The I.F. amplifier-detector has a logarithmic response characteristic with a useful dynamic range of 80 dB.

The antenna is a 90° corner reflector with two driven dipole elements. Its measured forward gain is 15.5±1.0 dB. The estimated E-plane and H-plane half power beamwidths are 18° and 44° respectively. The antenna is compact enough to be attached to the cargo hook of any helicopter with high skid gear. On our August 1976 flights we outrigged the antenna from the helicopter, in an experimental installation (Fig. 2.2).

The video output from the receiver modulates the phosphor intensity of a Tektronix model 475 oscilloscope. A slow ramp on the vertical input scans the trace through the full screen height in one minute. The operator manually controls the vertical scan and a Polaroid-backed oscilloscope camera records the data. This results in approximately 20% dead time. (We recommend that in future the photographic recording system be replaced by a magnetic recorder or graphic recorder and are, in fact, developing such a system.)

2.2 SURVEY PROCEDURE

As well as the arrival time of the bed echo, useful sounding data require knowledge of aircraft position and ground clearance. The UBC sounder, when used as its own radio

---

Overleaf: Figure 2.2. The UBC radio echo sounder antenna installed on a Bell 206 helicopter.

altimeter, receives a strong echo from the ice surface. It is necessary, however, to fly at least 40 m above the ice surface in order to separate the transmitted pulse from the first received pulse. The small dynamic range of the phosphor and film cause this limitation. An improved recording system could reduce the minimum required elevation to less than 25 m above the ice surface. Alternately, flying as close to the surface as possible, the pilot can use visual references (survey markers, etc.) to control his elevation and maintain a constant clearance above the ice surface. The advantage of the latter procedure is a greater signal-to-noise ratio (Swithinbank, 1968). Its disadvantages are several: reduced air speed, reduced accuracy (the pilot cannot maintain a perfectly constant height above the surface; we have estimated our low level height at 6±2 m) and poor flight-line photography--not to mention discomfort due to air sickness and increased risk of crashing. Data for Rusty Glacier were collected from high elevation (Figs. 2.3 and 2.4); data from the Trapridge Glacier were collected from both high and low elevations; data from the Hazard Glacier were collected only at low elevation.

For flight line records we used a combination of dead reckoning and aerial photography. A tape recording of the aircraft intercom was verbally synchronized with the data collection. Navigation information included compass headings, airspeeds, and visual references. Aerial photography with a 210°-coverage fisheye lens was also synchronized with the data collection. Our intention was to take photographs every 10 s, which, when compared to large-scale photographs, would provide

locations and headings (frontispiece). Unfortunately photographic flight control was incomplete due to erratic behaviour of the motor-driven Nikon camera caused by aircraft vibrations (the camera has now been replaced by a 70 mm Vinten aerial reconnaissance camera).

2.2.1 FLIGHT LINE ANALYSIS

Verbal references to airspeed and aircraft heading are recoverable with a timing accuracy of several seconds. Since these values change relatively slowly, more precise timing is not needed. References to visual cues such as stakes located in the glacier can be referenced to the data with an accuracy of about 1 second. With typical airspeeds of 40-60 Km hr^{-1} (10-15 m s^{-1}) on the Hazard Glacier and Rusty Glacier and less on the Trapridge Glacier along-path plan accuracy can be kept to less than 50 m.

Across-path dead reckoning tolerances are determined by the

Overleaf; Figure 2.3. The flight path of the profile reproduced in Figure 2.4. The region shown is at 61°15'N, 140°20'W.

Second overleaf: Figure 2.4. Cross-section of the Rusty Glacier showing photographically-recorded data. The small circles at the ice surface represent the centre line survey stakes. The larger circles at the bedrock boundary indicate the ice depths measured with the DOEC system (Clarke and Goodman, 1975). Vertical exaggeration is 4:1. The data records show clear separation of the transmitted pulse, ice surface reflection and ice bottom reflection, even over ice as thin as 30 m. The dark vertical bars are synchronizing marks with the 35 mm camera or with verbal cues recorded on the flight recorder. The vertical scale is 500 ns $division^{-1}$. Data for the cross-section were compiled from two passes of identical plan and overlapping profile (one not shown).

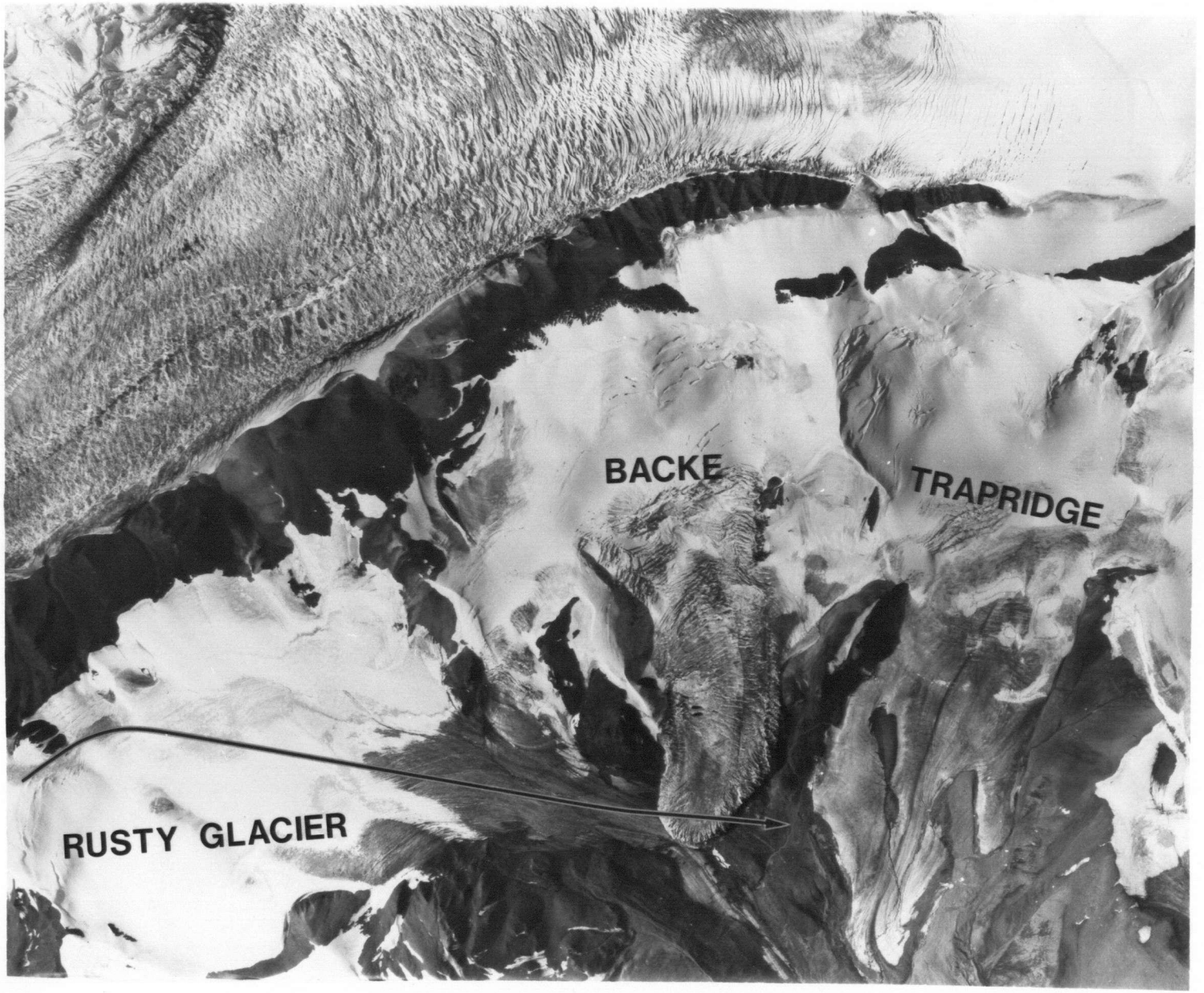
BACKE
TRAPRIDGE
RUSTY GLACIER

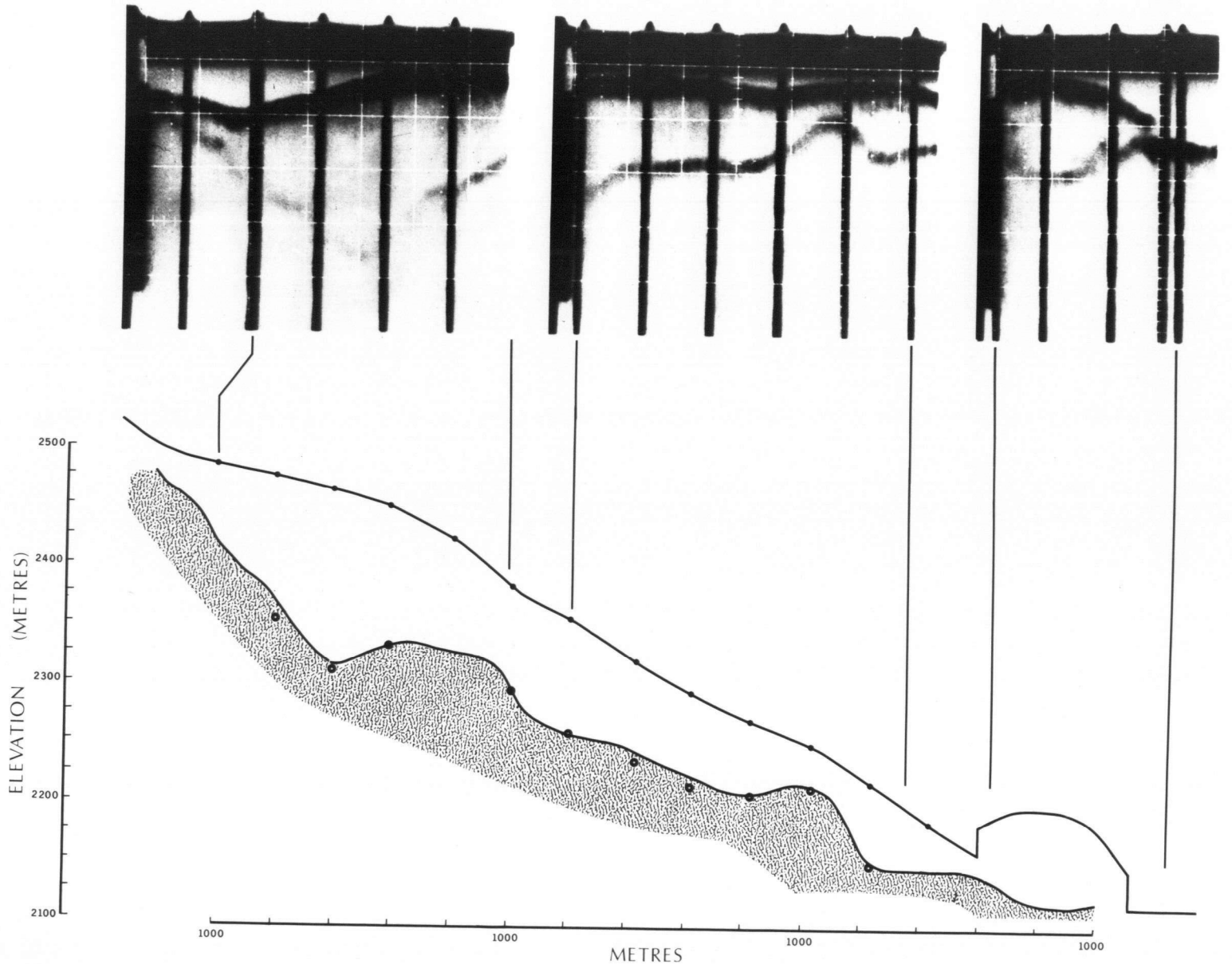
2500
2400
2300
2200
2100
ELEVATION (METRES)
1000
1000
1000
1000
METRES

accuracy of compass and visual cue references. Headings were referred from the aircraft magnetic compass. We found an apparent systematic discrepancy of 12° between observed headings and headings plotted on aerial photographs using all available information. This difference can be accounted for by considering several possible sources of error (Table 2.2). Values for aircraft deviation were provided by the chartering airline. Magnetized materials in the radio echo sounder (isolator and circulator) introduce deviation. Rosette error refers to our inability to match our ground survey coordinate system to parallax-affected large scale aerial photos. Cartesian error refers to our inability to orient the aerial photo with respect to published maps of the area. Distortion error refers to nonlinearities introduced by photographic enlargement optics. However, the accepted flight lines are well tied to visual references. Across path plan accuracy from dead reckoning has been estimated at better than 50 m.

The best quality flight line control came from the fisheye flight line photography. These photographs provided tie points accurate to about 10 m (the drainage feature in the frontispiece is approximately 10 m across).

We have estimated our overall plan accuracy at better than 50 m for accepted data.

2.3 RESULTS

The profile of the Rusty Glacier presented in Figures 2.3 and 2.4, except for crossing the terminus of the Backe Glacier at the lower end, follows the centre line of survey markers down

Table 2.2 Compass Errors

	Typical	Maximum
To Be Explained	12°	
Aircraft Deviation	2°	5°
Introduced Deviation*		5°
Rosette Error	3°	
Cartesian Error		4°
Distortion Error		1°
Reading Error		5°

* Tests for this value were performed in Vancouver, Canada. The survey area was much further north, possibly within the area of compass unreliability. The actual value thus may be larger.

the glacier. The profile is in excellent agreement with an earlier survey made by man-hauling the DOEC system (Clarke and Goodman, 1975). For ready comparison with this work we have taken 176 m us^{-1} as the velocity of electromagnetic waves in ice. At the ten locations where direct comparison is possible seven of the measured ice depths agree within the resolution of the system. The remaining three discrepancies, all less than 10 m, have been attributed to a deviation of the flight path near the headwall, or to difficulties of interpretation of ground survey data. It is also possible that the airborne system could yield data implying shallower ice, since it illuminates a larger area of the bedrock.

The Rusty Glacier profile demonstrates several features of the echo sounder. Resolution (about 4 m or one-tenth of a

graticule division) is currently limited by the photographic recording scheme. The averaging effect of the photographic film suppresses scattering returns since each grain is exposed by the accumulated output of over 1000 transmitter pulses.

Data for the ice thickness map of Trapridge Glacier (Fig. 2.5) were compiled from three of the four flights made during the two days, resulting in more extensive coverage than on the Rusty Glacier. The Trapridge Glacier also has an array of survey markers useful during the flights as visual navigation aids. Again, where it is possible to compare the airborne ice thickness measurements with those made from the surface with the DOEC system (Goodman and others, 1975), agreement is very good, within the resolution limit of the present airborne system.

There are a number of features in the new ice thickness map that were not indicated by the ground survey data. A shallow rib extends from the northern edge, about half way up the glacier, across the glacier towards an icefall. This zone of shallow ice may split the glacier into two separate dynamic zones. The major rock ridge which splits the terminus extends under the ice about one-third of the way up the glacier. A basin of ice has been found between the two rock spurs near the centre of the headwall. The new features are consistent with the ground survey

---

Overleaf: Figure 2.5. Trapridge Glacier ice thickness map. The contours are computer generated by interpolating from the airborne data onto an arbitrary square grid. The interpolation uses an inverse-distance-squared weighted average of the nearest datum in each of eight equal sectors. In regions of low density coverage and particularly near the southwest headwall, the map reflects the arbitrary nature of the interpolation scheme.


Headwall
Ice fall
10
20
30
40
50
60
70
80
90
100
110
N
1 KM
TRAPRIDGE GLACIER
RADIO ICE DEPTH
in metres

data and are results of the more extensive coverage of our airborne programme.

The most serious limitation of the sounder is its inability to penetrate great thicknesses of temperate or debris-rich ice. We believe the ice thickness map of Hazard Glacier (Fig. 2.6) owes much of its character to an internal moraine layer formed by the merging of the glacier's two main tributaries. The map shows, along the northern edge of the glacier, a shallow ledge of relatively constant (60-80 m) ice depth. The boundary of the ledge is defined by a tortuous 80 m ice depth contour. We do not believe that in this region we have actually measured total ice depth. More likely the radiation has been scattered by the internal moraine layer.

The evidence for an internal reflector is two-fold. Each transverse flight line yielded data showing an extremely steep rise from the "deeper" southern region of the glacier to the northern ledge (Fig. 2.7). These very strong boundary points do

---

Overleaf: Figure 2.6. Hazard Glacier ice thickness map. The contour interval is 20 m. The major medial moraine is shown as a shaded area.

Second overleaf: Figure 2.7. A transverse section of the Hazard Glacier showing the interpretation and a reproduction of the data. The cross-section is shown looking up-glacier, with the northern boundary to the right. The solid line represents the first interpretation of the data. The flight line shown on Figure 2.6, went from the northern boundary to the southern boundary. The steep rise coincides with the edge of the major medial moraine. The shallow ledge depicted by the solid line above a shaded band is probably not bedrock but a debris layer, perhaps brought with overlain ice from the northern arm of the glacier. The dashed line represents a hypothetical bedrock surface.

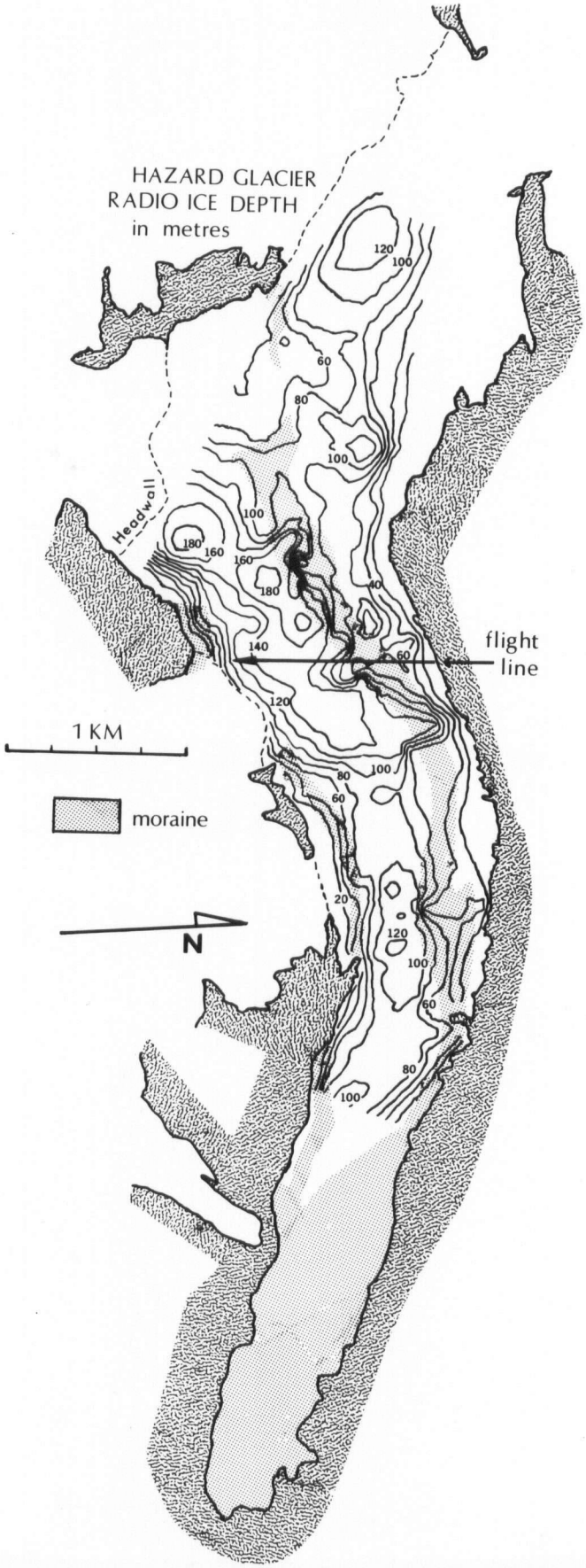
HAZARD GLACIER
RADIO ICE DEPTH
in metres
Headwall
flight
line
1 KM
moraine
N

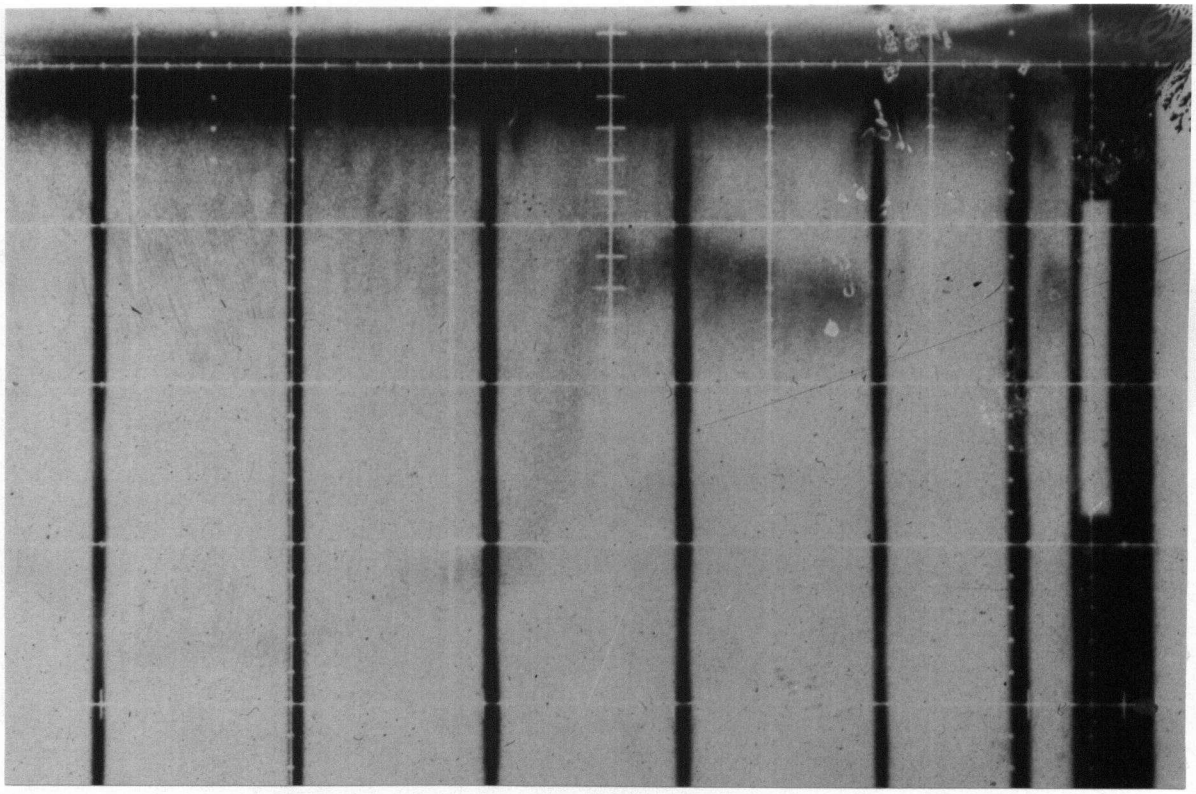

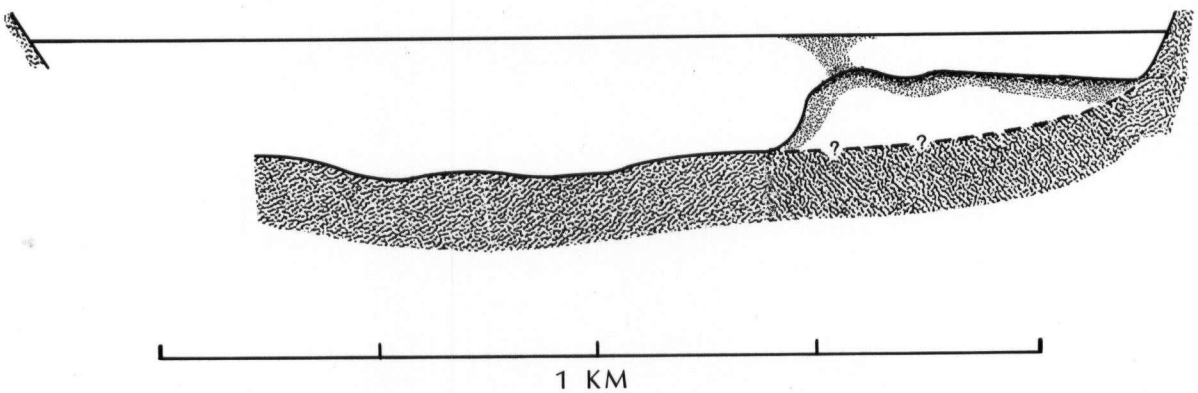
?
?
1 KM

not define a smooth valley floor. Instead they cause the tortuous 80 m contour in Figure 2.6. We believe that the rises are too steep for a reasonable valley configuration and that the irregular contours result from the occasional penetration of the radiation through the internal layer. Secondly, the edge of the shallow ice depths coincides with the major surface medial moraine. The structure which has caused the formation of the medial moraine could also have caused the formation of an internal moraine layer which terminates in the vicinity of the medial moraine. Possibly ice from the northern arm has overridden ice which originated at the southern headwall (Sharp, 1960, p. 13).

2.4 CONCLUDING REMARKS TO AIRBORNE SURVEYS

Our field tests demonstrate that airborne UHF echo sounders can be used to measure the ice thickness of small and medium-sized cold valley glaciers. The compact size of the antenna and instruments makes them easily deployable from even the smallest aircraft. Using a small helicopter, complete ice thickness data can be collected quickly and efficiently. The deepest ice encountered was 200 m on Hazard Glacier, though this is not the depth limit of our sounder. During an airborne survey of the glacier lying in the northwest col of Mt. Logan, Yukon Territory, we sounded 430 m of ice under conditions that were far from ideal (Clarke and Narod, unpublished). The major drawback of UHF echo sounders is their inability to penetrate temperate or dirty ice.

Several improvements to the sounder are now being

undertaken: these include the organization of the radar into a single rack-mounted package for easier airborne deployment, increased pre-amplification for improved system performance, addition of a graphic display for monitoring and field replay, a magnetic recorder for digital or analogue data, and direct recording navigation aids.

CHAPTER 3: PHYSICAL PROPERTIES OF GLACIERS

3.1 EXPERIMENTAL DESCRIPTION

The experiments performed with the UBC sounder at our Hazard Glacier field camp (drill site #1) were designed to measure ellipses of polarization of reflected power, and to gather statistical data on reflection strengths. The data discussed here are the products of two experiments which have for convenience been labelled experiment TX.0 and experiment TX.9.

The physical execution of the experiments involved the rotation of a receiver antenna about the vertical axis, while a transmitter antenna was left stationary. For TX.0 the E-vector of the transmitter antenna was aligned approximately parallel to the flow axis of the glacier. For TX.9 the E-vector of the transmitter was aligned at a right angle to the TX.0 orientation, approximately perpendicular to the flow axis of the glacier (Fig. 3.1).

Two high-gain corner reflector antennae (App. 1.5) were used for these experiments. Because of their small size we were able to mount the antennae on rotating platforms, levelled approximately 60 cm above the ice surface.

For each experiment we recorded 36 echograms, taken at 10° increments of the receiver antenna azimuth. We made a total of 72 records by photographing an A-scope (X-Y) oscilloscope display on Polaroid film.

We then digitized these records on a "Gradicon" flatbed digitizer. This digitizer has a precision of 0.001" (0.025 mm). The digital records were numerically interpolated to 10 ns increments, and corrected for trace rotation on the flatbed digitizer. A final time base correction brought the leading edges of the transmitted pulses into alignment (Figs. 3.2 and 3.3).

3.2 DATA ANALYSIS

The intent of the two experiments was to establish a quasi-stationary EM field with the stationary transmitter antenna, and then to use the receiver antenna as an analyser of the reflected field. If the returning power were linearly polarized we should expect to detect a $\cos^2$ variation of power with azimuth. The two-fold symmetry of the receiver antenna pattern implies that we should expect always to have a two-fold symmetry in the returned power vs. azimuth. Nonpolarized returning power should result in the measurement of a circular power distribution. Our data show little evidence for any of these effects.

3.2.1 ERRORS IN POWER MEASUREMENTS

PROCESSING ERRORS

The photographic/digitizing procedure introduces errors which could have been avoided had a more sophisticated recording medium been easily available.

Due to cathode ray tube writing speeds the photographic process cannot deliver uniform image density (brightness) along the trace. Together with the finite width of the oscilloscope trace, this can result in substantial timing/power errors since the user must visually select valid points along the trace. In our case an optimally sharp trace had a width corresponding to approximately 100 ns or 1.5 dB.

The digitizing process can also contribute to timing/power errors. A precision in our case of 0.001" (0.025 mm) corresponds to 2.5 ns or 0.04 dB, and is hence not a significant error source. However user imprecision and fatigue could introduce errors many times larger. We kept sessions at the digitizer to less than 1 hour to minimize this problem.

Time base correction values were taken from points sampled

Overleaf: Figure 3.1. Schematic of the plan views of the antenna rotation experiments.

Second overleaf: Figure 3.2 the 36 records for experiment TX.0. The numbers to the left of each record indicate the receiver azimuth in degrees.

Third overleaf: Figure 3.3. The 36 records of experiment TX.9.

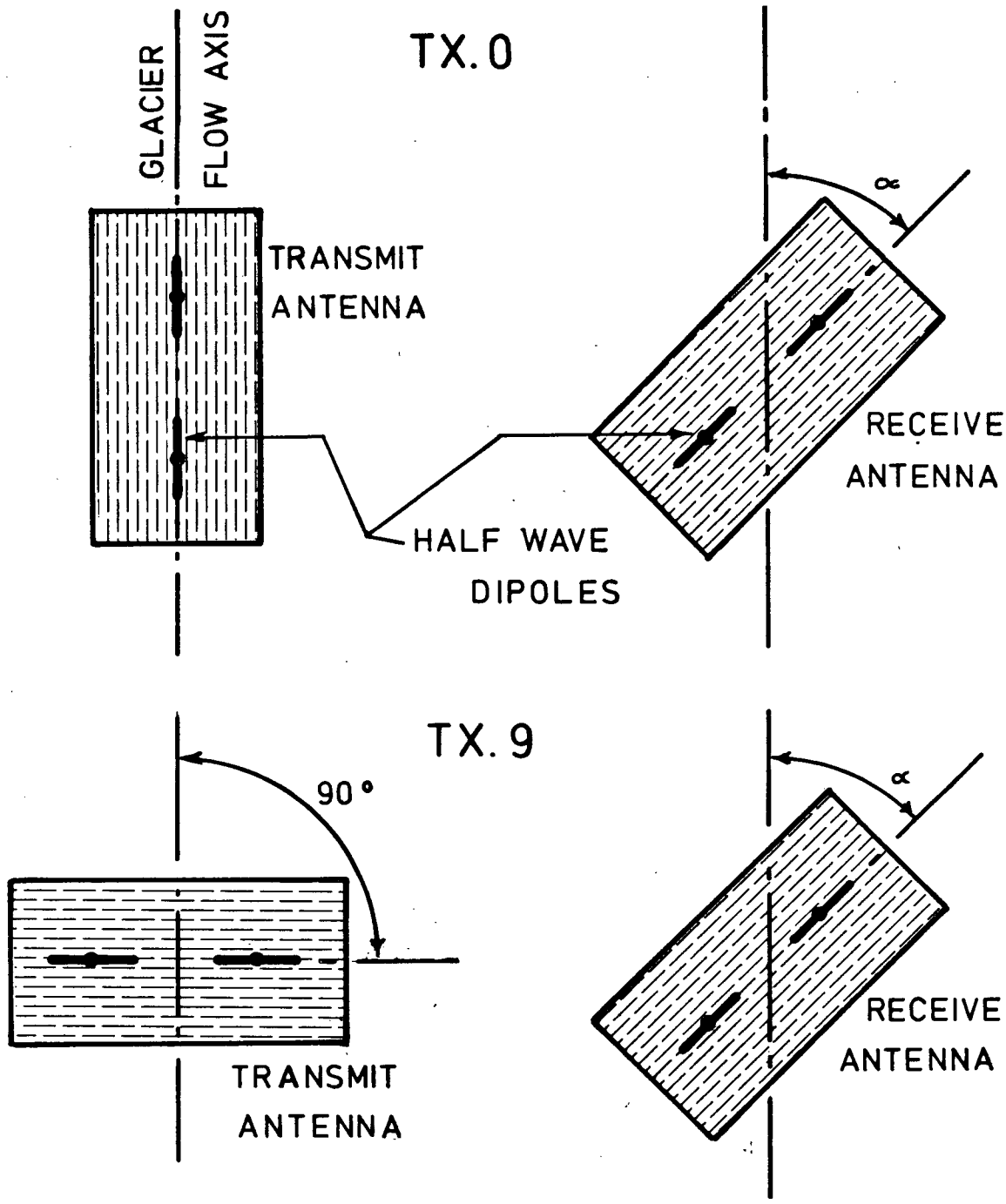

FIG. 3.1 SCHEMATIC OF ANTENNA ROTATION EXPERIMENTS, PLAN VIEW

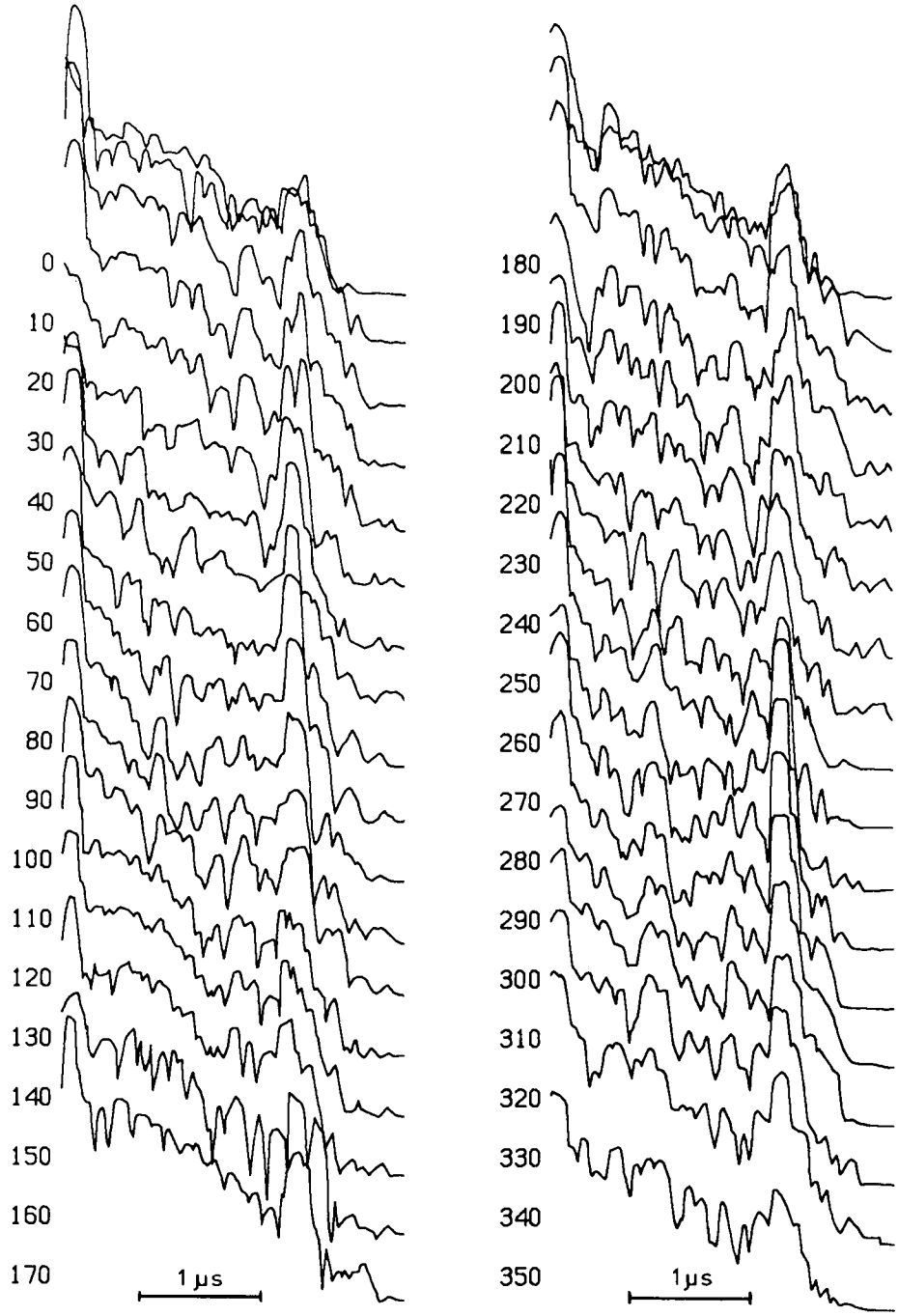

FIG. 3.2 CORRECTED RECORDS OF EXPERIMENT "TX.0"

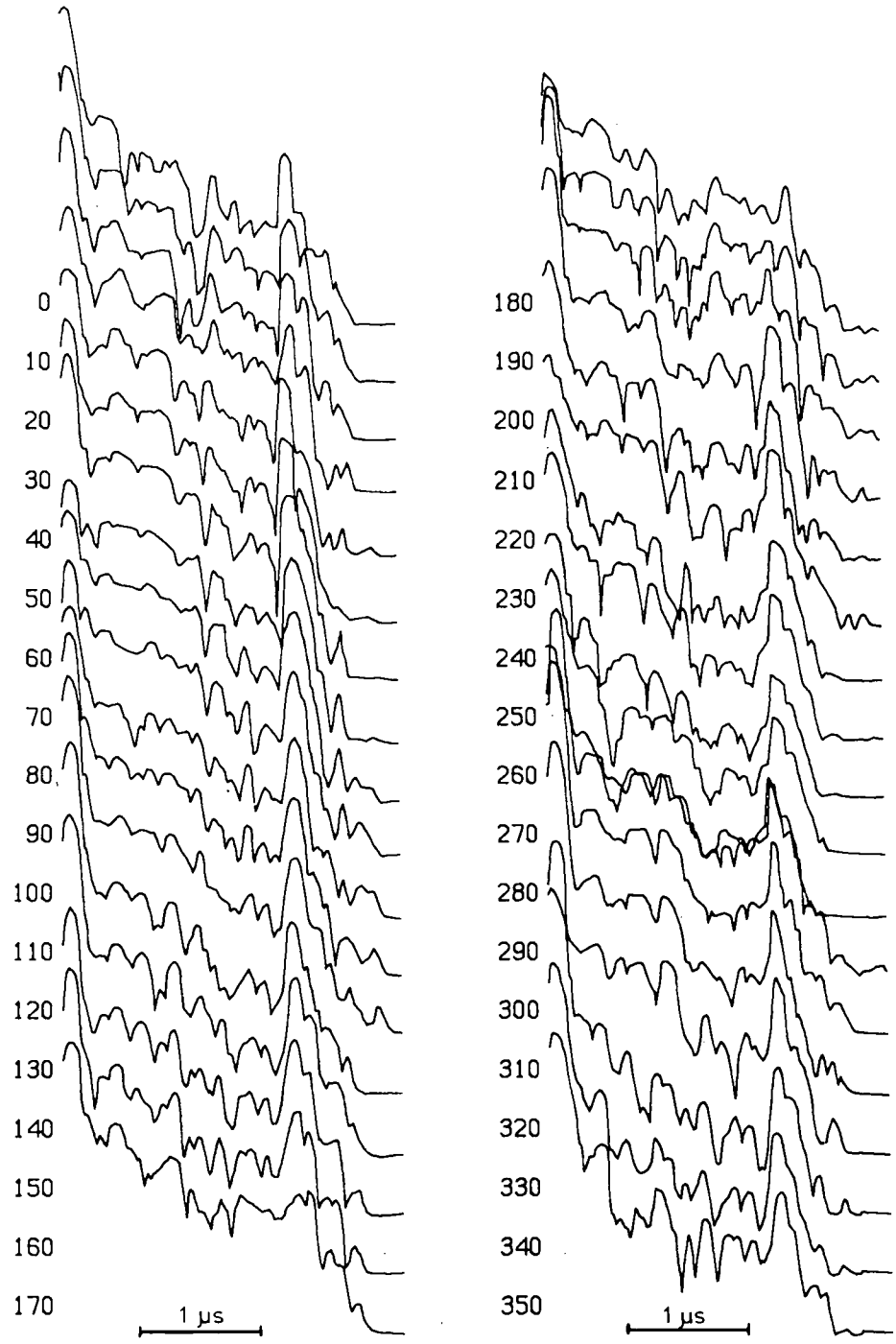

FIG. 3.3 CORRECTED RECORDS OF EXPERIMENT "TX.9"

along the leading edge of the oscilloscope trace; these were the only sharply visible edges on all of the records. However because of variations in the strength of the direct arrival power, this correction is not likely to have improved the gross timing accuracy to better than 20 ns, nor has it affected random measurement errors within the traces.

Finally, after correction, trace rotation was not considered to be a significant error source.

SYSTEM INDUCED ERRORS

Three additional effects, each caused by the glacier not being an ideal half-space, result in received power varying with antenna position. Two of these effects, involving the interaction of the antenna with materials in its near field, are changes in the antenna's effective impedance and gain pattern. Impedance changes result in mismatches with the antenna feed line and fluctuations in power fed to the receiver. Variations in the antenna pattern, caused by refraction at random variations in the ice/air surface, redistribute the received power. It is well known that roughness can cause bedrock echoes to vary significantly with small antenna movements (Nye, and others, 1972). Ice/air surface roughness could cause a similar effect. With a 36 cm wavelength, roughness on the scale of 36 cm could influence the antenna pattern. Finally, having an elliptical beam (approximately 18° x 44° semi-axes) guarantees that the receiver antenna "sees" different scatterers as the

antenna is rotated, introducing more variation in the received power.

Our data exhibit large variations, from record to record, of total received power. We estimated these variations as follows. By taking the average over the 36 records of power vs. time (Fig. 3.4A) we noted that the power returning between 0.5 us and 1.5 us falls off roughly as $1/R^2$ - 5 dB/100 m. We then calculated the average power in each record, between 0.5 us and 1.5 us, using the $1/R^2$ - 5 dB/100 m curve as a weighting function to flatten the records. The results are plotted as a function of azimuth on a linear plot (Fig. 3.5) and a log plot (Fig. 3.6).

The algorithm described above is to some extent arbitrary. However, there are features in Figs. 3.5 and 3.6 which would certainly occur with any estimator. One is the very large difference between the strongest and weakest returns within one experiment. In both experiments the difference exceeds 25 dB. Another feature is the apparent randomness of the estimated power. At several locations jumps in power exceeding ±10 dB occur between adjacent antenna positions.

If these variations have been caused by effects other than

Overleaf: Figure 3.4. Averages of power vs. time. These records are the averages of the 36 individual records of each experiment. In 3.4A the original data have been averaged. In 3.4B each individual record has been scaled up or down to an average level by subtracting the relative power figure plotted in Fig 3.6. We have called this process "azimuthal smoothing".

Superimposed on each record is a curve which represents a $1/R^2$ - 5 dB/100 m fall-off of power with depth.

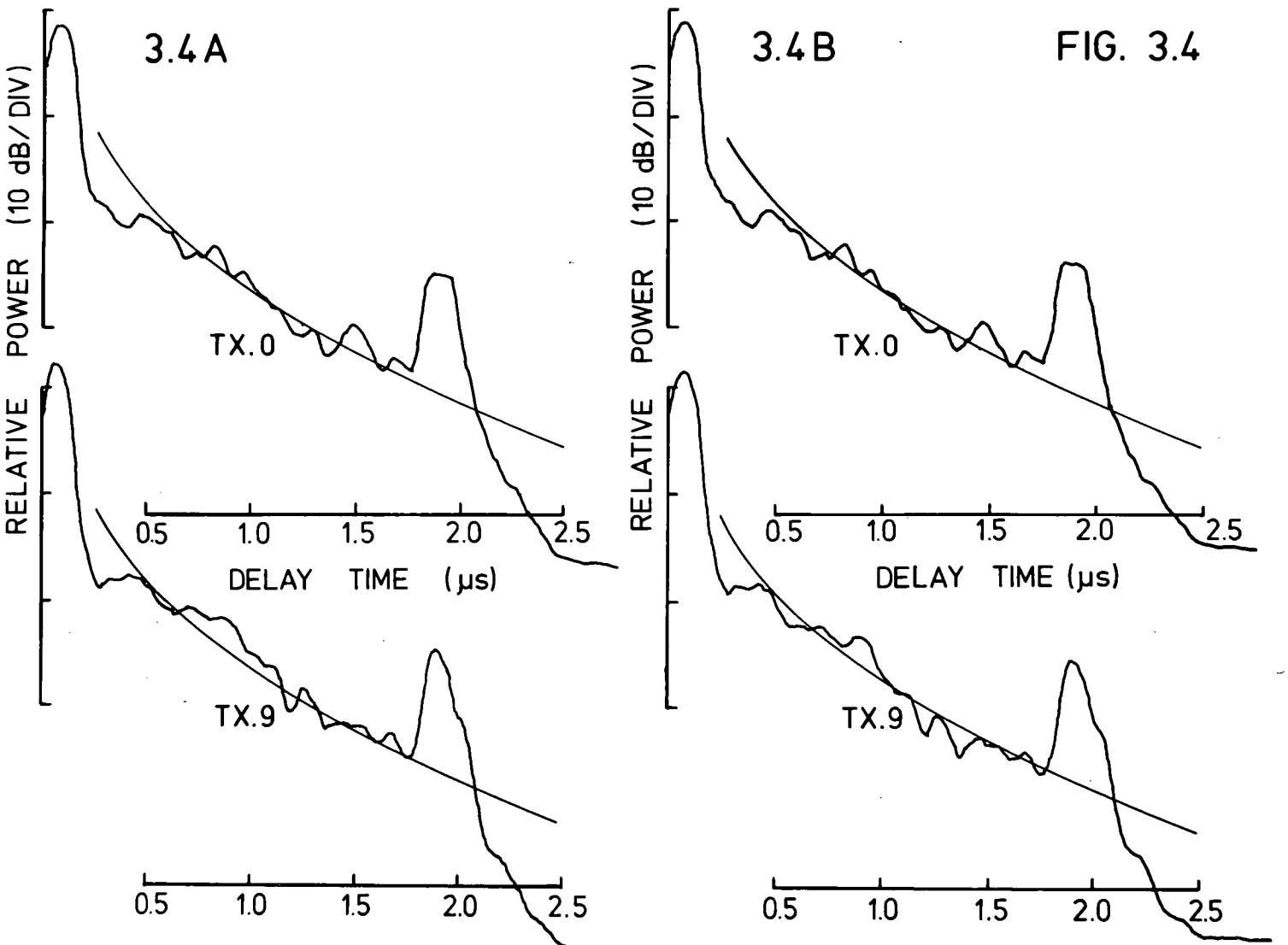
3.4A
3.4B
RELATIVE POWER (10 dB/DIV)
TX.0
TX.9
0.5
1.0
1.5
2.0
2.5
DELAY TIME (μs)

FIG. 3.4

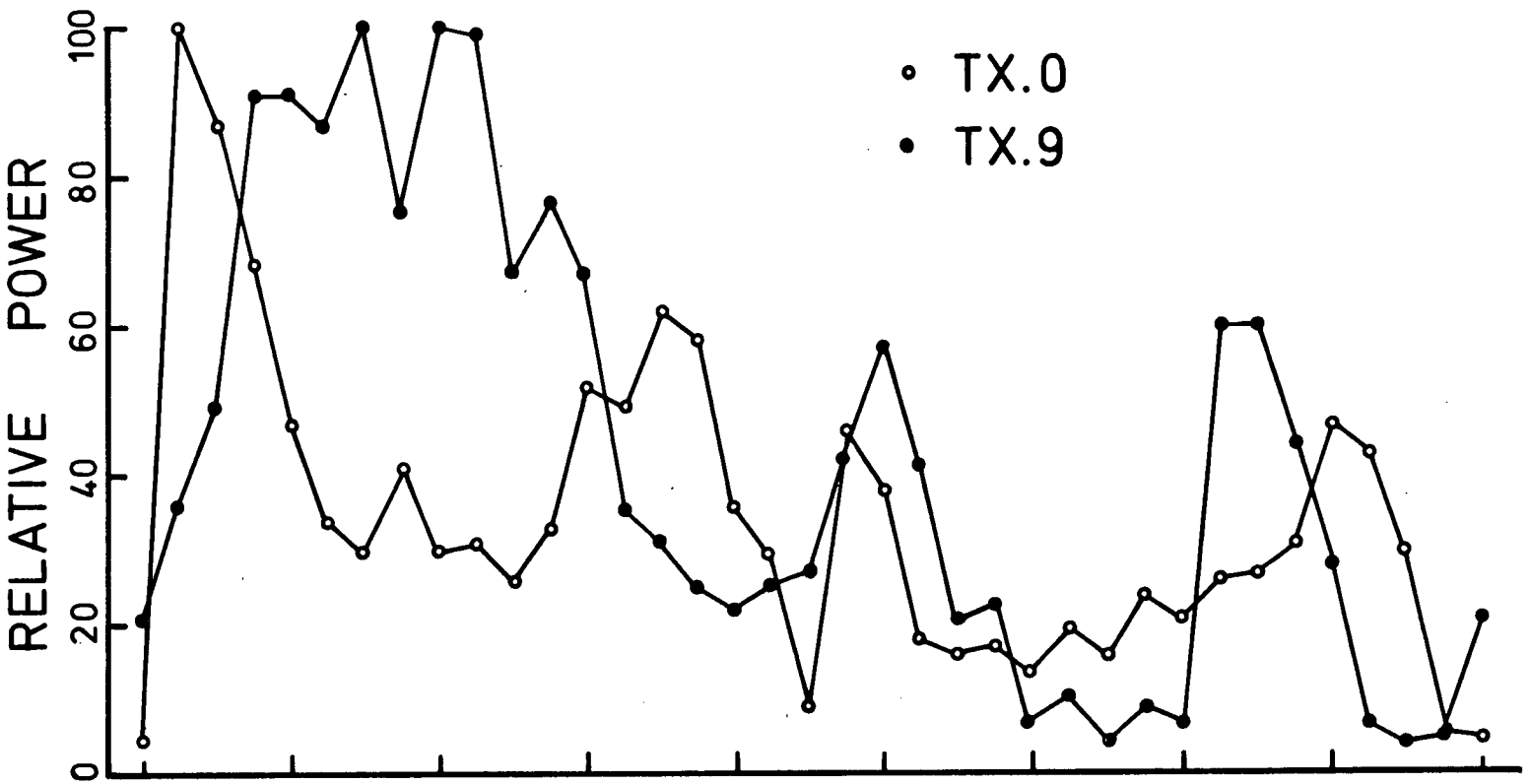
RELATIVE POWER
0
20
40
60
80
100
TX.0
TX.9
0
40
80
120
160
200
240
280
320
360
RECEIVER AZIMUTH (DEGREES)

FIG. 3.5

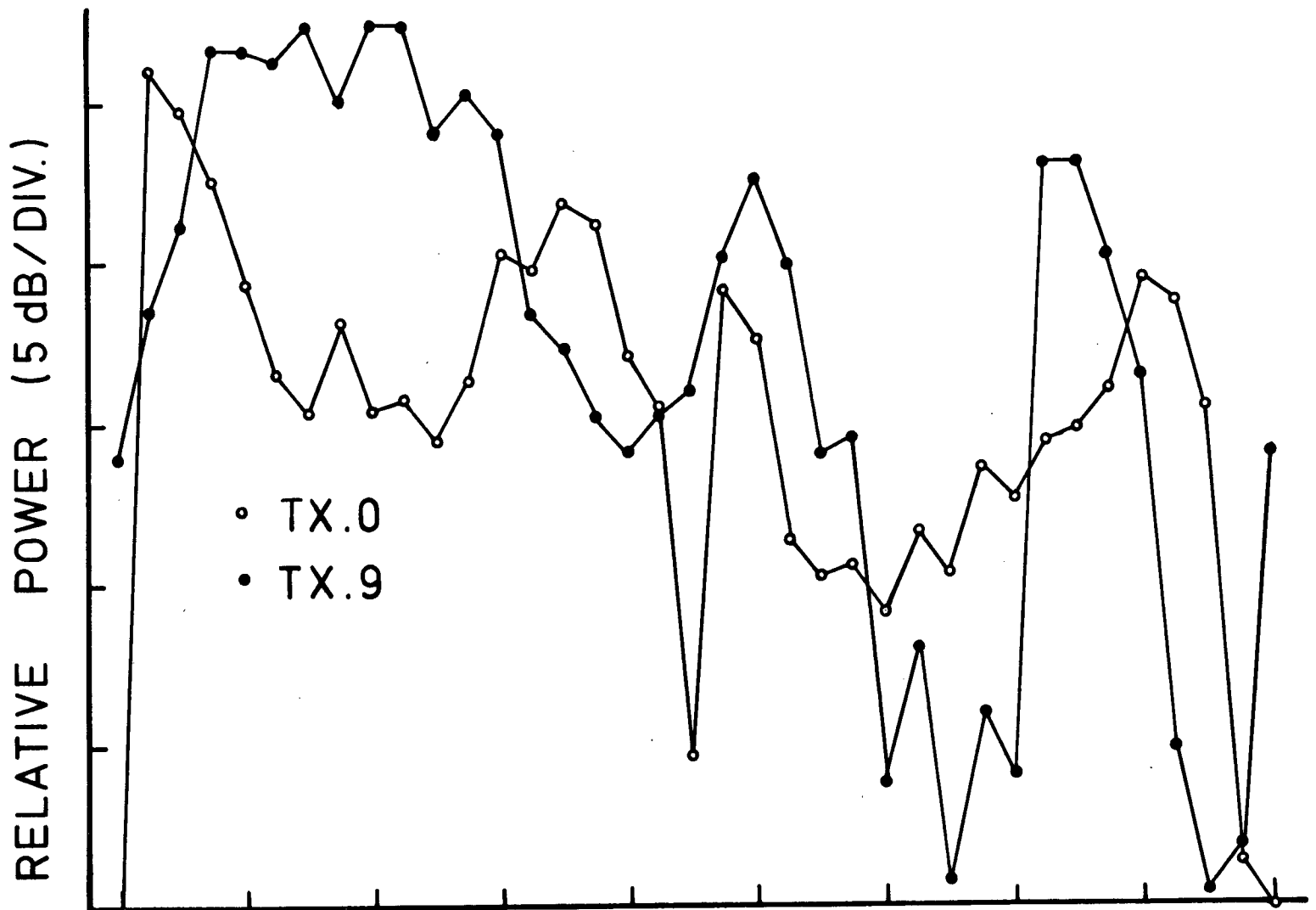
RELATIVE POWER (5 dB/DIV.)
TX.0
TX.9
0
40
80
120
160
200
240
280
320
360
RECEIVER AZIMUTH (DEGREES)

FIG. 3.6

the random interaction between the antenna and the ice/air surface we should expect to see a two-fold symmetry in the azimuthal functions of power. Examination of the discrete Fourier spectra (Fig. 3.7) of the relative power reveals that there is no tendency for the even harmonic terms to dominate, and thus that these variations are not caused by bulk properties of the glacial ice mass.

Ellipticity of polarization should also be estimated by extracting even harmonics from azimuthal power functions. The magnitudes of these additional random variations in our data thus preclude measurement of ellipticity of polarization, and the detection of birefringence.

3.2.2 DIELECTRIC ATTENUATION

The 72 records of experiments TX.0 and TX.9 provide a basis for estimating the dielectric losses in the glacier ice. The averages of the records have been plotted in Fig 3.4A. To estimate the effect of the large random variations discussed in Sec. 3.2.1, we have also averaged the records after having scaled each record to correct for these large variations. This was done by subtracting the relative power figure plotted in Fig. 3.6 from its respective record, and adding the average power figure from Fig. 3.6 to all the records. In this way the power estimating algorithm described in the previous subsection would always yield a relative power figure equal to the average power figure. This procedure, which we have called azimuthal smoothing, changes the peak power reflected at the bedrock by ±1 dB. We can conclude from this small deviation that the large

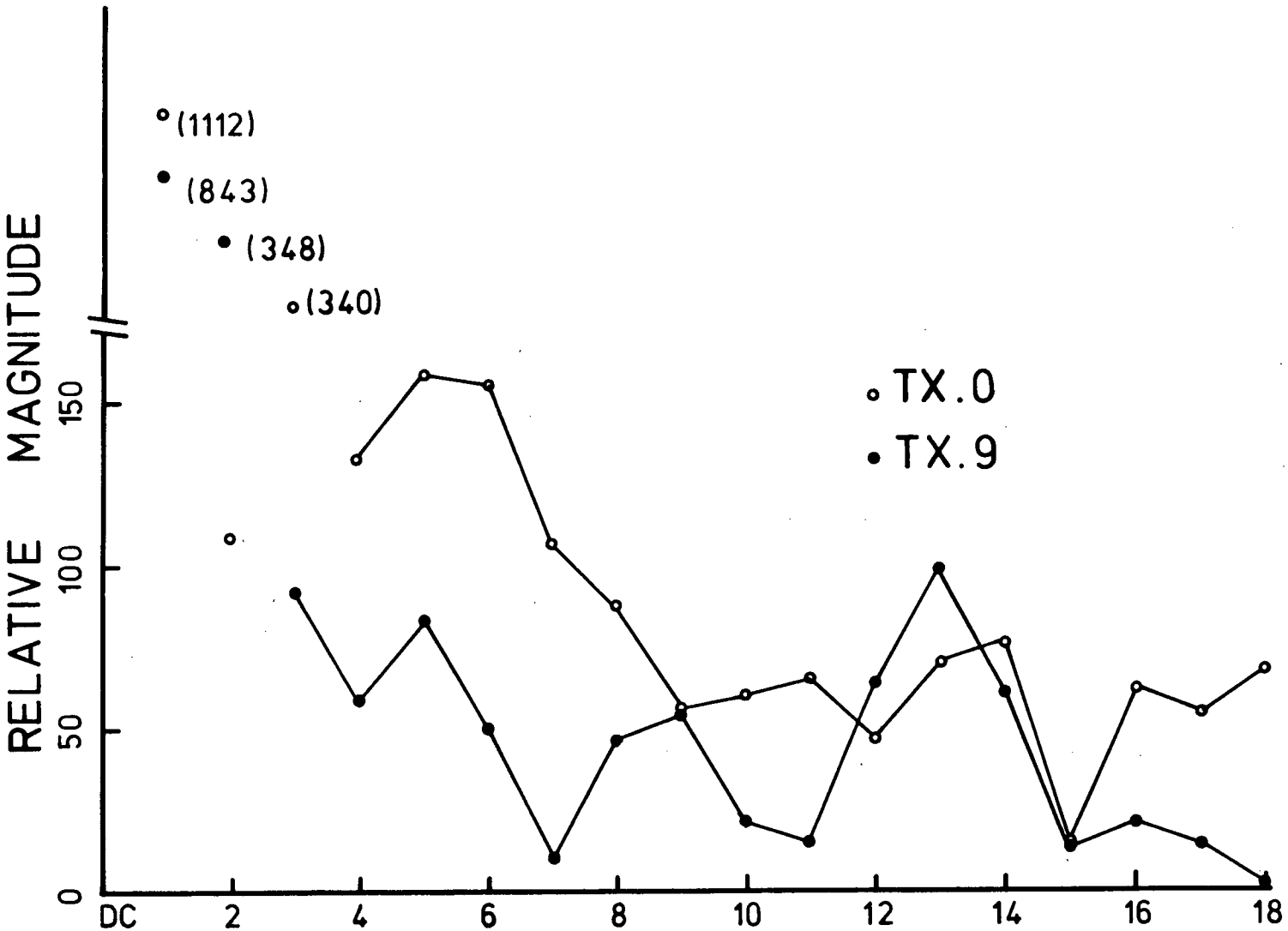

FIG. 3.7 DISCRETE FOURIER SPECTRA OF AZIMUTHAL POWER

record to record variations do not adversely affect our ability to measure an average bedrock reflection power.

Table 3.1 Dielectric Loss Computation

Transmitted power		+66 dBm
Received power	-	-32 dBm
		98 dB
Geometric losses at 158m		-81 dB
System losses		-14 dB
Bedrock reflectivity		-20 dB
Two-way antenna gain		+31 dB
Dielectric losses		-14 dB
		-98 dB

The measured bedrock echo strength, determined from Fig. 3.4, is -32 dBm. To compute the dielectric losses from one datum requires that we assume a value for the bedrock reflectivity. A commonly used value is -20 dB (Davis, unpublished). The echo delay is 1.85 us corresponding to an ice depth, with cable length corrections, of 158 m. These two figures require that the total dielectric losses be 14 dB, yielding loss rates of 4.5 dB/100m or $f\tan\delta = 0.26$.[1] table 3.1 summarizes the dielectric loss calculation.

---

[1]We must be aware that the bedrock reflectivity value of -20 dB represents a simplification of the combined dielectric contrast and surface roughness effects, and was selected to account for radio echo sounder behaviour at VH frequencies. To use this figure here we must assume that this simple description of bedrock behaviour can be extended, unchanged, to UH frequencies. This is not necessarily the case since features such as water films may have substantial effects at the higher frequencies. Nonetheless since we have no other estimate we shall use this figure.

The mean ice temperature of Hazard Glacier at the experiment site is known (Fig. 3.8) to be about -5°C (Clarke, private communication). The value of ftan δ = 0.26 at -5°C agrees very well with measurements of Westphal (Evans, 1965).

3.2.3 SCATTERED POWER DENSITY VS. DEPTH

Given from the previous subsection that the two-way dielectric losses are about 9 dB/100 m, we may now infer from Fig. 3.4 that at Hazard Glacier drill site #1 the scattering coefficient, C, as defined by Davis (unpublished, p. 64, eq'n 5(1)) increases with depth.

$$C = \frac{P_s}{P} \quad m^{-1} \tag{3.1}$$

where P_S is the scattered power per unit volume and P is the incident power density. A constant C and dielectric losses of 9 dB/100 m requires that received power scattered from a shell of radius R, fall off with R as $1/R^2$ - 9 dB/100m (Davis, unpublished, p. 66, eq'n 5(3)). Since the actual scattered power is best fitted by a 5dB/100m loss curve, (Fig. 3.9) we conclude that the scattering coefficient increases with depth. The implication of this result is that the size and/or density of scatterers (presumably rock debris, water cavities, conduits) increases with depth.

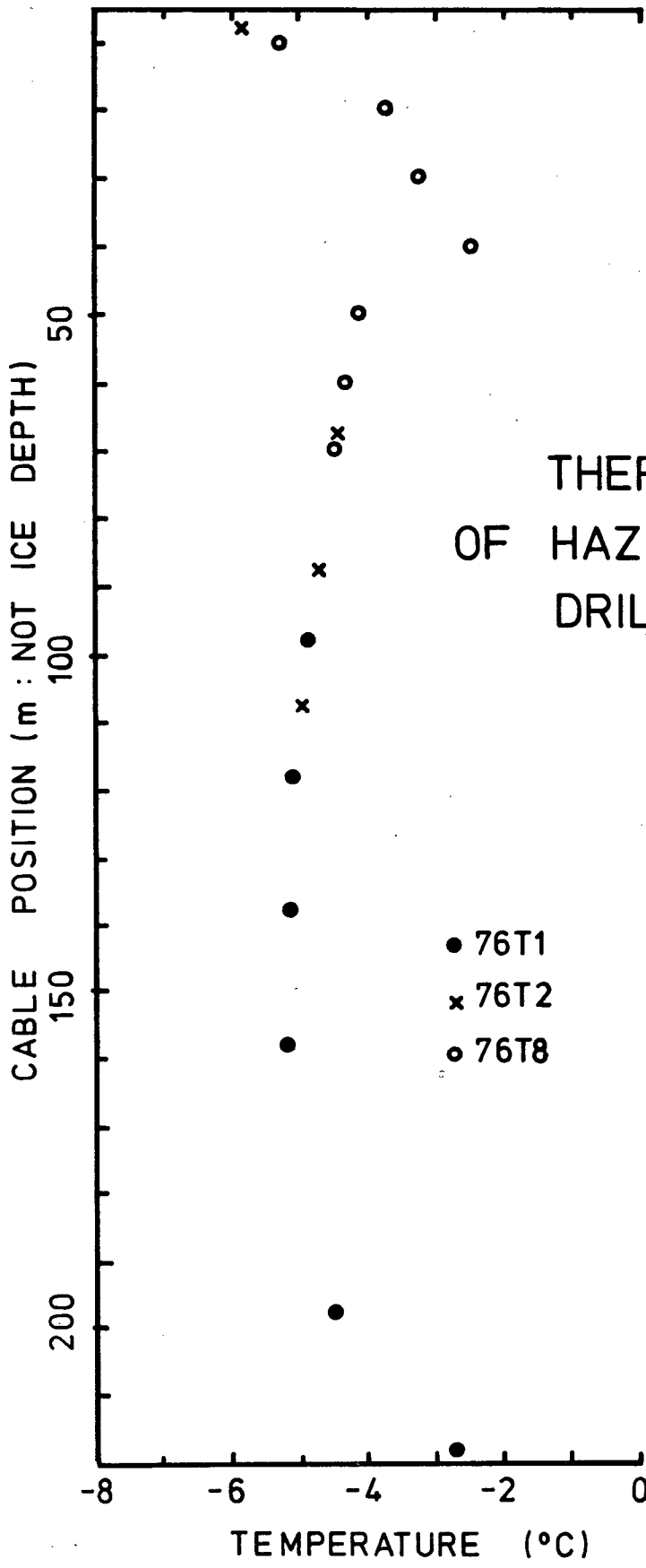

FIG. 3.8
THERMAL REGIME
OF HAZARD GLACIER
DRILL SITE 1

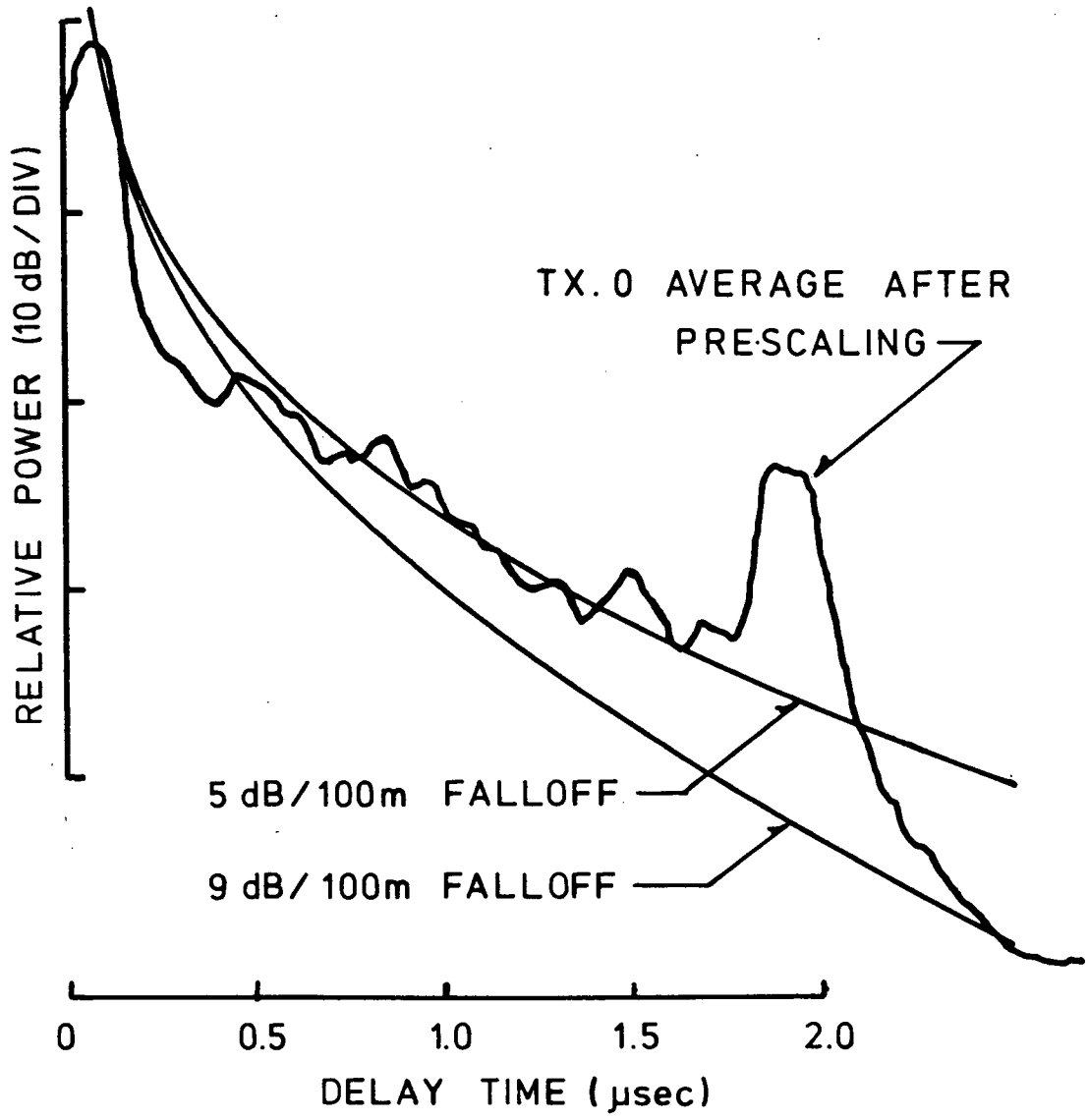

FIG. 3.9 COMPARISON OF DIELECTRIC LOSS AND SCATTERED POWER

3.3 DETECTION OF LARGE CONDUIT SCATTERERS

A further examination of Fig. 3.4 reveals that at a time delay of 1.5 us the average record of TX.0 exhibits a strong peak 5 dB above the local time average. This peak is not evident in the average record of TX.9. This section examines the possibility of using high resolution UHF radio echo sounding to identify large conduit or "linear" scatterers, and further, discusses the possibility that data at time delay 1.5 us might represent such a scatterer.

3.3.1 THEORETICAL PATTERNS FOR CONDUIT SCATTERERS

We have taken the approach that linear scattering objects generate signature patterns, i.e. the pattern of data produced by a linear scatterer, present in the range of an antenna rotation experiment, may somehow be identified with the scattering object. By modelling the scatterer as a horizontal flat ribbon (Appendix 3) the ratio of power received from the scatterer, to the total transmitted power max be estimated by

$$\left[\frac{P_R}{P_T}\right]^{1/2} \cong \frac{W\lambda}{4\pi X_1^2}\left|\left(\frac{1-i}{2\sqrt{2}}\right)G(\beta,\alpha_T)G(\beta,\alpha_R)\cos\beta\left[\frac{2X_1\sec\beta}{\lambda}\right]^{1/2}\right.$$

$$\left. + \frac{1}{\pi^2}\sum_{P=1}^{\infty} J(P/8)\ \exp\left(-i\frac{\pi}{2}P\right)\right|$$

(3.2, cf. A3.59)

where (see Fig. A3.1) W is the width of the scatterer, X_i is the scatterer depth, G is the antenna gain function, β is the angle of nearest approach (angle of incidence), and J, defined by eq'n A3.37, is antenna pattern dependent. α_T and α_R are the respective azimuths of the transmit and receive antennae relative to the scatterer normal.

The approximation is valid if $W\sin\beta \ll 1$. For the near vertical angle of incidence required by our high-gain antennae, W may be several wavelengths. In our case, widths up to 1 m may be reasonably modelled.

Equation 3.2 comprises two parts. The first term is the evaluation of the integral over a removable singularity, and is dependent only on the gain of the antennae toward the

---

First and second overleaves: Figure 3.10. Theoretical antenna rotation patterns for the U.B.C. high-gain corner reflector antennae. The two rosettes model respectively experiments TX.0 and TX.9. In each rosette there are two curves. The outer dashed curve plots the relative power calculated using the numerical scheme defined in Appendix 3. These values have been normalized to the maximum value for the two model experiments. The inner shaded curve, always two petals, is the product of the value of the first curve with either $\cos^2\phi$ or $\sin^2\phi$. The second curves show the expected patterns if the backscattered radiation has the identical polarization to the incident polarization. Here we have assumed that no depolarization or polarization rotation has occurred.

Superimposed on each rosette is a schematic representation of the scatterer position. The heavy line represents the scatterer, oriented at angle α (see Fig. A3.1), displaced by angle β off of the vertical. Full scale displacement represents 45° off vertical.

The large dynamic range at $\beta = 20°$ is due to a strong null in the antenna E-plane at about 20°.

Third and fourth overleaves: Figure 3.11. Theoretical antenna rotation patterns for dipole antennae. See description of Fig. 3.10.

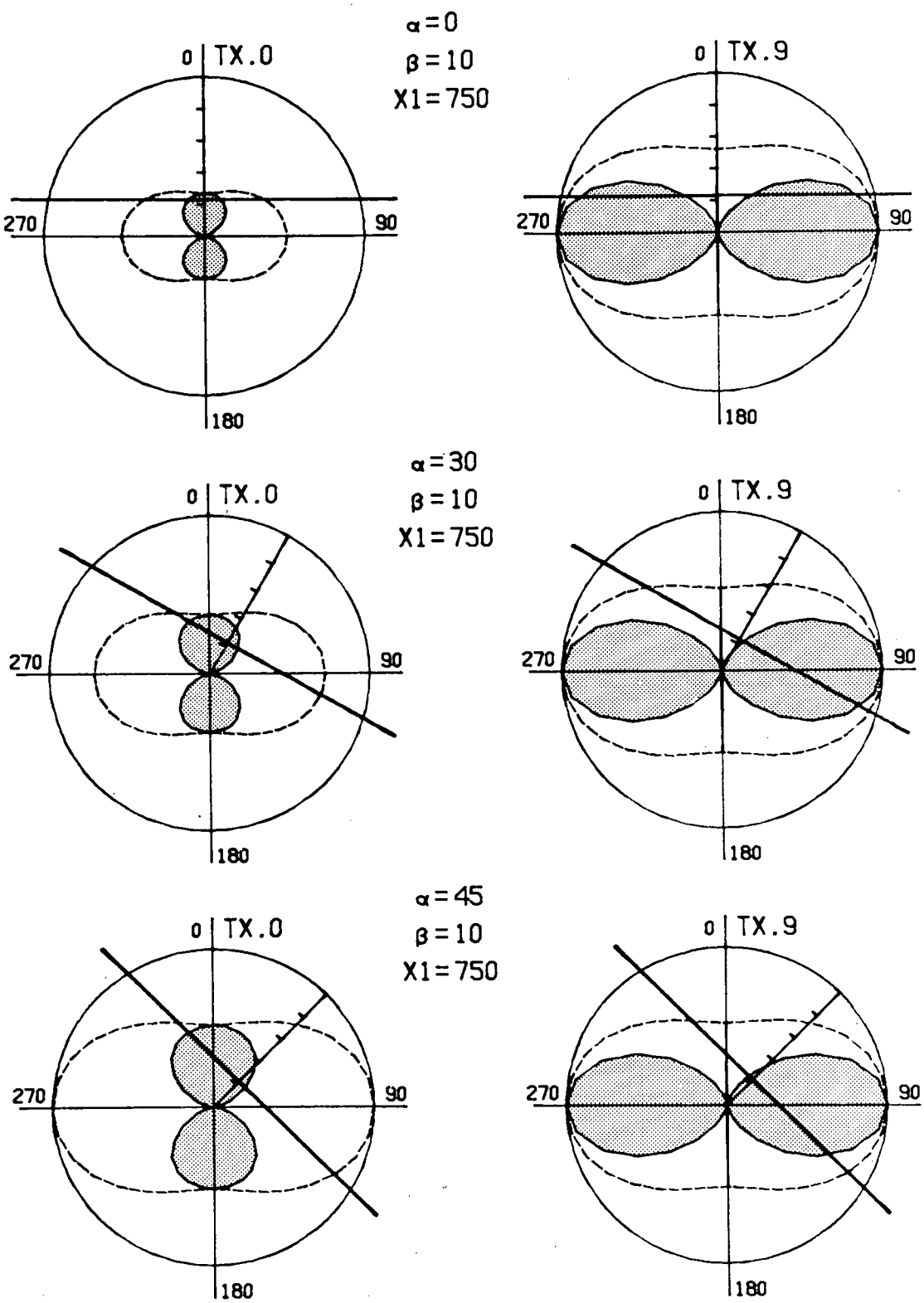

FIG. 3.10 SAMPLE THEORETICAL ANTENNA ROTATION PATTERNS FOR CORNER REFLECTOR ANTENNAE

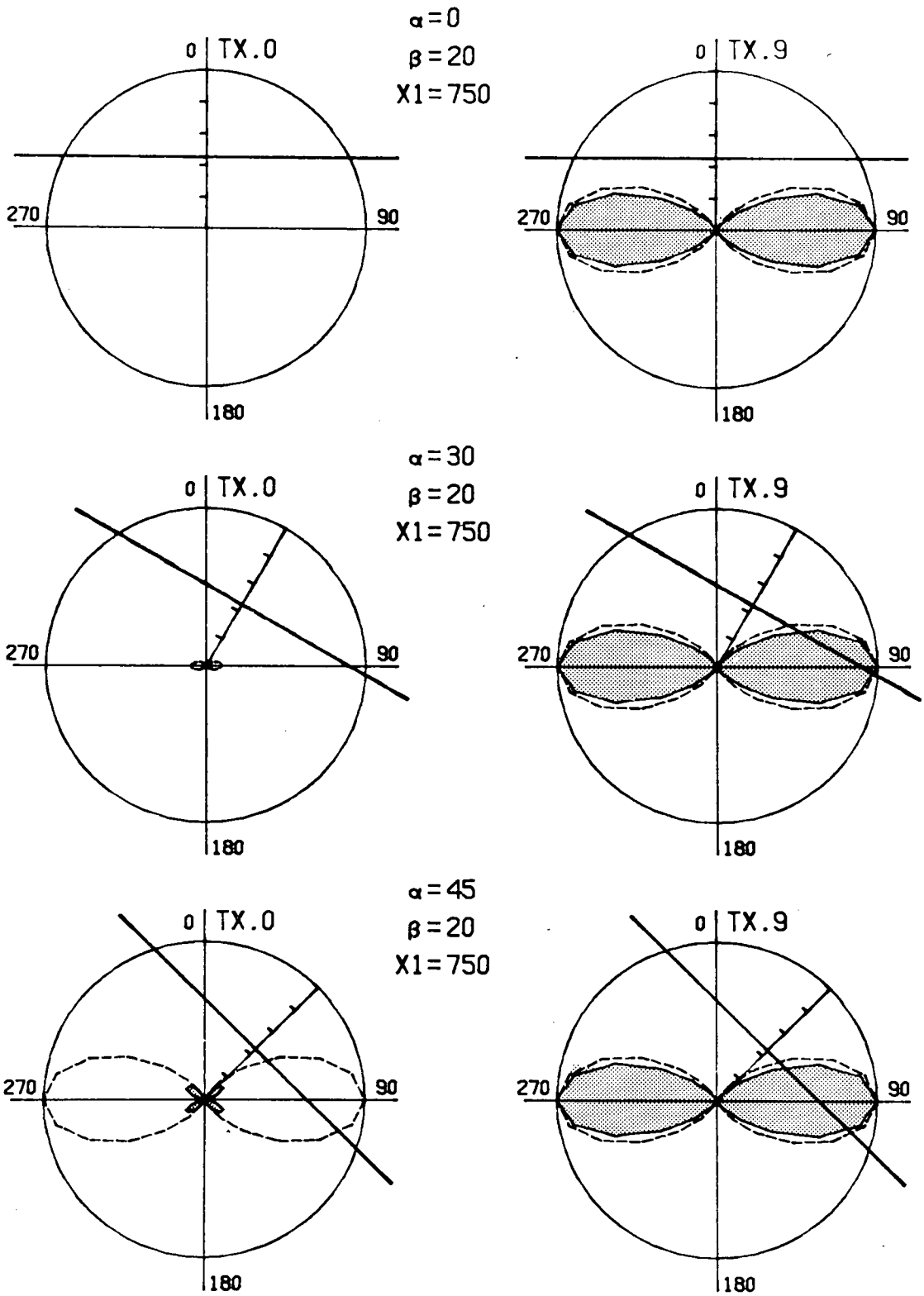
α = 0
β = 20
X1 = 750
0
TX.0
270
90
180
0
TX.9
270
90
180
α = 30
β = 20
X1 = 750
0
TX.0
270
90
180
0
TX.9
270
90
180
α = 45
β = 20
X1 = 750
0
TX.0
270
90
180
0
TX.9
270
90
180

FIG. 3.10 CONT.

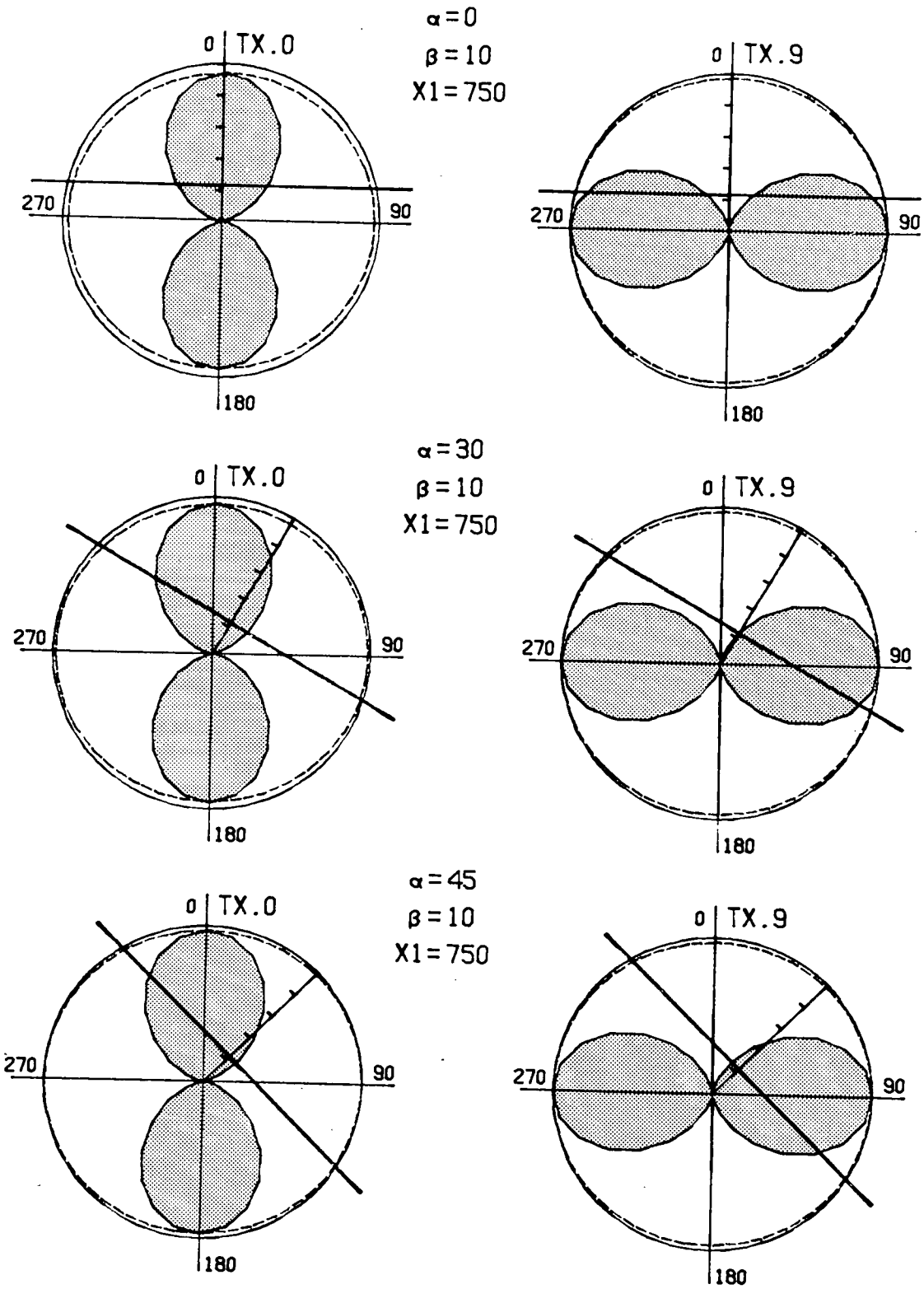

FIG. 3.11 SAMPLE THEORETICAL ANTENNA ROTATION PATTERNS FOR DIPOLE ANTENNAE

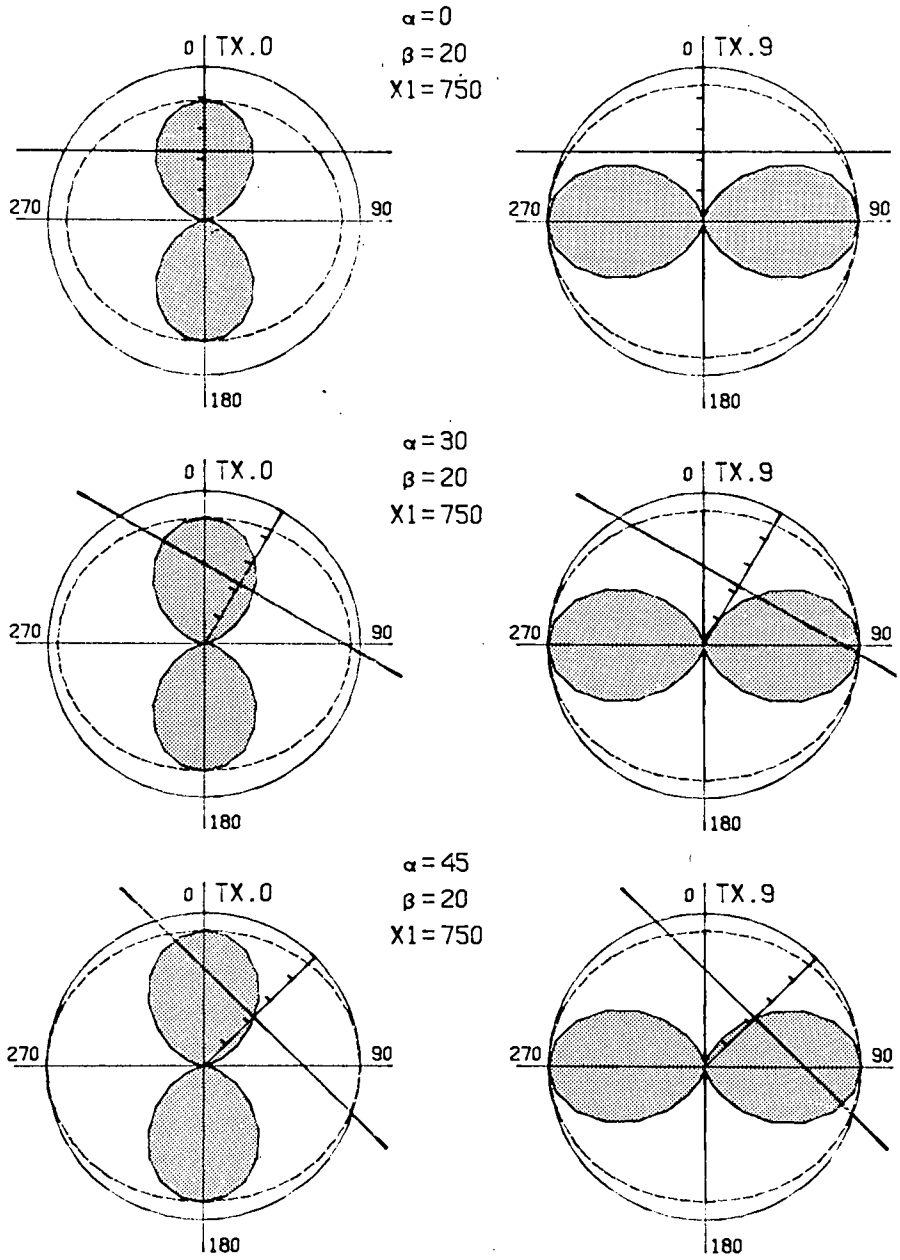

FIG. 3.11 CONT.

scatterer's nearest point $G(\beta, \alpha_{T,R})$. The second term evaluates the residual difference between the removable singularity and the gain dependent integral.

Using the numerical scheme established in Appendix 3 we have evaluated the continuous wave returning power pattern from several scatterer positions, modelling both our high-gain corner reflector antennae, and single half-wave dipole antennae (Figs. 3.10 and 3.11). In all cases we have found that the pole contribution to the integral is at least two orders of magnitude larger than the residual contribution, even when the integration extends θ to well beyond 45°. We can then neglect the residual component, and consider the pole term alone to represent the entire integral

$$\left[\frac{P_R}{P_T}\right]^{\frac{1}{2}} \cong \frac{W\lambda}{8\pi X_1^2}\; G(\beta,\alpha_T)G(\beta,\alpha_R)\cos\beta \left[\frac{2X_1 \sec\beta}{\lambda}\right]^{\frac{1}{2}} \qquad (3.3)$$

Since the only α and β dependence now occurs in the factor $G(\beta,\alpha_T)G(\beta,\alpha_R)$, the shape of the pattern is indistinguishable from that of a point scatterer located at the L origin. Hence, the shape of the pattern alone cannot be used to identify line scatterers.

Equation 3.3 may be rewritten

$$\left[\frac{P_R}{P_T}\right]^{1/2} \cong \frac{W\lambda^{1/2}}{4\sqrt{2}\pi} G(\beta,\alpha_T)G(\beta,\alpha_R)\,(R_o)^{-3/2} \qquad (3.4)$$

indicating that backscattered power fall off as R^{-3}. A plane reflector backscatters power as R^{-2}. A point scatterer backscatters power as R^{-4}. As determined above, a large linear scatterer cannot be identified by data collected from a single location. A positive identification would require the locating of the scatterer from several radar sites and fitting the backscattered power to the R^{-3} curve.

First and second overleaves: Figure 3.12. TX.0 antenna rotation data selected at various delay times. The first eleven plots have been selected at 100 ns intervals, in the range 0.7 us to 1.7 us. The last nine plots have been selected at 20 ns intervals in a range covering the leading edge of the bedrock echo at 1.8 us.

Each rosette has been normalized to the maximum value of the data used in the rosette and plotted on a linear scale. To the right of each rosette a bar graph displays relevant power data. The bar graph is logarithmic with the full scale representing 80 dB. The top of the dark band in the left column indicates the level of the $1/R^2$ - 5dB/100m estimator described in Section 3.2. The top and bottom of the dark band in the right column mark the maximum and minimum power plotted in the corresponding rosette. As the delay time passes into the bedrock echo the power level can clearly be seen to rise well above the scattered power estimator.

Third and fourth overleaves: Figure 3.13. TX.9 antenna rotation data. Similar to Fig. 3.12.

Fifth and sixth overleaves: Figure 3.14. TX.0 antenna rotation data after azimuthal smoothing. The ratio of the maximum to minimum power (the length of the dark band in the right column of the bar graphs) are generally smaller than those of the unsmoothed data suggesting that azimuthal smoothing has tended to remove large-scale, externally caused effects. The spikey appearance at the delay times 1.80 us to 1.84 us can result from two causes - a severely different bedrock scattering regime, or, more likely, timing errors.

Seventh and eighth overleaves: Figure 3.15. Selected TX.9 antenna rotation data after azimuthal smoothing. See Fig. 3.14.

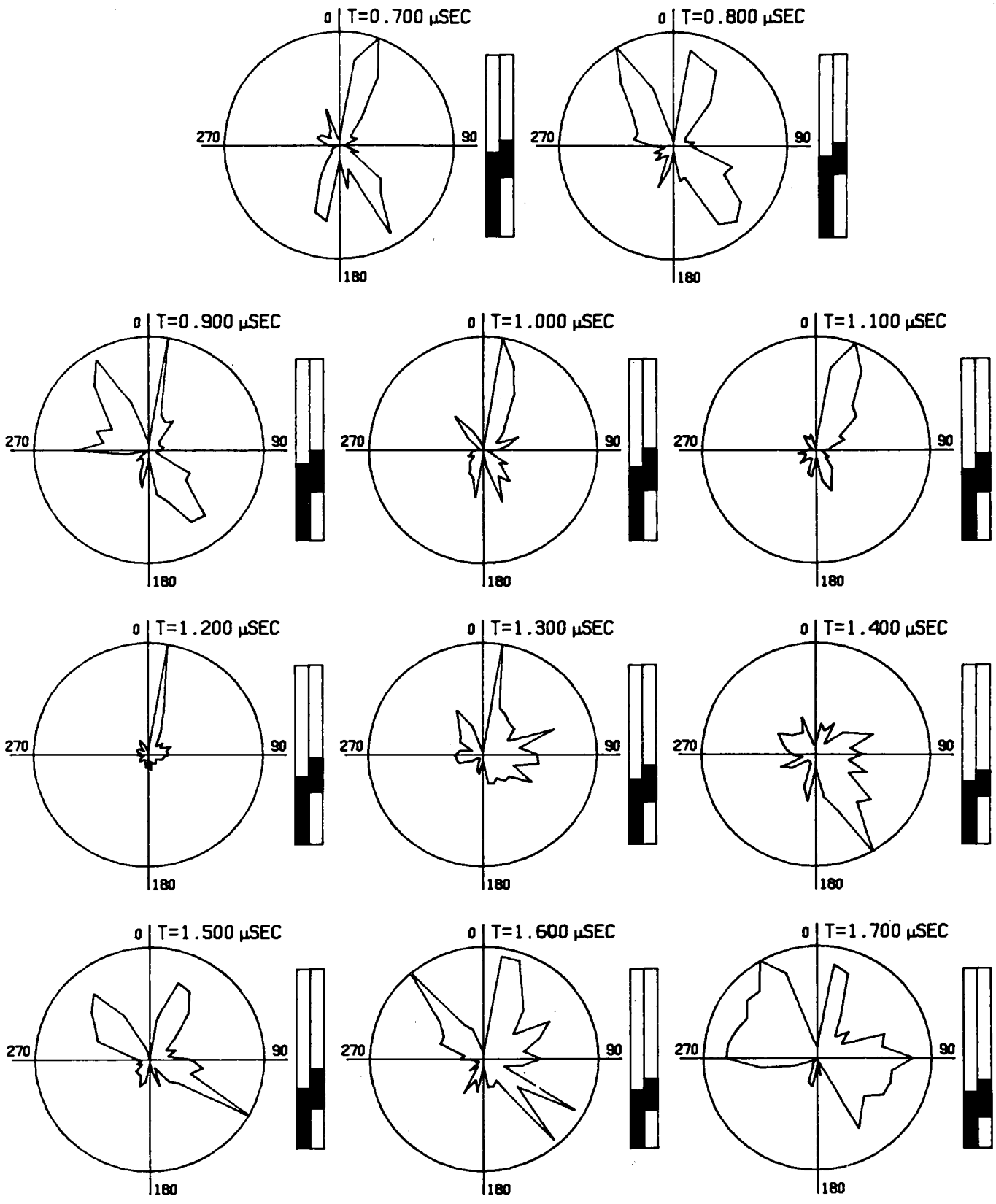

FIG. 3.12 SAMPLED ANTENNA ROTATION DATA FROM "TX.0"

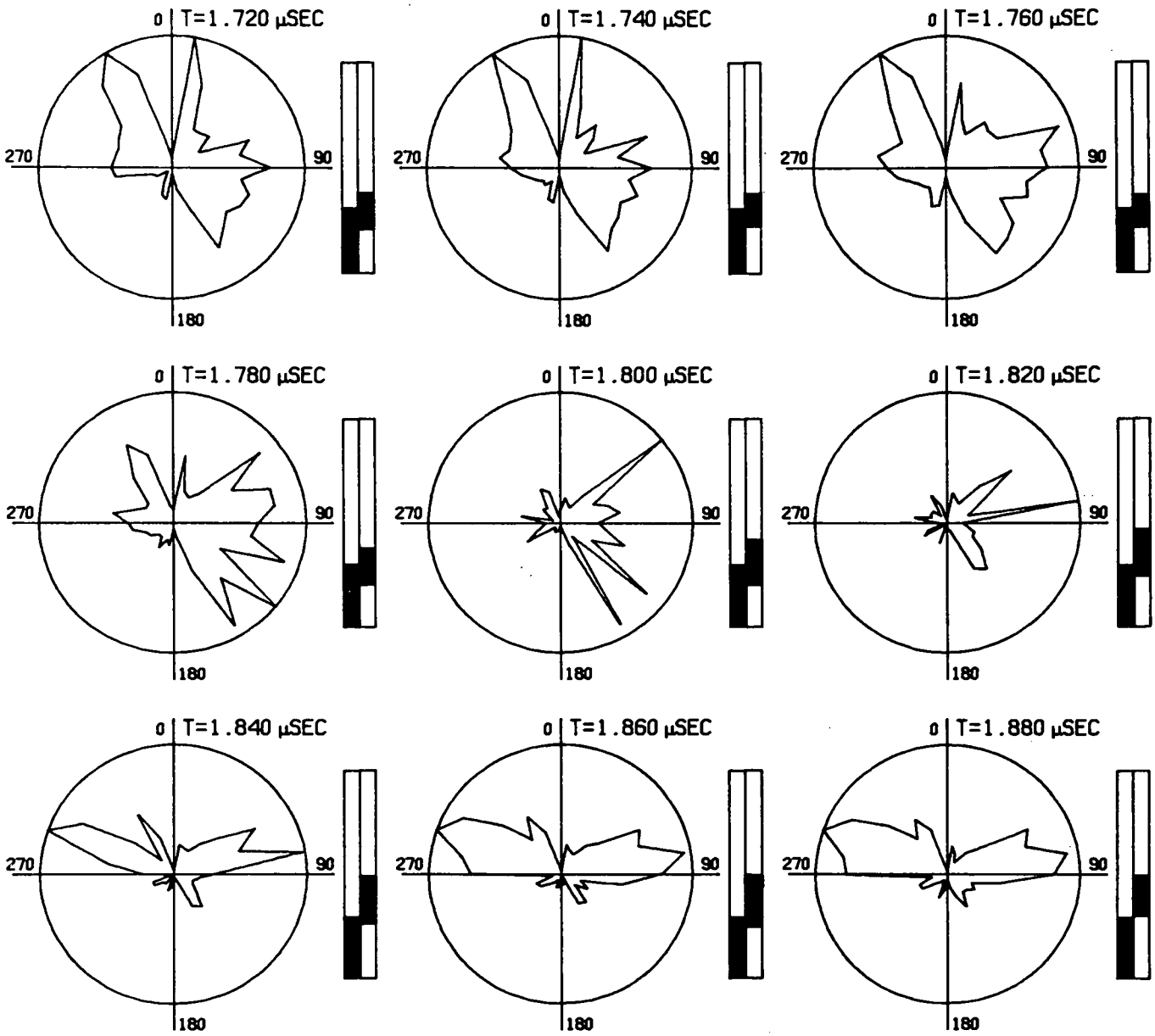
0
T=1.720 μSEC
270
90
180
0
T=1.740 μSEC
270
90
180
0
T=1.760 μSEC
270
90
180
0
T=1.780 μSEC
270
90
180
0
T=1.800 μSEC
270
90
180
0
T=1.820 μSEC
270
90
180
0
T=1.840 μSEC
270
90
180
0
T=1.860 μSEC
270
90
180
0
T=1.880 μSEC
270
90
180

FIG. 3.12 CONT.

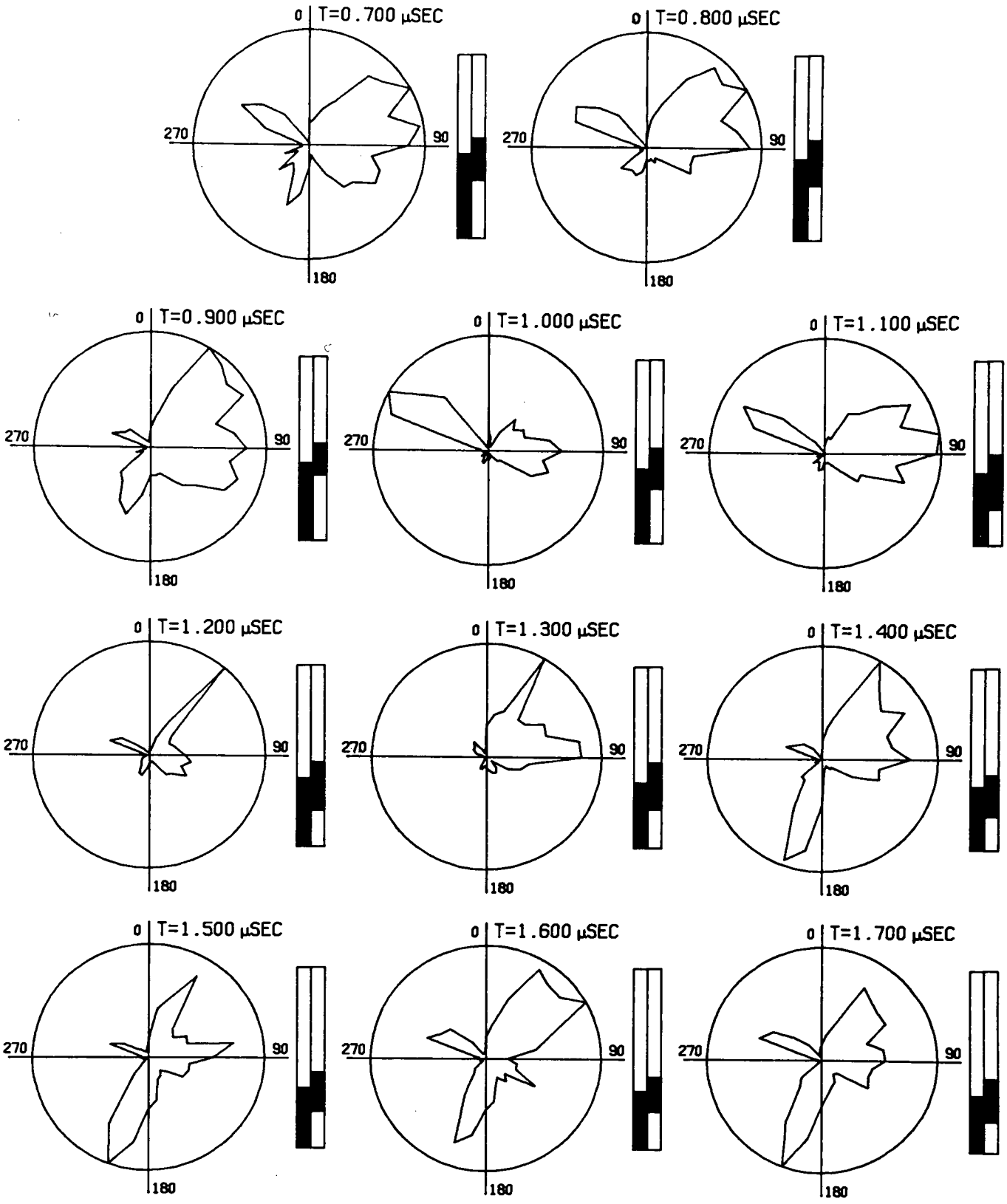

FIG. 3.13 SAMPLED ANTENNA ROTATION DATA FROM "TX.9"

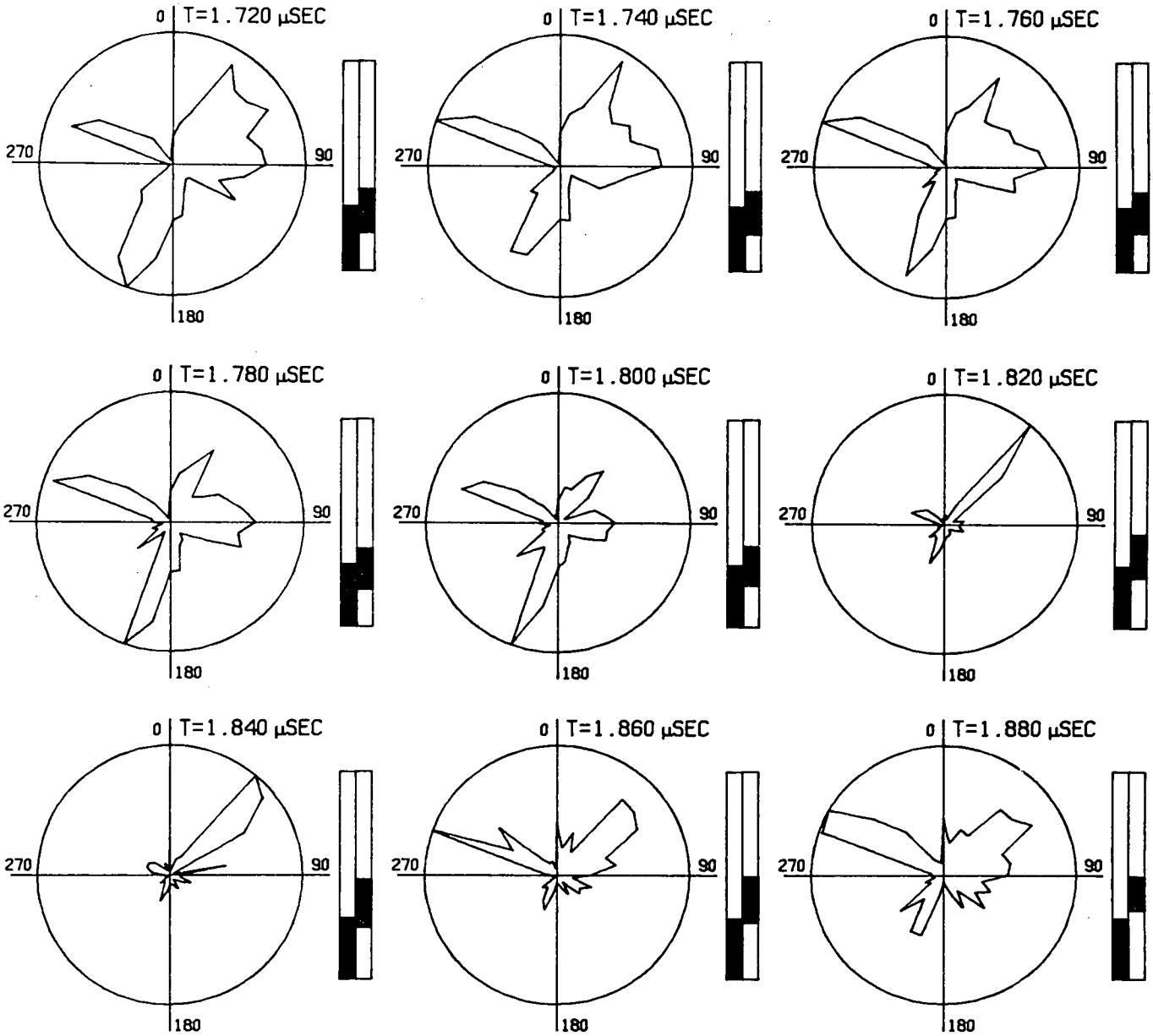
0
T=1.720 μSEC
270
90
180
0
T=1.740 μSEC
270
90
180
0
T=1.760 μSEC
270
90
180
0
T=1.780 μSEC
270
90
180
0
T=1.800 μSEC
270
90
180
0
T=1.820 μSEC
270
90
180
0
T=1.840 μSEC
270
90
180
0
T=1.860 μSEC
270
90
180
0
T=1.880 μSEC
270
90
180

FIG. 3.13 CONT.

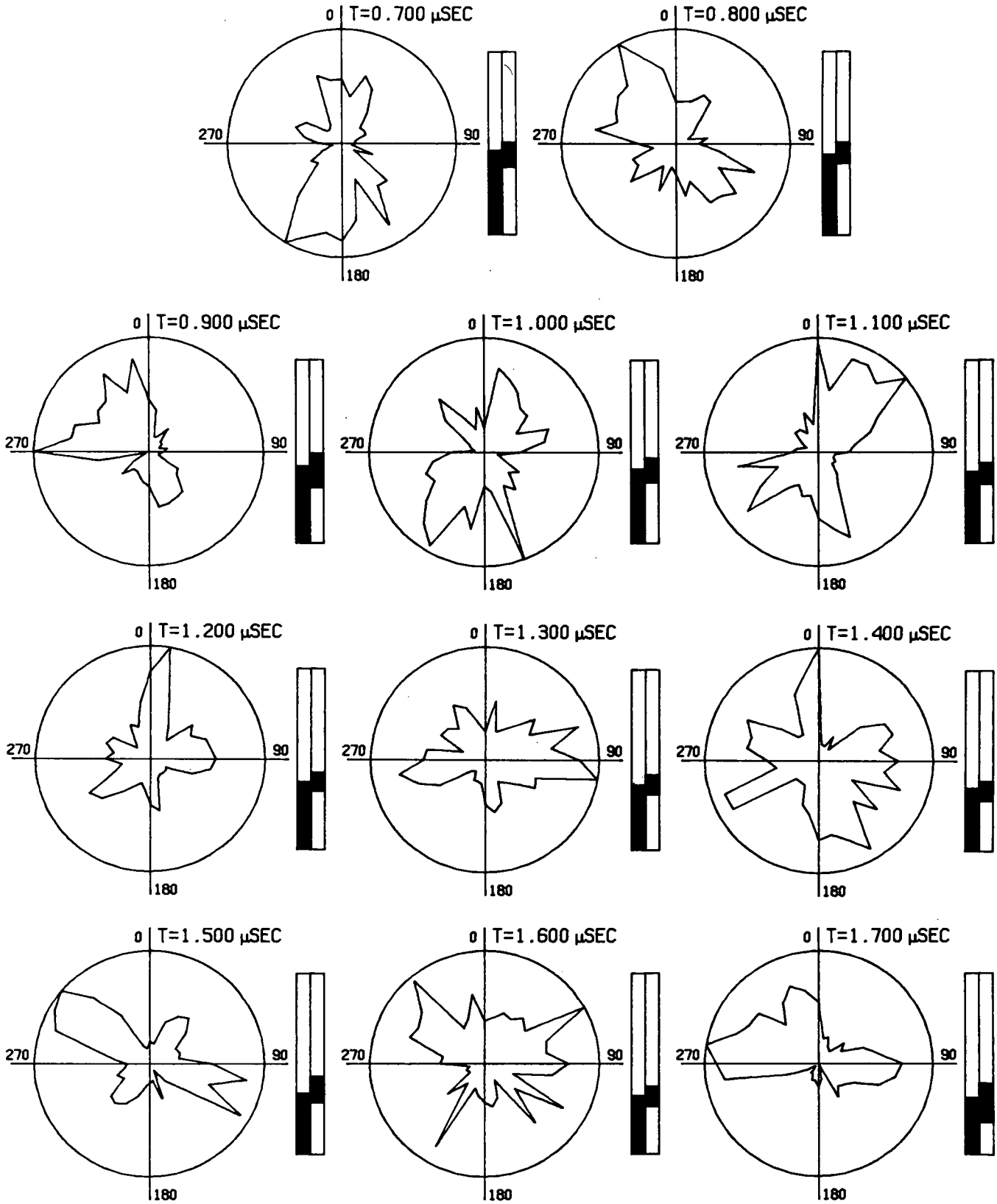

FIG. 3.14 SAMPLED ANTENNA ROTATION DATA FROM "TX.0", AFTER AZIMUTHAL SMOOTHING

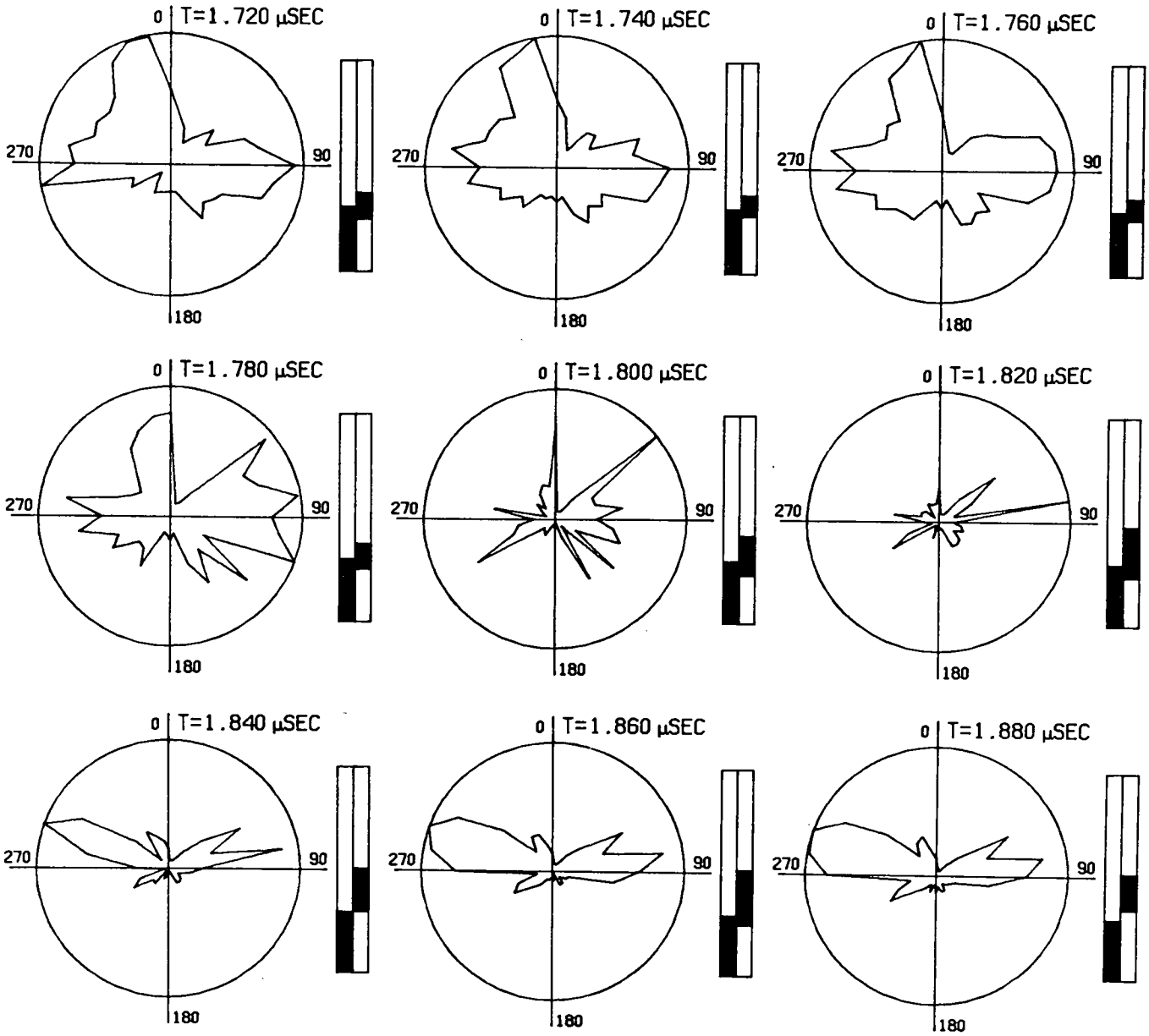
0
T=1.720 μSEC
270
90
180
0
T=1.740 μSEC
270
90
180
0
T=1.760 μSEC
270
90
180
0
T=1.780 μSEC
270
90
180
0
T=1.800 μSEC
270
90
180
0
T=1.820 μSEC
270
90
180
0
T=1.840 μSEC
270
90
180
0
T=1.860 μSEC
270
90
180
0
T=1.880 μSEC
270
90
180

FIG. 3.14 CONT.

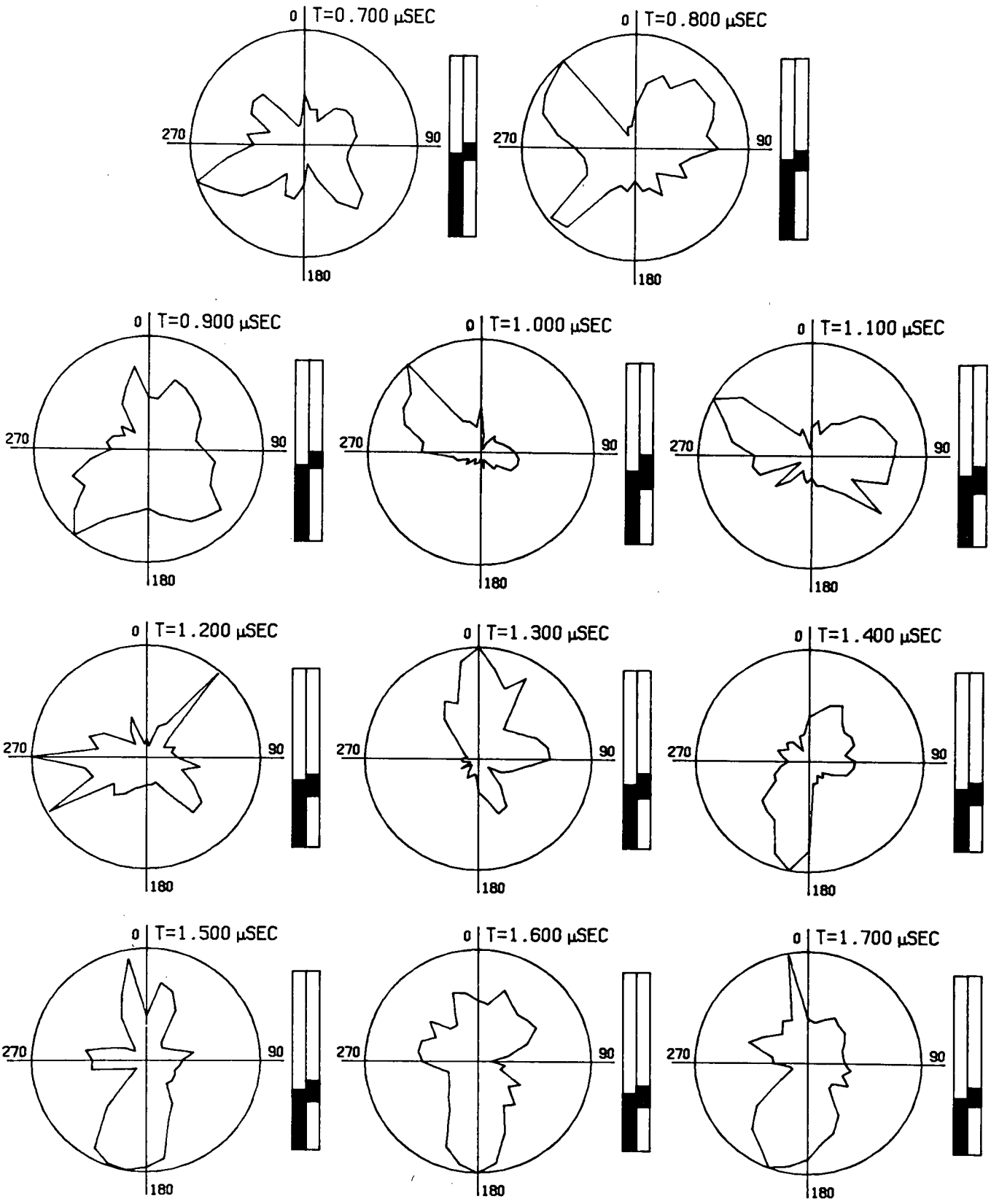

FIG. 3.15 SAMPLED ANTENNA ROTATION DATA FROM "TX.9", AFTER AZIMUTHAL SMOOTHING

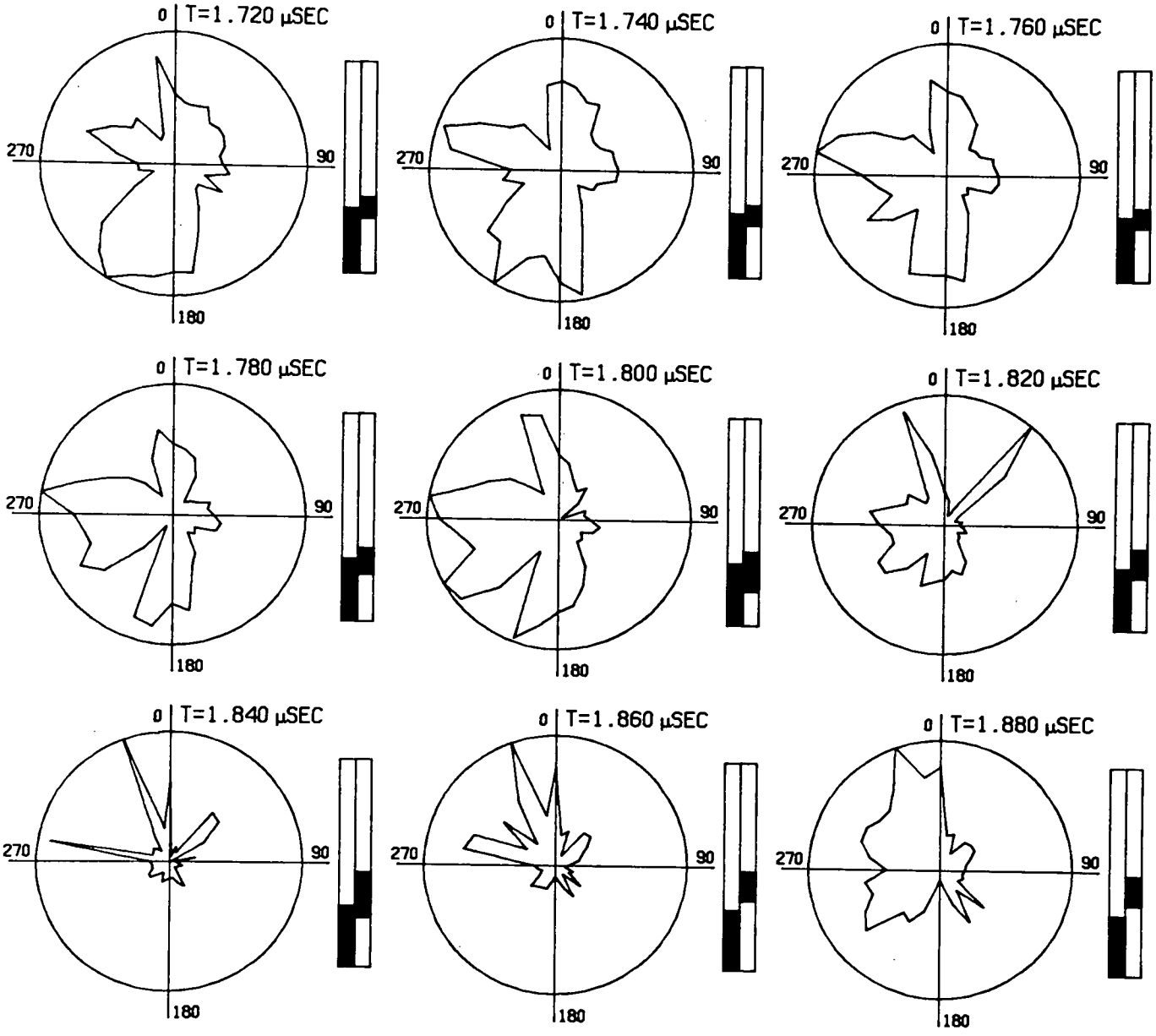
0
T=1.720 μSEC
270
90
180
0
T=1.740 μSEC
270
90
180
0
T=1.760 μSEC
270
90
180
0
T=1.780 μSEC
270
90
180
0
T=1.800 μSEC
270
90
180
0
T=1.820 μSEC
270
90
180
0
T=1.840 μSEC
270
90
180
0
T=1.860 μSEC
270
90
180
0
T=1.880 μSEC
270
90
180

FIG. 3.15 CONT.

3.3.2 COMPARISONS WITH THE FIELD EXPERIMENTS

Figs. 3.12 through 3.15 are selections of rosette plots of the two antenna rotation experiments, plotting received power vs. azimuth, with delay time as a parameter. These plots provide little evidence for the expected two-fold symmetry, even after azimuthal smoothing (Figs. 3.14 and 3.15).

The rosettes plotted from the smoothed data (Figs. 3.14 and 3.15) at delay time 1.50 us are the only patterns of the selected data which resemble two-fold symmetrical petal patterns. However, they still do not compare well with any theoretical patterns that we have generated using an idealized corner reflector model. To achieve even the least match also requires that we invoke some mechanism which rotates the polarization by about 90° since TX.0 theoretically receives its greatest power at 0° and TX.9 at 90°.

When we consider the data regarding the very low probability of observing any two-fold symmetry, the appearance of symmetry at delay time 1.50 us is most likely fortuitous.

3.4 CONCLUDING REMARKS TO CHAPTER 3

These field tests and discussions have demonstrated the difficulties associated with the use of UHF echo sounders for determining physical properties of glaciers. Measurements of attenuation, birefringence or other parameters require a capability for the accurate recording and reproduction of power vs. time data. Records collected by photographing A-scope displays have failed to provide the accuracy required for these

experiments. More important, random roughness at the ice/air surface, perhaps density variations within the near-surface ice, appear to cause large scale variations in the near-field of the antenna. At 840 MHz the glacier surface cannot be modelled as a plane surface, thus any surface based experiment must collect data with sufficient redundancy that a statistical approach may be used. Our attenuation estimate of $f\tan\delta = 0.26$, based on the average of 72 records, is our only measurement made with sufficient redundancy that it may be considered reliable, limited mainly by our knowledge of the bedrock reflectivity.

The last comments suggest another potentially serious drawback of the photographic recording technique. A statistical approach to parameter measurement may require that literally thousands of records be collected during a field experiment. Since it requires on the order of ten minutes of labour to digitize a single record the amount of time required to process a large number of photographs would be prohibitive.

Glacier surface experiments for ice properties measurements require an accurate, serviceable recording medium as do airborne surveys. In addition to our scheduled modifications to our airborne system we are concurrently developing a portable, digital, cassette logging system. We expect it to provide more accurate records than do photographs, and in an immediately computer compatible format. It will also eliminate a heavy, power-hungry oscilloscope and support hardware.

CHAPTER 4. CONCLUDING REMARKS AND RECOMMENDATIONS FOR FUTURE EXPERIMENTS

The work reported here has taken a particularly Canadian view towards radio echo sounding. The Canadian Arctic is dotted with many small ice masses likely of less than 700 m depth, including valley and alpine glaciers, as well as several ice caps in the Arctic Archipelago. We have shown by developing and airborne testing an 840 MHz radio echo sounder that all of these ice fields should be within the range of an UHF sounder.

The advantages to this approach are several. UHF antennae are readily deployable from light aircraft. This implies that airborne surveys can operate in small valleys where light aircraft are necessary and where high gain antennae minimize interference. Also, the use of light aircraft would ease logistic problems associated in mapping the Archipelago ice caps since an UHF radar survey could be operated from one of the small aircraft which routinely service these areas.

Our results from surface based experiments carried out on the Hazard Glacier confirm that with $f\tan\delta = 0.26$ at -5°C, 840 MHz must be included in the useful radio echo sounding band. However these tests also demonstrate the extreme sensitivity of our system to small scale changes in antenna position, indicating that at these frequencies the ice/air surface may not necessarily be modelled as a perfect plane. Any successful experiments performed to monitor such effects as stress induced anisotropy, bedrock roughness or internal structure will require a large data redundancy simply to overcome the random effects introduced at the ice/air surface.

A common thread running through all of this work has been the failure of our photographic recording procedures to provide reliable and recoverable data. We can strongly recommend that future experiments be performed with some alternative recording medium, preferably magnetic tape, with capabilities for both continuous recording for airborne surveys (analogous to Z-scope), and spot recording for surface experiments (analogous to A-scope). We are, in fact, presently developing both types of recorders as two separate systems. The first is based on a 4 channel FM transport and the second on a digital cassette transport.

LITERATURE CITED

Bailey, J. T., and others. 1964. Radio-echo sounding of polar ice sheets, by J. T. Bailey, S. Evans and G. de Q. Robin. Nature, Vol. 204, No. 4957, p. 420-21.

Beckmann, P., and Spizzichino, A. 1963. The scattering of electromagnetic waves from rough surfaces. Oxford, Pergamon Press.

Bentley, C. R. 1979. Ice studies: Visit to the Radio Physics Laboratory of the Arctic and Antarctic Research Institute in Leningrad. EOS Transactions, American Geophysical Union, Vol. 60, No. 10, p. 151.

Berry, M. V. 1972. On deducing the form of surfaces from their diffracted echoes. Journal of Physics A: General Physics, Vol. 5, p. 272-91.

Berry, M. V. 1973. The statistical properties of echoes diffracted from rough surfaces. Philosophical Transactions of the Royal Society of London, A, Vol. 273, No. 1237, p. 611-54.

Campbell, K. J., and Orange, A. S. 1974. The electrical anisotropy of sea ice in the horizontal plane. Journal of Geophysical Research, Vol. 79, No. 33, p. 5059-63.

Clarke, G. K. C., and Goodman, R. H. 1975. Radio echo soundings and ice-temperature measurements in a surge-type glacier. Journal of Glaciology, Vol. 14, No. 70, p. 71-78.

Clarke, G.K.C., and Narod, B.B. Unpublished. Mt. Logan radar survey, or the operation was a success but the patient died. [Internal report, Department of Geophysics and Astronomy, University of British Columbia, Vancouver, Canada, September 1976.]

Clough, J. W. 1977. Radio-echo sounding: reflections from internal layers in ice sheets. Journal of Glaciology, Vol. 18, No. 78, p. 3-14.

Davis, J. L. Unpublished. The problem of depth sounding temperate glaciers. [M.Sc. thesis, University of Cambridge, 1973.]

Davis, J. L., and others. 1973. Radio echo sounding of a valley glacier in East Greenland, by J. L. Davis, J. S. Halliday and K. J. Miller. Journal of Glaciology, Vol. 12, No. 64, p. 87-91.

Delco. 1971. 28 volt Darlington switching regulator. Delco Electronics application note #49, December 1971

Evans, S. 1965. Dielectric properties of ice and snow - a review. Journal of Glaciology, Vol. 5, No. 42, p. 773-92.

Goodman, R. H. 1975. Radio echo sounding on temperate glaciers. Journal of Glaciology, Vol. 14, No. 70, p. 57-70.

Goodman, R. H. and others. 1975. Radio soundings on Trapridge Glacier, Yukon Territory, Canada, by R. H. Goodman, G. K. C. Clarke, G. T. Jarvis, S. G. Collins and R. Metcalfe. Journal of Glaciology, Vol. 14, No. 70, p. 79-84.

Gradshteyn, I. S., and Ryzhik, I. M. 1965. Tables of Integrals, Series, and Products. New York, Academic Press.

Gudmandsen, P, and others. 1976. New equipment for radio-echo sounding, by P. Gudmandsen, E. Nilsson, M. Pallisgaard, N. Skou, and F. Sondergaard. Electromagnetic Institute, the Technical University of Denmark, Lyngby, D 257, 5 p. [reprinted from the Antarctic Journal, X(5), 1975, p. 234-6.]

Harrison, C. H. 1973. Radio echo sounding of horizontal layers in ice. Journal of Glaciology, Vol. 12, No. 66, p. 393-97.

Huynen, J. R. 1978. Phenomenological theory of radar targets. (Uslenghi, P. L. E. ed.) Electromagnetic Scattering. New York, Academic Press, p.653-712.

Jasik, H. ed. 1961. Antenna engineering handbook. New York, McGraw - Hill.

Johari, G. P., and Jones, S. J. 1975. Effects due to double refraction in echo-sounding of ice. Glaciology Division, Dept. of the Environment, Report No. 113-75G, 562 Booth St., Ottawa, Canada.

Longhurst, R. S. 1957. Geometrical and physical Optics. London, Longmans.

Myers, R. ed. 1975. The radio amateur's handbook, fifty-second edition. American Radio Relay League, Newington, Conn.

Napoleoni, J. G. P., and Clarke, G. K. C. 1978. Hot water drilling in a cold glacier. Canadian Journal of Earth Sciences, Vol. 15, No. 2, p. 316-21.

Narod, B. B. Unpublished. UHF radio echo sounding of glaciers. [M.Sc. thesis, University of British Columbia, 1975.]

Nye, J. F., and others. 1972. Proposal for measuring the movement of a large ice sheet by observing radio echoes, by J. F. Nye, R. G. Kyte and D. C. Threlfall. Journal of Glaciology, Vol. 11, No. 63, p. 319-25.

Oswald, G. K. A. Unpublished. Radio echo studies of polar glacier beds. [Ph.D. thesis, University of Cambridge, 1975.]

Panofsky, W. K. H., and Phillips, M. 1962. Classical electricity and magnetism. Reading, Mass., Addison-Wesley.

Robin, G. de Q. 1975. Radio-echo sounding: glaciological interpretations and applications. Journal of Glaciology, Vol. 15, No. 73, p. 49-64.

Sharp, R. P. 1960. Glaciers. Eugene, Oregon, University of Oregon Press.

Smith, B. M. E., and Evans, S. 1972. Radio echo sounding: absorption and scattering by water inclusions and ice lenses. Journal of Glaciology, Vol. 11, No. 61, p. 133-46.

Sondergaard, F., and Skou, N. 1976. Radioglaciology side-looking radar imaging and depth soundings of ice at 300 MHz. Electromagnetics Institute, the Technical university of Denmark, Lyngby, R 170, 51 p.

Stratton, J. A. 1941. Electromagnetic Theory. New York, McGraw - Hill.

Swithinbank, C. 1968. Radio echo sounding of Antarctic glaciers from light aircraft. Union Geodesique et Geophysique Internationale. Association Internationale d'Hydrologie Scientifique. Assemble generale de Berne, 25 Sept.-7 Oct. 1967. [Commision de Neiges et Glaces.] Rapports et discussions, p. 405-14.

Waite, A.H. 1966. International experiments in glacier sounding, 1963 and 1964. Canadian Journal of Earth Sciences, Vol. 3, No. 6, p. 887-92.

APPENDIX 1: DETAILS OF THE RADIO ECHO SOUNDER

A1.1 GENERAL DESCRIPTION AND OPERATION

This appendix is divided into five sections. The first section is an operations notice which details how to connect the various pieces of the radio echo sounder and how to operate the complete system. In principle this is the only section with which the new user need be concerned. The remaining four sections deal in detail in turn with the transmitter, the receiver, the regulating power supply and the antenna. They should be consulted when more than a basic knowledge of the component is required. These sections include complete circuit diagrams of each part as well as functional descriptions of all circuitry.

This appendix is intended to be an exact specification and description of the radio echo sounder as used during the 1976 field project, however it has been written so that a user of the radio echo sounder other than the author will be able to operate and service the sounder, the latter at least in components where user servicing is possible.

A1.1.1 SYSTEM ASSEMBLY

POWER SUPPLY AND DISTRIBUTION

The power for the radio echo sounder and any auxiliary instruments is distributed by the switching regulator. Power is fed into the regulator via one of the five standard circular connectors on the regulator front panel. The connector with the male insert receives the incoming power while the four connectors with female inserts are used as power outputs.

In each connector there are five pins. Pin A of each connector is connected to the output of the switching regulator. The pin B's are all connected to the input power, while the pin E's are connected to the ground reference. In normal use the transmitter always draws power from the output of the regulator on pin A while the receiver and the oscilloscope draw unregulated power from pin B. The additional connector is available for auxiliary instruments. Pin C and D of each connector are reserved for future expansion.

The assembled radio echo sounder (Fig. A1.1) will run off any power source which can provide 10A at 22 V to 28 V, for example two automotive batteries connected in series or a 10A, 28 V auxiliary circuit in an aircraft. Since each power source usually has its own system for connection, care must be taken when connecting it to the switching regulator. The polarity of the power connection must not be reversed. An incorrect connection will destroy the high-power switching transistor in the regulator. When properly connected and functioning the

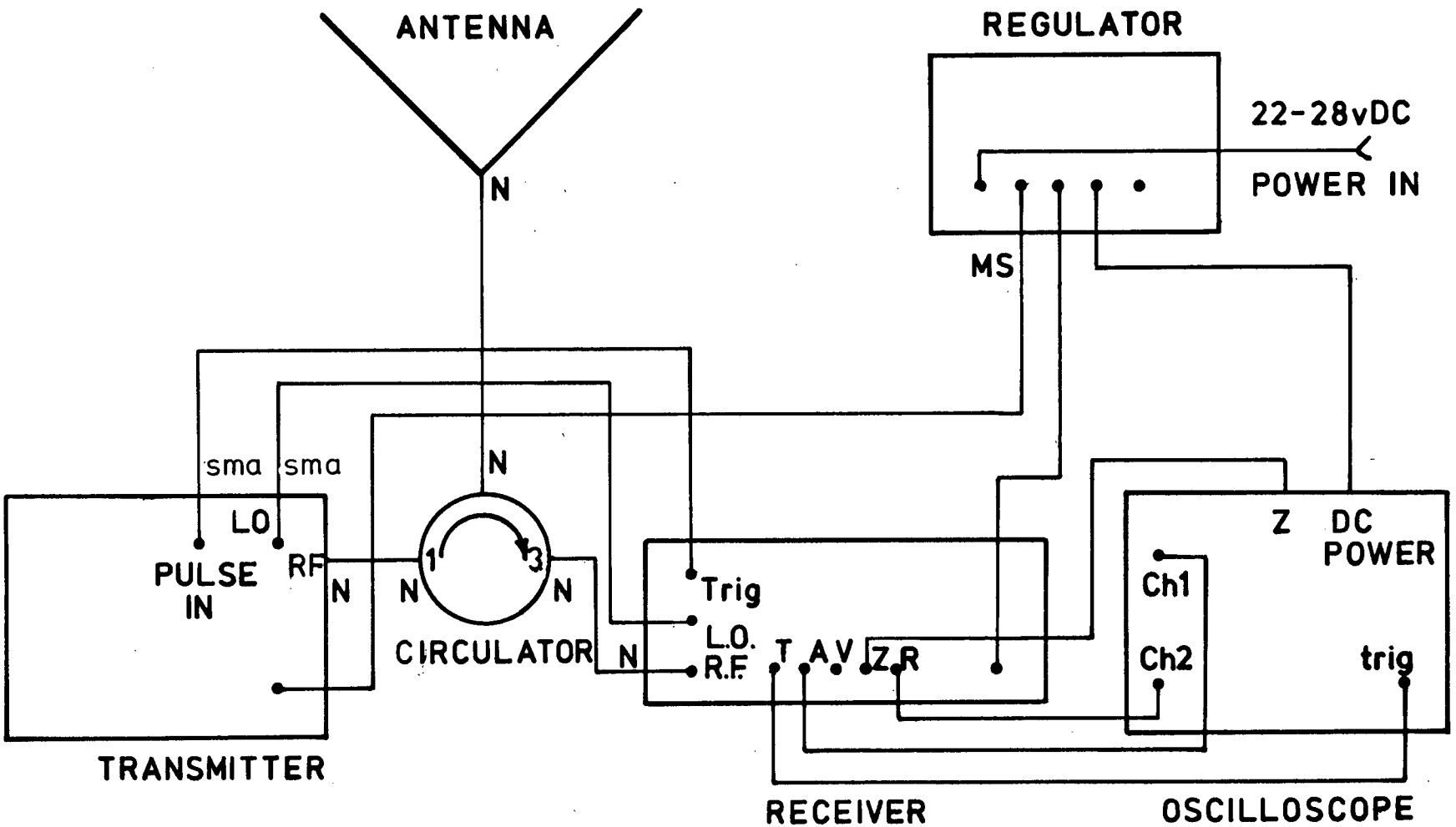

FIG.A1.1 RADIO ECHO SOUNDER BLOCK DIAGRAM

regulator will emit a high-pitched whine caused by high frequency contractions of the flyback inductor. The input and output voltages can be monitored by setting the monitor switch in either position B or A respectively and observing the voltage on the panel meter.

Should the regulator fail for any reason (other than short circuits or power diode failure) it would still be possible to operate the radio echo sounder provided the input voltage exceeds 27 V. When the system is reconnected correctly the regulator output voltage which tracks the input voltage will then be over 26 V which is sufficient to drive the transmitter. The panel meter is diode protected so that it should always function satisfactorily.

Connection procedure should be as follows: Arrange for connection to a suitable power source. Carefully check polarity and connect the regulator to the source. Listen for the high pitched whine and use the selector switch and panel meter to check that the input and output voltages are at suitable levels. Using provided cables connect the transmitter, receiver, oscilloscope and auxiliary instruments to the regulator. Check briefly that each instrument operates normally (all instruments have panel lamp power indicators). Make sure that the oscilloscope power selector switch is set to 24 VDC. If any instrument fails to function check that its fuses are satisfactory.

R. F. CONNECTIONS

Usually the radio echo sounder is operated with a single antenna. In this case both the transmitter and receiver must be connected to the antenna via a circulator.

A circulator is a passive T/R switching device with at least three ports. The construction is such that power fed into port 1 exits from port 2, and power fed into port 2 exits from port 3. With the provided circulator, power from the transmitter is fed into port 1. The transmitted pulse exits from port 2 which is connected to the antenna. The transmitted pulse is radiated from the antenna. The reflected power is received at the antenna and fed back into port 2. The received power then exits from port 3 which is connected to the receiver. The system is not perfect in that the port 1 to 3 isolation is only about 25 dB so that about 12 w from the transmitter plus any power from reflections due to antenna impedance mismatch will be fed directly into the receiver input. In the event of an antenna cable failure a 4 Kw spike would be reflected into the receiver input. This situation has been anticipated, and in the receiver design protection circuitry capable of withstanding the high power shock has been installed. The transmitter is also fully protected by an isolator against R.F. power being reflected back into it (an isolator is simply a circulator with a dummy load on port 3).

All of the high-power R.F. connections in the radio echo sounder use type N connectors and RG-8U or RG-213U cables. When operating from a hookmount on a helicopter an additional GR

connector link should be installed near the antenna in the antenna feed line. The GR link comprises a type N female to GR adapter and a GR to type N male adapter. The friction coupling in the GR connection effects a "weak link". In the event that the pilot of the helicopter is forced to jettison the antenna the GR connection will open and break the cable link to the antenna.

The R.F. connections should be made as follows: Using a type N male-male adapter and an optional type N right-angle adapter connect the transmitter R.F. output to port 1 of the circulator. Using a 1 meter type N cable connect the receiver R.F. input to port 3 of the circulator. Connect a 5 meter cable to port 2 of the circulator and run the cable to the antenna. The cables within the antenna itself should be taped to the antenna reflector to relieve strain. The antenna connection itself uses two type N "Tee" adapters and a tuning stub. The connection can be articulated to allow for a convenient approach by the antenna feed line. If required install the weak link connection on the antenna and connect the free end of the antenna feed line. Caution: when operating, the radio echo sounder radiates sufficient R.F. power to be considered hazardous. Do not stand in front of the antenna while the radio echo sounder is operating.

REMAINING RECEIVER TO TRANSMITTER CONNECTIONS

In addition to the R.F. connection there are two other

connections between the transmitter and the receiver. One is the local oscillator power, the other is the transmission trigger pulse.

The local oscillator (L.O.) power is generated in the transmitter and is frequency-locked to a 120 MHz crystal oscillator also in the transmitter. The latter provides a reference for both the 720 MHz L.O. and the 840 MHz transmitter carrier frequencies. The connection, made by attaching an RG-58 SMA cable to the sockets marked "L.O." on each of the transmitter and the receiver, provides 160mW of L.O. power to a mixer in the receiver which converts the received R.F. signal to the 120 MHz receiver intermediate frequency (I.F.).

The transmission trigger pulse is generated in the receiver logic circuitry. It has been preset to 50ns pulse length and is capable of driving 5 V into a 50Ω load. This pulse triggers the medium power R.F. amplifier as well as gating the high power R.F. amplifier. In this way the R.F. pulse length is externally adjustable while maintaining a high on/off ratio for detecting signals after long delays. The connection is made by attaching a second RG-58 SMA cable to sockets marked "PULSE IN" on the transmitter and "Trig" on the receiver.

OSCILLOSCOPE CONNECTIONS

Five BNC connectors on the receiver front panel provide all the signals required to make photographic records from a Tektronix 475 oscilloscope. They have been marked "T", "A",

"Z", "V", and "R". The functions of each is described in the following paragraphs.

The connector marked "T" is a twin of the SMA connector marked "Trig". It serves as a backup trigger source to the latter as well as a trigger for the oscilloscope. Its electrical properties are identical with "Trig".

The "A" connector carries the unmodified video output of the I.F. amplifier-detector strip in the receiver. The impedance is 93 Ω and the signal stays between 0 and +3 V with 40 MHz bandwidth. The A signal is used for all "A-scope" records (X-Y photos of power vs. time).

The "Z" connector carries the output of the video amplifier. It is normally used only as a monitor of the video signal.

The "V" connector carries a signal called "mixed video". It is identical in nature to the Z signal except that a frame code or grey scale can be momentarily switched into the data stream. Both the V and Z signal can be used to modulate the intensity of the phosphor brightness.

The "R" connector carries a slowly varying ramp which is used to scan an intensity modulated line trace vertically across the oscilloscope screen. This signal is used when continuous records are required.

Connecting the oscilloscope into the radio echo sounder system requires four BNC cables which should be deployed as follows. Connect the receiver "T" output to the "external trig" connector on the oscilloscope (lower right). Set the oscilloscope trigger source on "EXT", coupling on "DC", slope on

positive, mode on "AUTO" and horizontal mode on "A locks knob". Connect the receiver A output to the oscilloscope Ch1 input. Set the Ch1 attenuator at 0.5 V/div with DC coupling. Connect the R output to the oscilloscope Ch2 input. Set the Ch2 attenuator at 2 V/div with DC coupling. Connect the V output to the oscilloscope Z-axis input (rear of instrument).

A1.1.2 OPERATION OF THE RADIO ECHO SOUNDER

INITIAL SETUP

After assembly several steps must be taken before any photographic records are to be taken. The procedure which follows need be done only at the beginning of operation.

Turn on the power for the transmitter and the oscilloscope. The flashing light on the transmitter indicates that it is in its warmup cycle. During this period the high voltage supply in the transmitter is disabled. At the end of this warmup period the lamp will stay on continuously.

Turn on the power for the receiver. On the oscilloscope select Ch1 as the vertical source. Adjust the trigger level so that the echogram is stable. Adjust the vertical position to midframe. Set the timebase on 1 us/div or 500 ns/div depending on the expected ice thickness. Set the bandwidth to 100 MHz or 20 MHz depending on signal to noise and resolution requirements (20 MHz gives better signal to noise, 100 MHz gives better resolution). Attach the Polaroid camera to the oscilloscope.

The oscilloscope is now set up for A-scope photographs.

Only one additional initial adjustment is required for I-scope recording. Select Ch2 as the vertical source, uncouple the Ch2 signal (set switch to GND), adjust the vertical trace position to three graticule divisions below centre, recouple the Ch2 signal to DC.

A-SCOPE RECORDING

To make an A-scope photograph use the following procedure. Select Ch1 as the vertical source. Adjust the screen brightness to medium brightness. Close the camera onto the oscilloscope. Set the shutter speed at 1/60 s. Set the aperture at f:4 (approximate). Operate the camera in the usual manner. Getting a well exposed frame may require several attempts before the operator is familiar with the required brightness/aperture combination.

Z-SCOPE RECORDING

In this mode it is possible to use the Polaroid camera to make continuous records. Select Ch2 as the vertical source. Adjust the screen brightness to the minimum brightness while maintaining signal visibility. The operator may choose to use the grey scale as a source for setting the brightness. Depressing the momentary "GREY SCALE" toggle switch will switch the grey scale into the video signal. This shows up as an eight

step staircase starting with the brightest step at the left of the screen.

Set up the receiver as follows. Select a duration for each record using the rotary switch. One minute is typical. Using the "RESET" and "RUN" switches preset the frame code to one less than the required starting frame number. The frame code is displayed in octal on the receiver. The receiver will automatically increment the frame count after each depression of the "START" switch.

To expose a frame first close the camera onto the oscilloscope, set the shutter speed at "T" (time exposure) and the aperture at f:16. Press the shutter release and depress the "START" switch on the receiver. This action will cause the frame code to increment by one and the "READY" lamp to extinguish. When the "READY" lamp has relit press the shutter release again. This action closes the camera shutter. After removing the film frame the cycle is ready to be repeated. With practice the entire procedure can be accomplished in less than ten seconds.

Examination of an I-scope photograph will reveal the following. Each record starts at the bottom of the screen by exposing first the grey scale, then the frame code into the picture. This process uses 1/16th of the total record time.

A1.2 THE TRANSMITTER

In principle the radio echo sounder transmitter (Fig. A1.2) is simply a gated R.F. oscillator. Its sophistication results from its high output power level, fast switching times, stable frequency and foolproof, overload-sensitive power supply.

The circuit design and the instrument were provided for the University of British Columbia by Microwave Control Co., New Jersey. The following information has been included here solely for user interest and to aid possible field serviceability. No rights to the design are implied.

A1.2.1 POWER SUPPLY

REGULATORS

The input power regulators provide +26 V and +5 V for the transmitter. The +26 V regulator output (Fig. A1.3) is referenced to Zener diode D1. If the output voltage rises transistor Q1 is biased on which increases the sink current in transistor Q2 thereby pulling down the output voltage. The +5 V regulator (Fig. A1.4) is a simple shunt regulator with transistor Q24 being used as a variable current sink referenced to Zener diode D29.

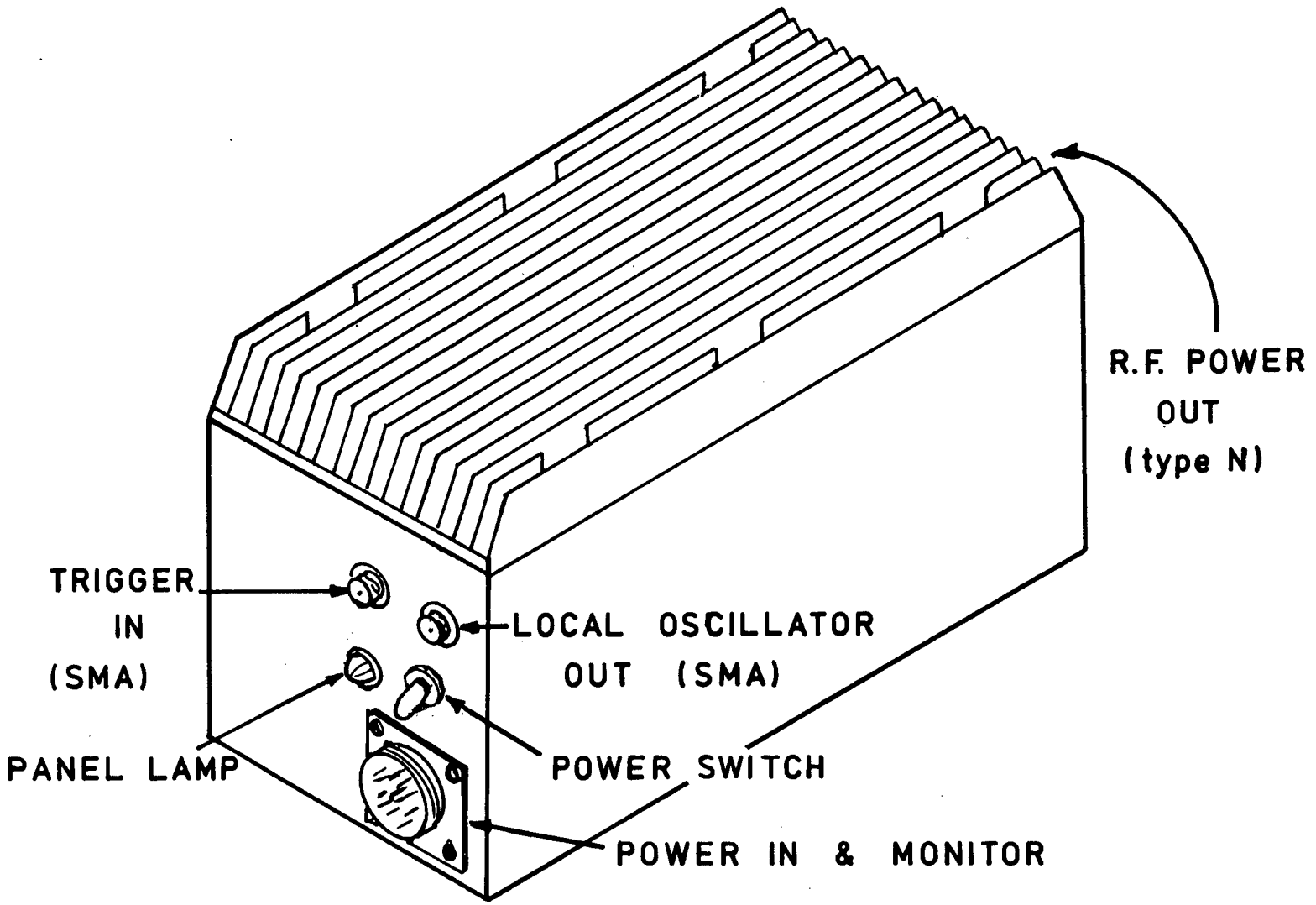

FIG. A1.2 TRANSMITTER: PICTORIAL

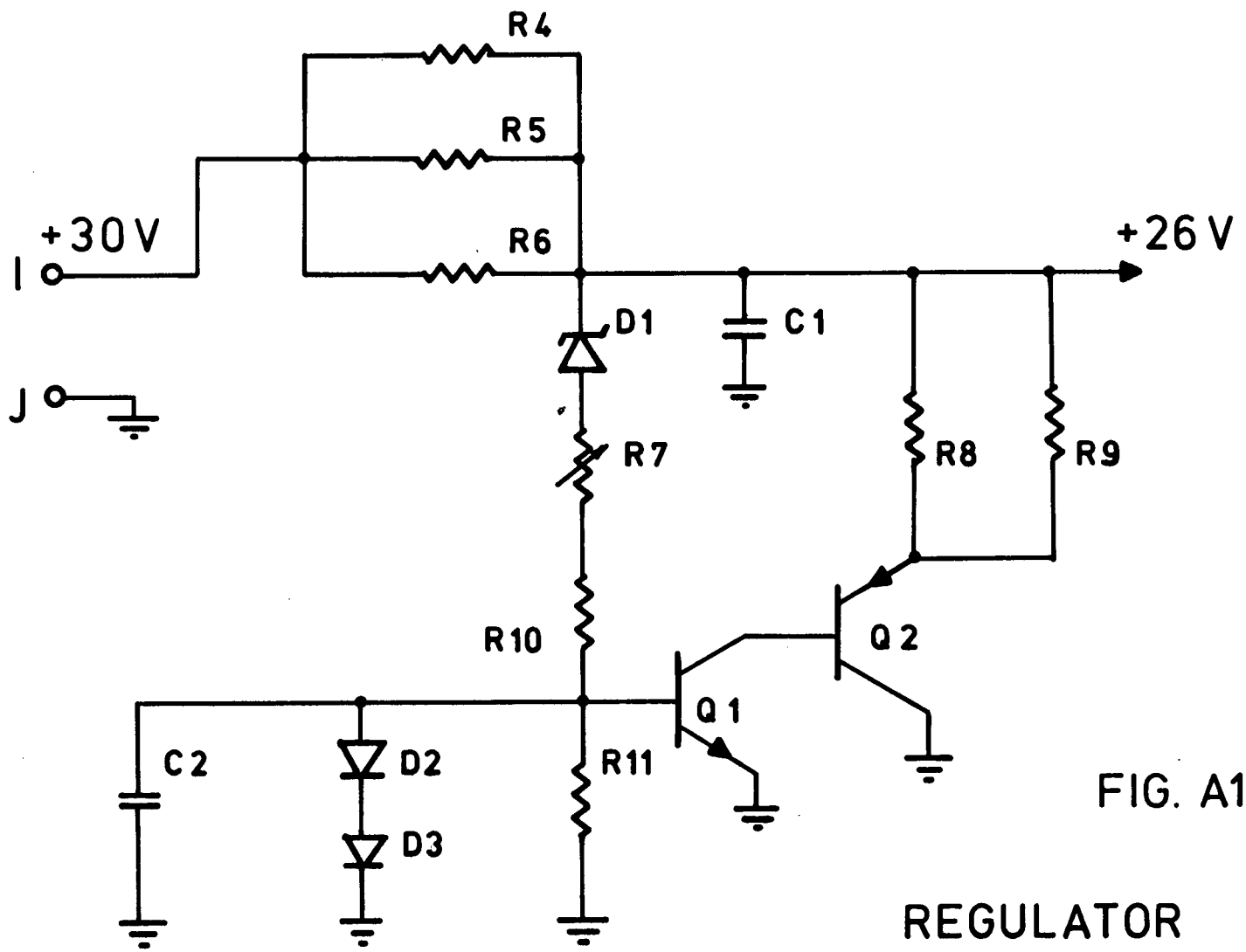

FIG. A1.3

REGULATOR
CIRCUIT DIAGRAM

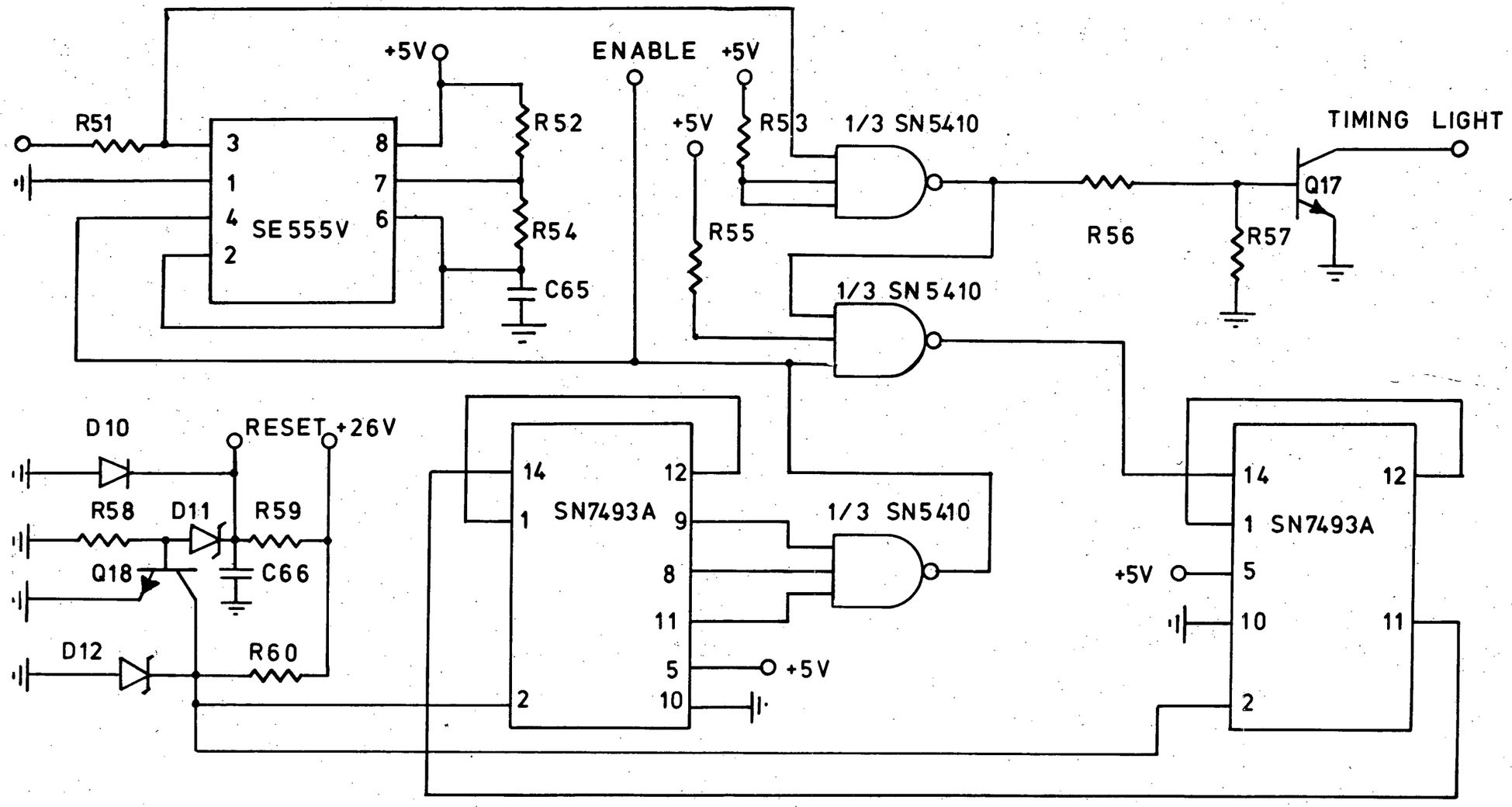

POWER SUPPLY TIMING CIRCUIT SCHEMATIC DIAGRAM

FIG. A1.4

WARM-UP TIMING CIRCUIT

When power is first applied to the transmitter the high voltage power supply is disabled to allow time for the triode filaments to warm up. A digital circuit (Fig. A1.4) delays the high voltage enable for approximately two minutes. At power-up capacitor C66 is discharged forcing transistor Q18 to be switched off. As a result pull-up resistor R60 and Zener diode D12 ensure a TTL high logic level on reset pin 2 of each SN7493 hex counter. Thus as power-up both counters are reset. Reset circuit relaxation then turns on transistor Q18 and the reset lines are brought to a low level.

An SE555V timer provides a start-up cycle clock. At power-up the count enable line is low and the SE555V is in astable vibration. The open collector output on pin 3 drives a NAND gate used as an inverter. The output on the NAND gate drives the base of transistor Q17 through resistor R56. Transistor Q17 drives the front panel timing light causing it to flash on and off at the count frequency. The clock pulse is inverted again in a NAND gate and drives the clock input (pin 14) of an SN7493A counter. The Q4 output provides a clock pulse for the second SN7493A counter. The Q2, Q3 and Q4 outputs of the second counter are "NAND"ed to determine the ENABLE level. When the count reaches hex'E0' the ENABLE level goes low resetting the SE555V multivibrator and forcing a high clock input on the first SN7493A counter. A low level from the multivibrator is inverted and turns on transistor Q17 continuously. At this time the panel lamp remains on continuously indicating the end of the

warm-up period.

POWER SUPPLY DRIVER

All power supplies are constructed using step-up/isolation transformers. Currents in the primary windings are switched by transistors Q19, Q20, Q21 and Q22 (Fig. A1.5). Pulses to drive these transistors are derived in the power supply driver.

The basic transformer frequency is determined by an MC4324 astable multivibrator and a J-K flip-flop (1/2 SN5473) (Fig. A1.6). The Q and $\bar{Q}$ outputs of the flip-flop alternately enable pulses onto the bases of transistors Q26 and Q28 in the high voltage drive, and transistors Q30 and Q32 in the low voltage drive.

Duty cycles for the high and low voltage drives are independently determined by two monostable vibrators in a SN54123. The two monostable vibrators are triggered simultaneously with state changes in the J-K flip-flop. The pulse length for the low voltage supply drives is preset by resistors R82 and R84 and capacitor C78. The output of this vibrator (pin 4) is normally high and goes low when the vibrator is triggered. When low both transistors Q30 and Q32 are switched on pulling down emitter-follower transistors Q29 and Q31. At this time both transistors Q19 and Q20 are switched off and no current flows in the primary winding of the low voltage power transformer.

At the end of the monostable cycle the output of one of the

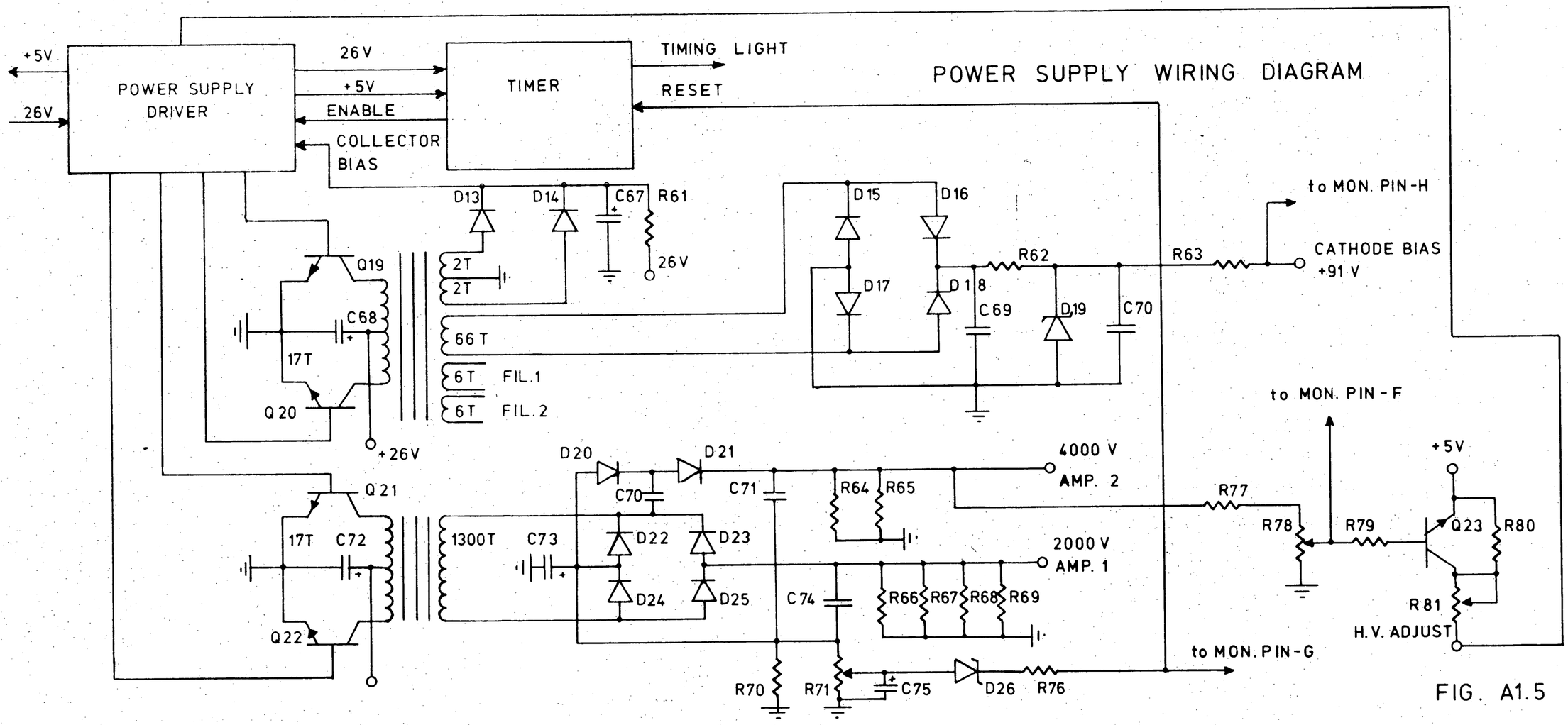
POWER SUPPLY WIRING DIAGRAM
+5V
26V
POWER SUPPLY DRIVER
26V
+5V
ENABLE
COLLECTOR BIAS
TIMER
TIMING LIGHT
RESET
D13
D14
C67
R61
26V
2T
2T
Q19
C68
17T
Q20
66 T
6T FIL.1
6T FIL.2
+26V
D15
D16
D17
D18
C69
D19
C70
R62
R63
to MON. PIN-H
CATHODE BIAS +91 V
Q21
17T
C72
Q22
1300T
C73
D20
D21
C70
D22
D23
D24
D25
C71
R64
R65
4000 V AMP. 2
2000 V AMP. 1
C74
R66
R67
R68
R69
R70
R71
C75
D26
R76
to MON. PIN-G
to MON. PIN-F
+5V
R77
R78
R79
Q23
R80
R81
H.V. ADJUST

FIG. A1.5

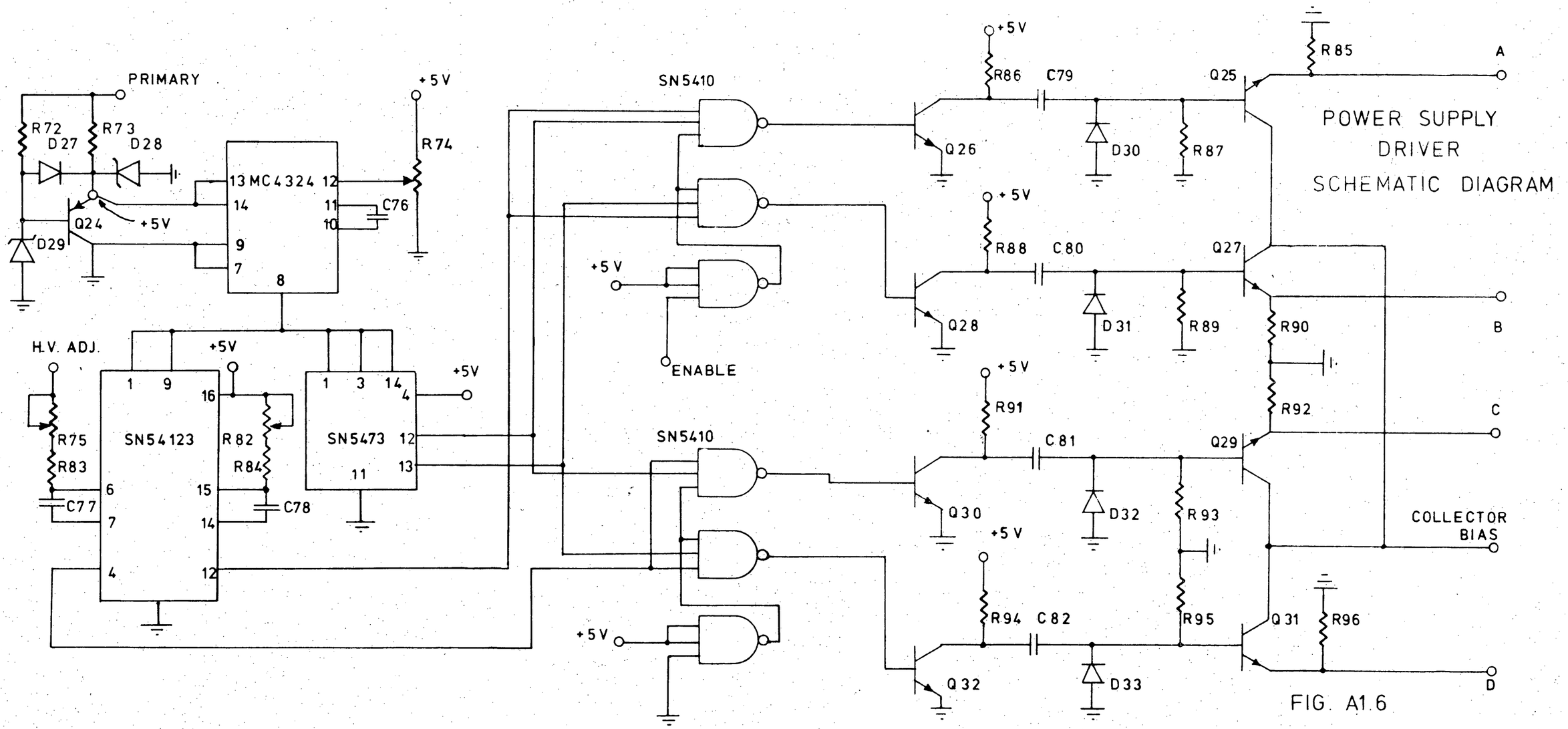
PRIMARY
R72
D27
R73
D28
Q24
D29
+5V
13 MC4324 12
14
11
10
9
7
8
C76
R74
+5V
H.V. ADJ.
+5V
1 9
16
SN54123
R75
R83
R82
R84
C77
C78
6
7
15
14
4
12
1 3 14
4
SN5473
12
13
11
+5V
SN5410
+5V
ENABLE
SN5410
+5V
+5V
R86
C79
Q26
D30
R87
Q25
R85
A
POWER SUPPLY
DRIVER
SCHEMATIC DIAGRAM
+5V
R88
C80
Q28
D31
R89
Q27
R90
B
R92
C
+5V
R91
C81
Q30
D32
R93
Q29
COLLECTOR
BIAS
+5V
R94
C82
Q32
D33
R95
Q31
R96
D

FIG. A1.6

NAND gates driven by the monostable vibrator goes low, switching off one of the transistors Q30 or Q32 and through transistor Q29 or Q31 switching on one of transistors Q19 or Q20. Adjusting variable resistor R82 varies the standby time of the multivibrator, which varies the RMS output voltage of the transformer without varying the peak output voltage. Source voltage for the collectors of transistors Q25, Q27, Q29 and Q31, after start-up from resistor R61, comes from diodes D13 and D14 and capacitor C67.

The high voltage supply is turned on when the ENABLE line, derived in the timer, goes low. In the same manner as in the low voltage supply, the high voltage supply duty cycle is controlled by a monostable vibrator. The high voltage supply, however, is feedback regulated. If the +4 KV supply tries to go too high the voltage on the tap of variable resistor (Fig. A1.7) R78 approaches +5 V and transistor Q23 switches off. This effectively increases the series resistance to multivibrator pin 6 (R81 and R75 are one resistor, shown twice in the two separate drawings), increasing the monostable cycle time and reducing the standby time. This reduces the power available to the high voltage power transformer primary winding forcing the high voltage output to drop.

LOW VOLTAGE SUPPLY

The low voltage supply (Fig. A1.5) provides two filament supplies and a +91 V cathode bias supply. The filament supplies

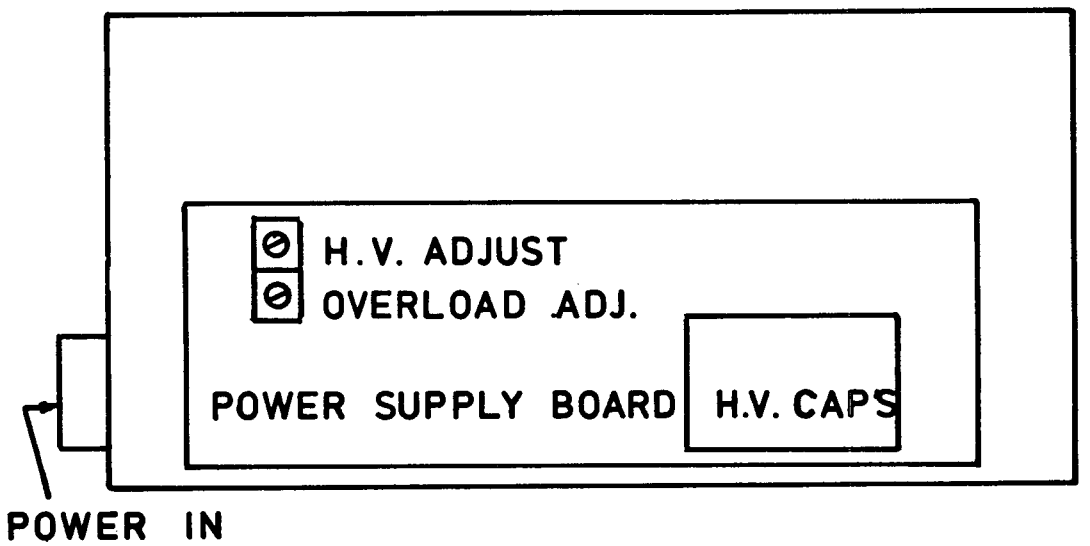

RIGHT SIDE

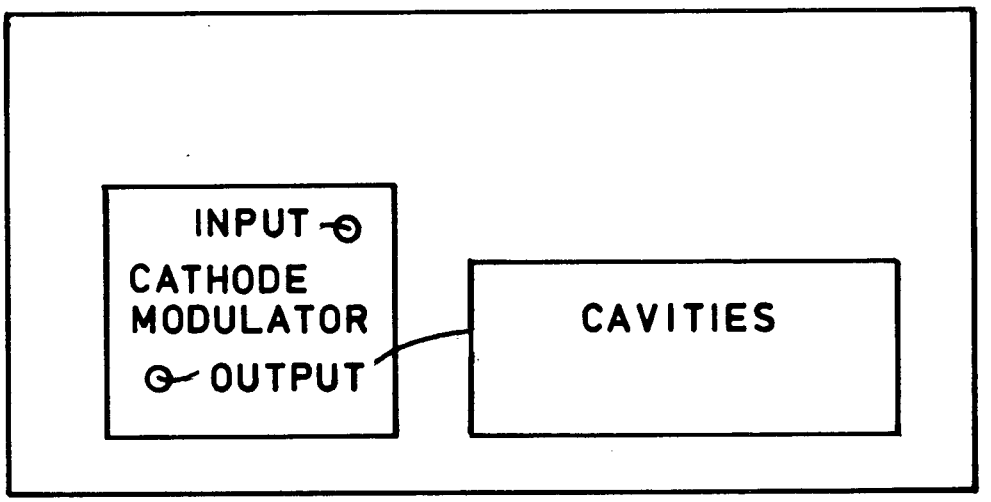

LEFT SIDE

TRANSMITTER: INTERNAL LAYOUT

(NOT TO SCALE)

FIG. A1.7

are unregulated after the +26 V regulator. Filament currents to the two triodes are controlled by variable resistors R2 and R3.

The cathode bias supply includes a full wave rectifier using diodes D15, D16, D17 and D18 and storage capacitor C69. The supply is shunt regulated by Zener diode D19 and resistor R62. Excessive power wastage is avoided in a manner described previously.

HIGH VOLTAGE SUPPLY

The high voltage supply (Fig. A1.5) provides a +2 KV supply for the first triode amplifier and a +4 KV supply for the final triode amplifier. The +2 KV supply uses four diodes D22, D23, D24 and D25 in a full wave rectifier and storage capacitor C74. The +4 KV supply adds voltage doubler diodes D20 and D21 and storage capacitor C71. The high voltage supply regulation was previously described.

The supply is over-load protected. If the load dissipation increases for any reason the (negative) voltage across current sense resistor R70 also increases. The drop pulls down (through Zener diode D26 and resistor R76) the RESET voltage. If the RESET line drops too low transistor Q18 switches off reinitiating the start-up sequence with ENABLE line high. The overload level is preset by variable resistor R71.

A1.2.2 MODULATOR

The modulator controls separately the gain of two stages of R.F. amplification. The pulse amplifier gates the 20 W solid state R.F. amplifier, and the cathode modulator gates the first triode amplifier. Both modulators take their input signals from the 50 TTL level "PULSE IN" signal.

PULSE AMPLIFIER

The incoming pulse is buffered by a DM8830 line driver, (Fig. A1.8) then amplified/inverted in a push-pull amplifier constructed from transistors Q8 and Q10. Resistor R71 is adjusted so that the pulse length cannot exceed 200ns. The pulse is again amplified/inverted by transistor Q9 which acts as a power switch for the solid state R.F. amplifier. The output voltage swings between 0 and +25 V.

CATHODE MODULATOR

The cathode modulator (Fig. A1.9) is very similar to the pulse amplifier. The incoming pulse is amplified/inverted by transistor Q6. Resistor R16 is set to limit the maximum pulse length to 200 ns. The pulse is amplified/inverted by a push-pull amplifier constructed from transistors Q3, Q4 and Q7. The additional emitter-follower transistor Q4 has been added to the push-pull amplifier to boost the source current drive capability

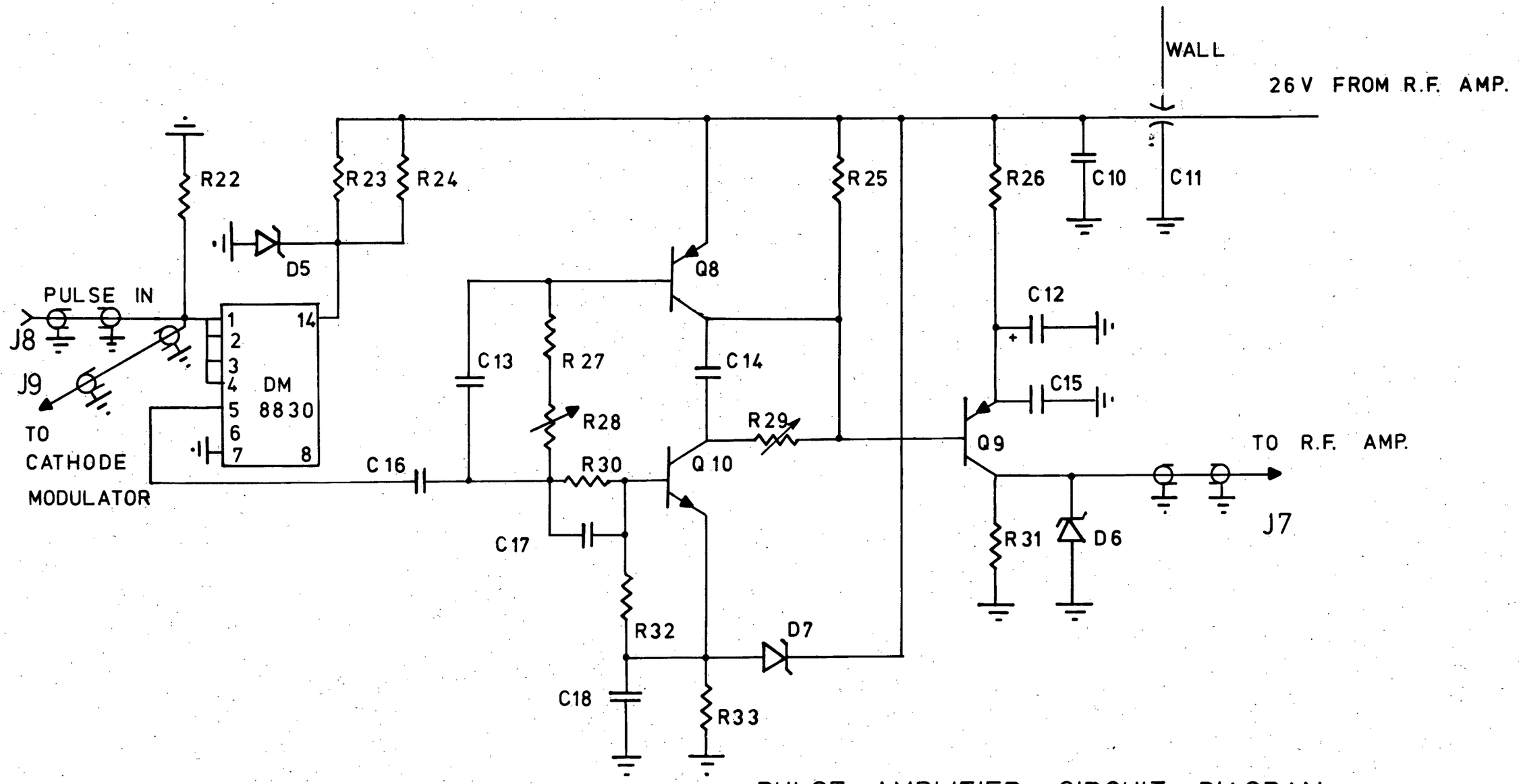

PULSE AMPLIFIER CIRCUIT DIAGRAM

FIG. A1.8

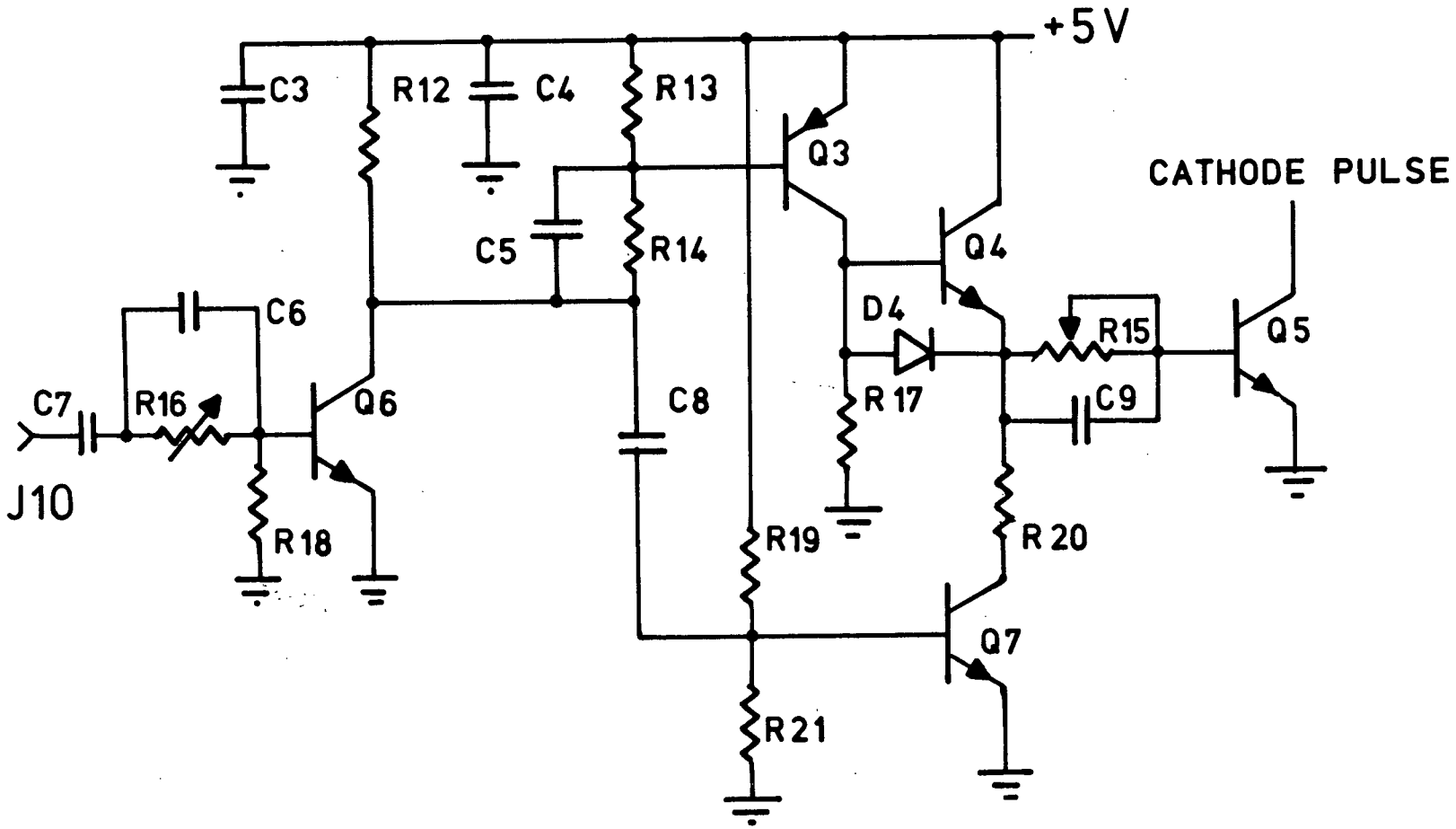

CATHODE MODULATOR CIRCUIT DIAGRAM

FIG. A1.9

to transistor Q5. Transistor Q5 is the final stage of pulse amplification. Q5 is a high-gain, high-power transistor with collector load including resistor R1 and the first triode cathode.

A1.2.3 THE R.F. CHAIN

The R.F. chain derives the carrier and local oscillator frequencies by multiplying the frequency of a 120 MHz crystal oscillator. The chain can develop 4 KW output power into 50 at 840 MHz.

THE 120MHZ OSCILLATOR-AMPLIFIER

The basic 120 MHz reference frequency is generated by a TTL compatible 120 MHz modular crystal oscillator (Fig. A1.10). The first stage of R.F. amplification uses transistor Q13 as a tuned amplifier, operating class AB. This is followed by three stages of tuned R.F. amplification using transistors Q16, Q15 and Q14. All three amplifiers operate class C. The first class C amplifier uses stripline components in its tuned circuit.

X6, X7 MULTIPLIERS

The 120 MHz output power drives the nonlinear varactor diode D9 (Fig. A1.11). The sixth and seventh harmonics are isolated by stripline tuned circuits. The sixth harmonic is

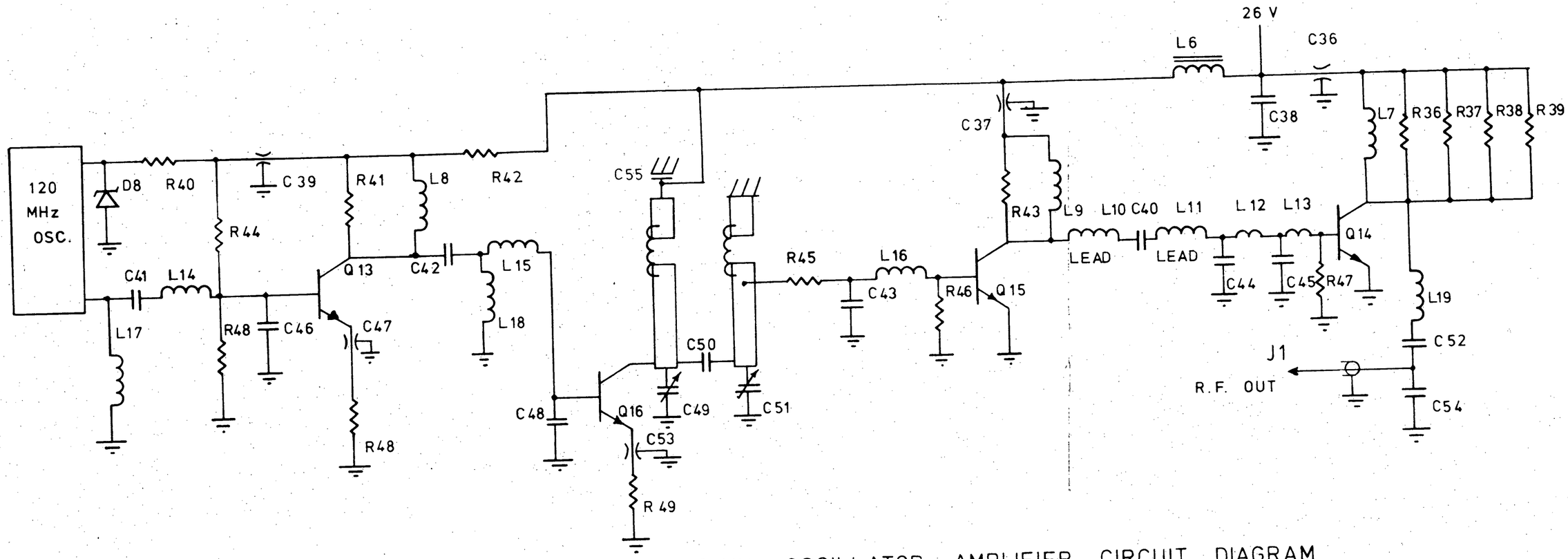

120 MHz OSCILLATOR - AMPLIFIER CIRCUIT DIAGRAM

FIG. A1.10

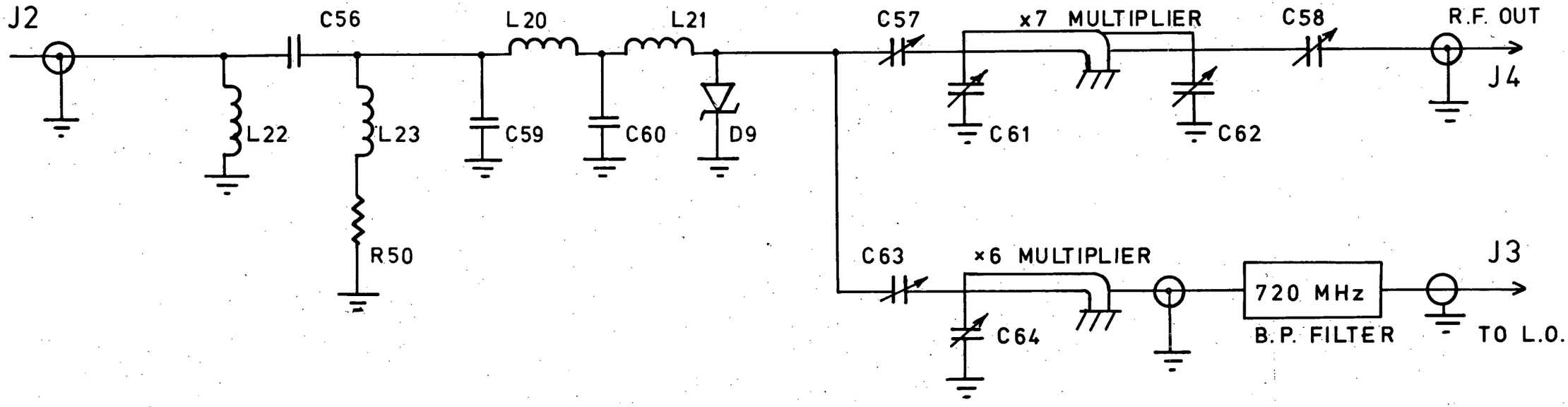

×6, ×7 MULTIPLIER CIRCUIT DIAGRAM

FIG. A1.11

further filtered by a 720 MHz bandpass filter. At this point the 720 MHz power level is 160 mW. This provides the local oscillator power to the receiver.

840MHZ R.F AMPLIFIER

The 840 MHz seventh harmonic from the multiplier is further amplified through two stages of tuned common-base amplification using transistors Q11 and Q12 (Fig. A1.12). The pulse amplifier gates the first stage by switching the collector current on and off.

The output power of the solid state R.F. amplifier section is 20 W. It is isolated from the triode amplifier section by a ferrite isolator.

The high-power R.F. amplifier (Fig. A1.13) uses two microwave cavity triode amplifiers. The cathode modulator gates the first triode amplifier by switching the DC level on the cathode. This switches the triode out of and back into cutoff. The centre frequencies and Q's of the triode amplifiers are set by adjusting their cavity configurations.

The output power of the R.F. chain is 4 KW. It is again isolated by a ferrite isolator and attached to the R.F. output connector.

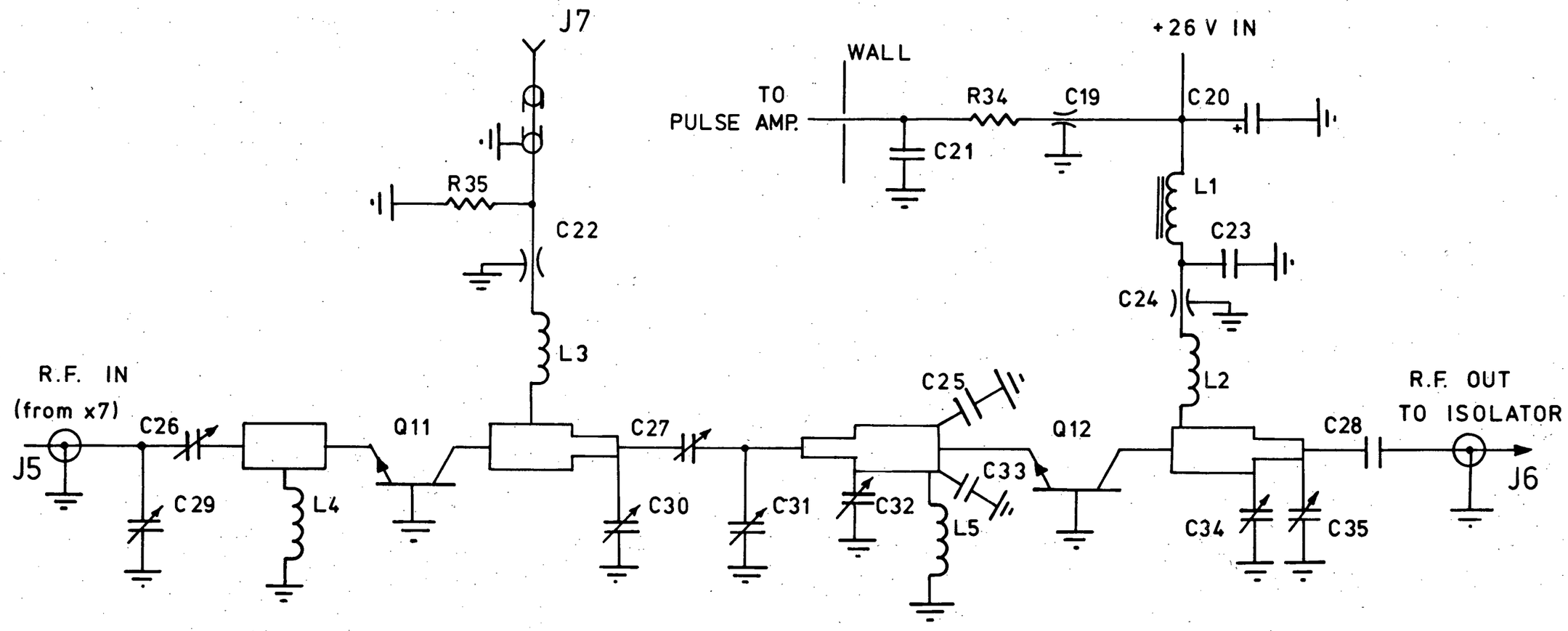

840 MHz R.F. AMPLIFIER CIRCUIT DIAGRAM

FIG. A1.12

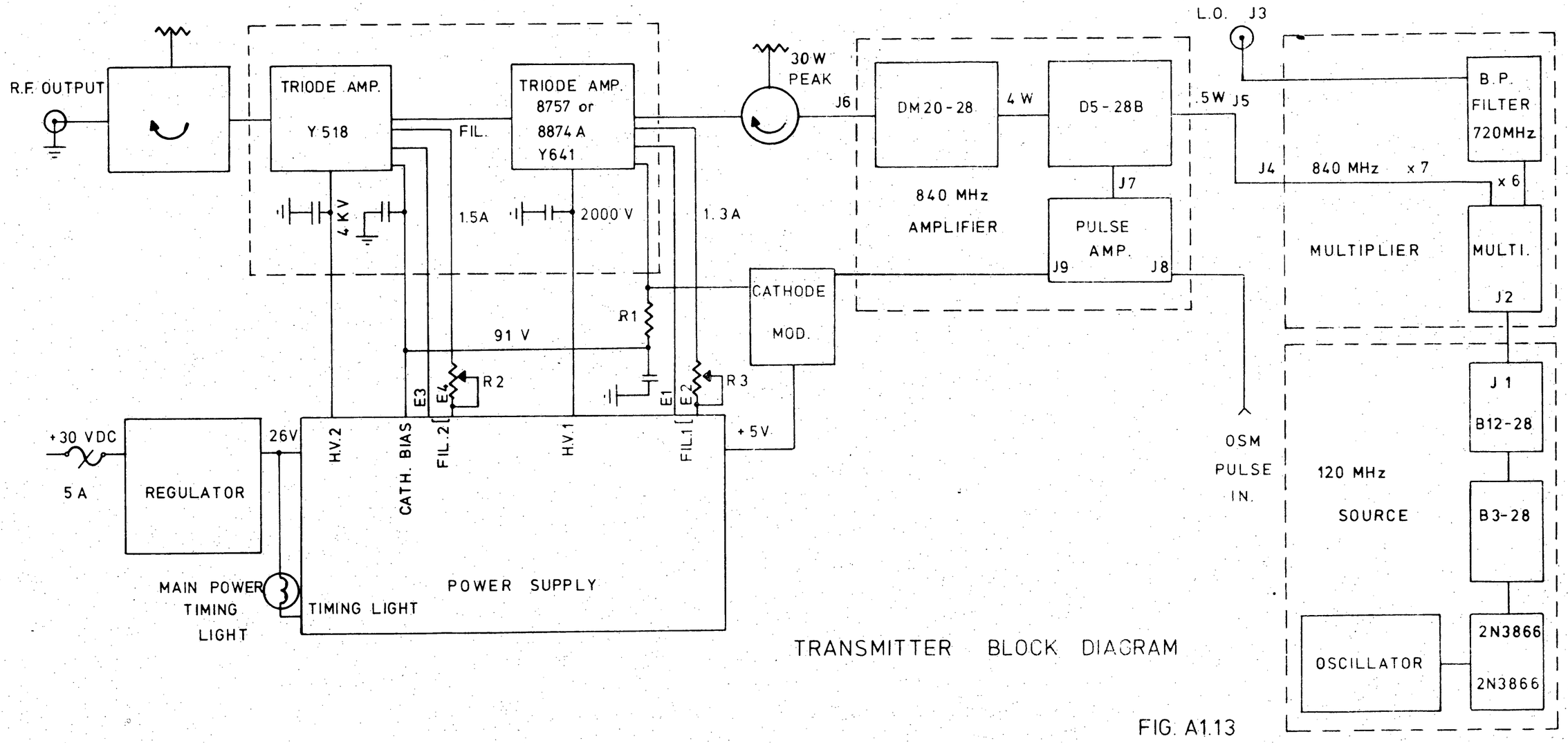

TRANSMITTER BLOCK DIAGRAM

FIG. A1.13

Table A1: Power Connector Pin Designations

DC POWER INPUT

I +30 Volts

J - Return

MONITOR TEST POINTS

A Spare

B, C Filament #1

D, E Filament #2

F HV Monitor

G Reset Line

H Bias Voltage

Table A2: Transmitter: Required Major Components

Y518 Cavity Triode

Y641 Cavity Triode

840 MHz Isolator, 5 KW Peak

840 MHz Isolator, 30w Peak 120 MHz Oscillator

Integrated Circuits:

SN5410 TTL Triple 3-NAND (x3)

SN5473 TTL Dual J-K Flip-flop

SN7493A TTL 4-bit Binary Counter (x2)

SN54123 TTL Dual Monostable Vibrator

MC4324 TTL Dual Voltage Controlled Multivibrator

SE555V MOS Linear Timer

Table A3: Transmitter: Discrete Components Parts List

Q1 MPS-U06	Q23 2N2907
Q2 2N5883	Q24 MPS-U57
Q3 MPS-U57	Q25 MPS-U07
Q4 2N3009	Q26 2N4264
Q5 2N5430	Q27 MPS-U07
Q6 2N4264	Q28 2N4264
Q7 2N3009	Q29 MPS-U07
Q8 MPS-3640	Q30 2N4264
Q9 2N3720	Q31 MPS-U07
Q10 2N3009	Q32 2N4264
Q11 D5-28B	D1 1N5251
Q12 DM20-28B	D2 1N4007
Q13 2N3866	D3 1N4007
Q14 B12-28	D4 1N914
Q15 B3-28	D5 1N5231
Q16 2N3866	D6 1N5253
Q17 2N2222	D7 1N4732
Q18 2N2222	D8 1N5240
Q19 2N3055	D9 VAB-810
Q20 2N3055	D10 1N4007
Q21 2N3055	D11 1N5246
Q22 2N3055	D12 1N5230

TABLE A3 CONT.

D13 1N4007
D14 1N4007
D15 1N4007
D16 1N4007
D17 1N4007
D18 1N4007
D19 1N5377
D20 USR-60
D21 USR-60
D22 100S8F
D23 100S8F
D24 100S8F
D25 100S8F
D26 1N4754
D27 1N4007
D28 1N5234
D29 1N5230
D30 1N914
D31 1N914
D32 1N914
D33 1N914
C1 27 ufd, 35 V
C2 100 ufd, 5 V
C3 10 ufd, 8 V
C4 0.1 ufd
C5 100pfd
C6 4.7pfd
C7 0.05 ufd
C8 0.1 ufd
C9 0.0033 ufd
C10 0.1 ufd
C11 0.001 ufd, feedthrough
C12 27 ufd, 35 V
C13 180pfd
C14 0.0033 ufd
C15 0.1 ufd
C16 0.1 ufd
C17 0.0022 ufd
C18 0.01 ufd
C19 0.001 ufd, feedthrough
C20 50 ufd, 50 V
C21 50 ufd, 50 V
C22 22pfd, feedthrough
C23 0.1 ufd
C24 0.001 ufd, feedthrough
C25 7.5pfd
C26 1-10pfd, variable
C27 1-10pfd, variable
C28 390pfd
C29 1-10pfd, variable

TABLE A3 CONT.

C30 1-10pfd, variable
C31 1-10pfd, variable
C32 1-10pfd, variable
C33 7.5pfd
C34 1-10pfd, variable
C35 1-10pfd, variable
C36 0.001 ufd, feedthrough
C37 0.001 ufd, feedthrough
C38 50 ufd, 50 V
C39 0.001 ufd, feedthrough
C40 27pfd
C41 24pfd, selected
C42 Selected
C43 60pfd
C44 65pfd
C45 450pfd
C46 20pfd
C47 0.001 ufd, feedthrough
C48 20pfd
C49 1-10pfd, variable
C50 51pfd
C51 1-10pfd, variable
C52 270pfd
C53 0.001 ufd, feedthrough
C54 26pfd
C55 200pfd
C56 75pfd
C57 0.1-3pfd, variable
C58 1-10pfd, variable
C59 95pfd
C60 300pfd
C61 1-10pfd, variable
C62 1-10pfd, variable
C63 0.1-3pfd, variable
C64 1-10pfd, variable
C65 22 ufd, 20 V
C66 15 ufd, 35 V
C67 50 ufd, 50 V
C68 22 ufd, 35 V
C69 18 ufd, 150 V
C70 18 ufd, 150 V
C71 0.1 ufd, 5 KV
C72 22 ufd, 35 V
C73 22 ufd, 35 V
C74 0.1 ufd, 3 KV
C75 3.9 ufd,10 V
C76 0.015 ufd, 100 V
C77 910pfd, 20 V
C78 91pfd, 20 V
C79 3.9 ufd, 10 V

TABLE A3 CONT.

C80 3.9 ufd, 10 V

C81 3.9 ufd, 10 V

C82 3.9 ufd, 10 V

L1 RF choke

L2 3 Turns

L3 2 Turns

L4 3.5 Turns

L5 1 Turn

L6 RF choke

L7 8 Turns

L8 6 Turns

L9 8 Turns

L10 3 Turns (leads)

L11 3 Turns (leads)

L12 2 Turns

L13 3/4 Turns

L14 5 3/4 Turns

L15 3 Turns

L16 0.02 uh

L17 6 Turns

L18 8 Turns

L19 Selected

L20 0.02 uh

L21 0.0058 uh

L22 0.022 uh

L23 RF choke

R1 150 0.5w, 10%

R2 0103 Ohmite 3 12w

R3 0103 Ohmite 3 12w

R4 2.25 , 12w

R5 2.25 , 12w

R6 2.25 , 12w

R7 200 variable

R8 4.7, 12w

R9 4.7, 12w

R10 200 0.5w, 10%

R11 62 0.5w, 10%

R12 56 0.5w, 10%

R13 150 0.5w, 10%

R14 Selected

R15 500 variable

R16 2K variable

R17 470 0.5w, 10%

R18 470 0.5w, 10%

R19 270 0.5w, 10%

R20 10 0.5w, 10%

R21 330 0.5w, 10%

R22 56 0.5w, 10%

R23 1800 0.5w, 10%

R24 1800 0.5w, 10%

TABLE A3 CONT.

R25 270 0.5w, 10%

R26 1 0.5w, 10%

R27 470 0.5w, 10%

R28 2K variable

R29 500 variable

R30 100 0.5w, 10%

R31 1K 0.5w, 10%

R32 330 0.5w, 10%

R33 510, 5%, 2w

R34 0.39, wirewound

R35 33 0.5w, 10%

R36 22K 0.5w, 10%

R37 22K 0.5w, 10%

R38 22K 0.5w, 10%

R39 22K 0.5w, 10%

R40 12K 0.5w, 10%

R41 390 0.5w, 10%

R42 68 0.5w, 10%

R43 68 0.5w, 10%

R44 5.6K 0.5w, 10%

R45 6.8 0.5w, 10%

R46 10 0.5w, 10%

R47 10 0.5w, 10%

R48 270 0.5w, 10%

R49 220 0.5w, 10%

R50 Selected

R51 1K 0.5w, 10%

R52 68K 0.5w, 10%

R53 1K 0.5w, 10%

R54 68K 0.5w, 10%

R55 1K 0.5w, 10%

R56 680 0.5w, 10%

R57 1.2K 0.5w, 10%

R58 22K 0.5w, 10%

R59 47K 0.5w, 10%

R60 4.7K 0.5w, 10%

R61 270-430 RH8-5w

R62 27K, 2w

R63 470 0.5w, 10%

R64 4.5M 0.5w, 10%

R65 4.5M 0.5w, 10%

R66 2M 0.5w, 10%

R67 2M 0.5w, 10%

R68 2M 0.5w, 10%

R69 2M 0.5w, 10%

R70 1200 5w

R71 89PR 5K, variable

R72 2.7K 0.5w, 10%

R73 42, 25w

R74 91T 20K, variable

TABLE A3 CONT.

R75 91T 20K, variable	R86 100 0.5w, 10%
R76 1K 0.5w, 10%	R87 1K 0.5w, 10%
R77 4.5M 3w	R88 100 0.5w, 10%
R78 89PR-25K, variable	R89 1K 0.5w, 10%
R79 1K 0.5w, 10%	R90 10 0.5w, 10%
R80 47K 0.5w, 10%	R91 100 0.5w, 10%
R81 31T-20K, variable	R92 10 0.5w, 10%
R82 91T-20K, variable	R93 1K 0.5w, 10%
R83 10K 0.5w, 10%	R94 100 0.5w, 10%
R84 5.6K 0.5w, 10%	R95 1K 0.5w, 10%
R85 10 0.5w, 10%	R96 10 0.5w, 10%

Other Components:

2 Toroidal Transformers

1 720 MHz Bandpass Filter

1 30 V, 5A Circuit Breaker

1 28 V, Tungsten Panel Lamp

A1.3 THE RECEIVER

The receiver for the radio echo sounder (Fig. A1.14) includes all the circuitry required to perform two basically independent functions. One part of the receiver is the actual radio frequency receiver - a heterodyne receiver, detector and video amplifier. The second part includes all the digital circuitry required to trigger the transmitter and to control an oscilloscope, the latter providing both a display and photographic recording capability. Since these two functions are independent (and since future versions of the radio echo sounder will certainly split these functions into two units) their descriptions have been separated.

A1.3.1 THE R.F. CHAIN AND VIDEO AMPLIFIER

A1.3.1.1 PHYSICAL DECRIPTION

The RF converting and amplifying chain includes six modular components; a diode limiter, mixer, I.F. filter, logarithmic I.F. amplifier-detector and two 6 dB passive attenuating devices (PAD's). All of the components are contained in a larger module (the RF module, see Fig. A1.14) which can be removed from the receiver by removing the four retaining screws around the RF inputs.

The video amplifier is the only component of the RF-video chain which is not modular since it is used with discrete components as bias and gain controls. The video amplifier

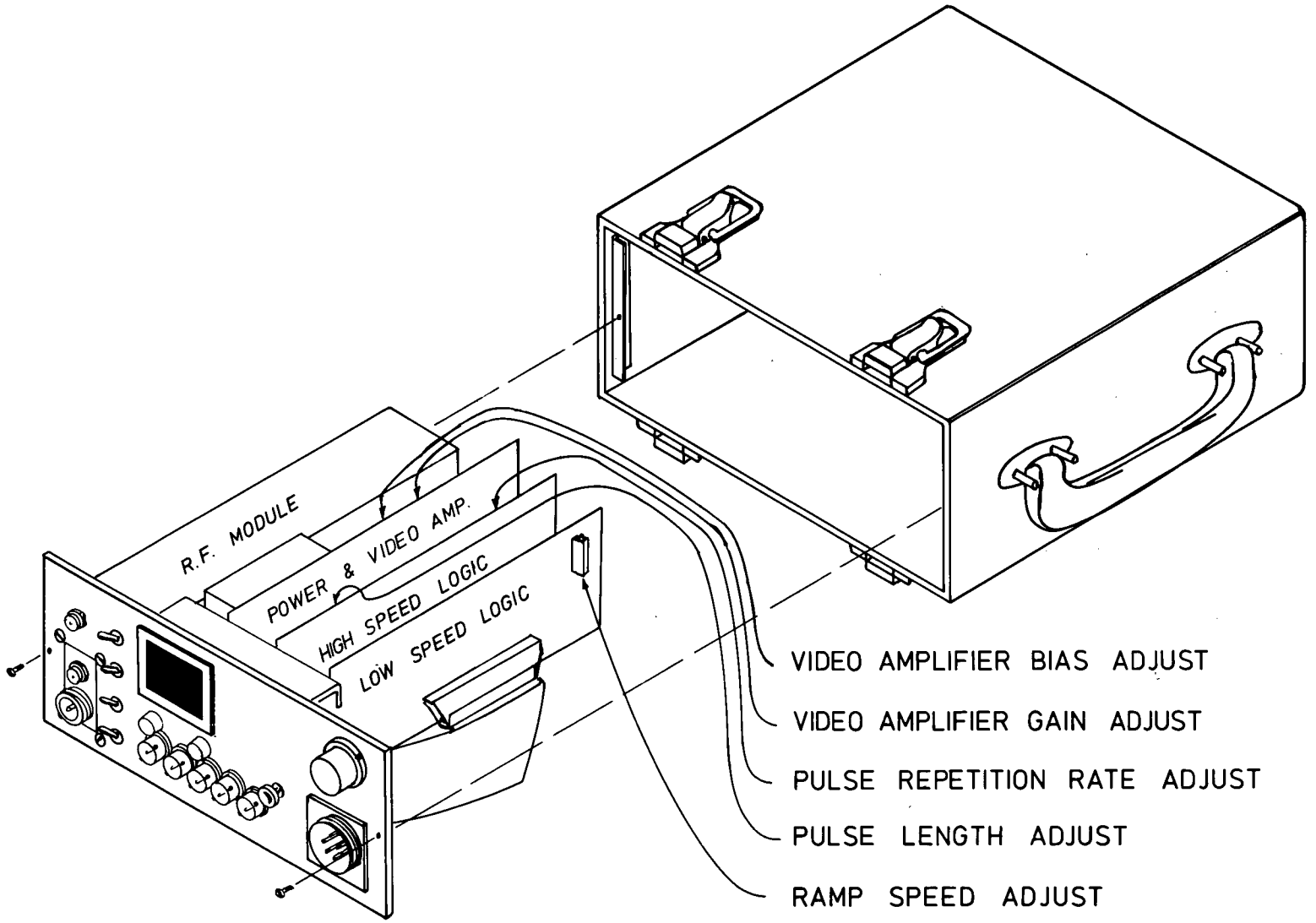

FIG. A1.14 RECEIVER PICTORIAL DIAGRAM

shares space on a printed circuit board with two DC-DC converters and three voltage regulators. One converter provides ±15 VDC for the video amplifier and +15 V for the CMOS logic circuitry. Two voltage regulators reduce these to ±12 VDC required for the log. IF amplifier-detector. The second converter and third regulator provide +5 VDC required by the high speed TTL logic circuitry used to drive the transmitter trigger and by the front panel displays.

A1.3.1.2 CIRCUIT DESCRIPTION

R.F. CIRCUITRY

This description traces the signal starting from the RF input. Refer to figure A1.15. The RF input is protected against overload by a solid state diode limiter (DL1). The limiter allows any signal up to 50 mW to pass through it effectively unattenuated. Any power applied to the limiter in excess of 50 mW is absorbed by the limiter. Saturation of the limiter normally occurs each time as RF transmission occurs either because of a direct wave between two antennae or because of power reflected in the antenna feed back through the circulator. The diode limiter is capable of withstanding overloads in excess of 4 KW in the event of a circulator failure or a cable failure while operating with a single antenna. Less than 0.1 erg of high level energy will pass through the limiter before it achieves a saturated state. The diode limiter

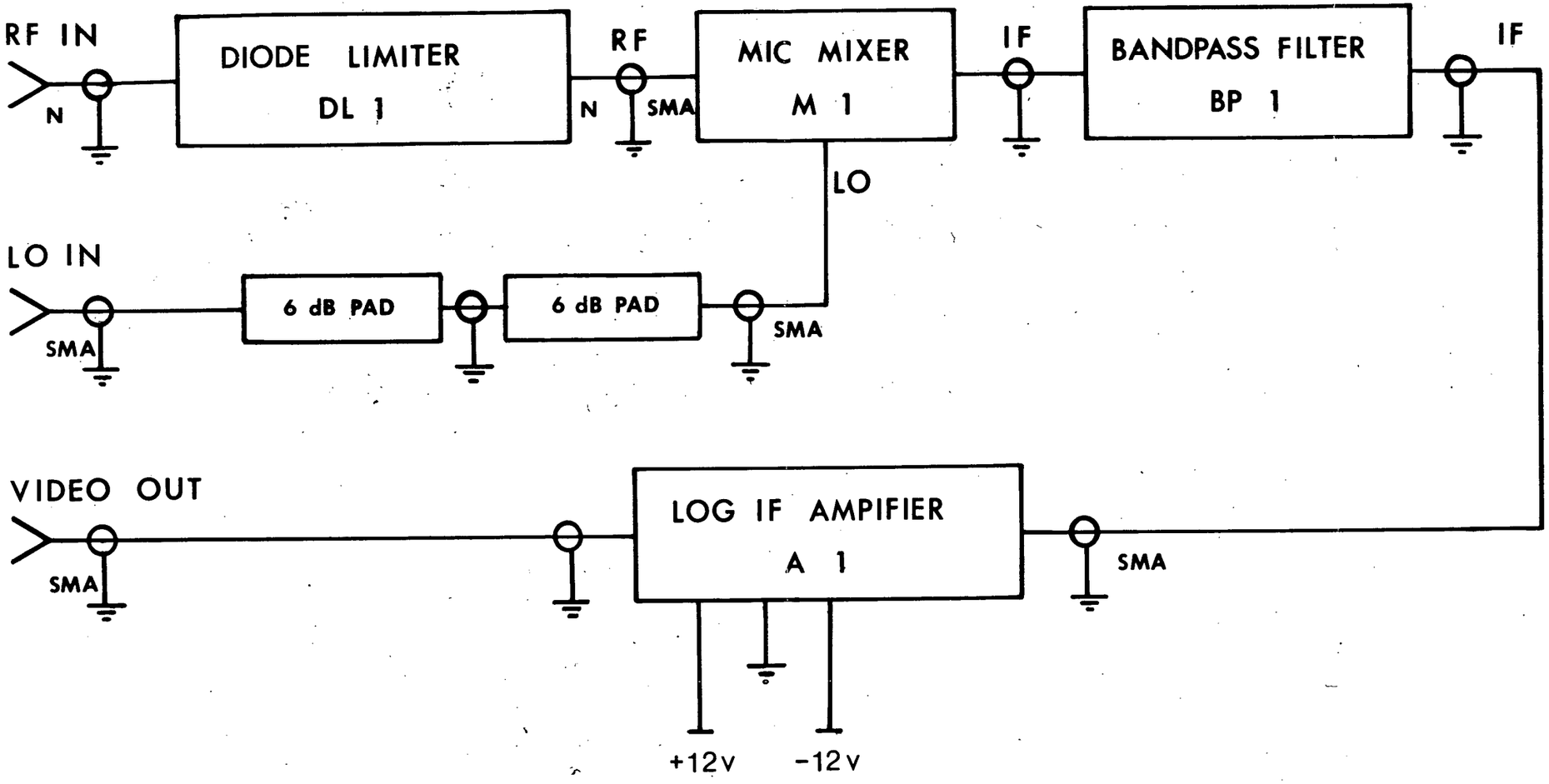

RF MODULE : CONNECTION DIAGRAM

FIG. A1.15

requires 100ns to recover from saturation.

From the diode limiter the RF signal passes to a double-balanced miniature integrated circuit mixer (M1) which converts the signal to the 120 MHz intermediate frequency (I.F.). Power for the conversion is provided by the transmitter via the front panel local oscillator (L.O.) connector. The L.O. input power level from the transmitter is 160 mW (+22 dBm). 12 dB of attenuation reduces the level to 10 mW (+10 dBm), the level required at the mixer L.O. input. The conversion loss in the mixer is approximately 9.3 dB at low RF levels. The 1 dB compression level is approximately +8 dBm of RF input power. Since 50 mW (+17 dBm) is the maximum output power of the diode limiter the maximum I.F. power level attainable is limited by both the L.O. power level and the diode limiter to about 4 mW (+6 dBm). At this level the distortion product power level is a significant fraction of the fundamental I.F. power level.

The I.F. signal passes through a passive filter to the I.F. amplifier. The filter eliminates any video feedthrough from the diode limiter as well as removing conversion products and overtones coming from the mixer. The 3 dB pass band of the filter is 99 MHz to 141 MHz. The full filter characteristic is reproduced in Figure A1.16.

The I.F. amplifier is the central component of the receiver. Specifically designed by RHG Electronics Lab. Inc. for airborne radar systems it was fabricated using thin film solid state hybrid technology. Its key feature is its logarithmic compression characteristic with a useful dynamic range from -70 dBm to +10 dBm (Fig. A1.17). The amplifier

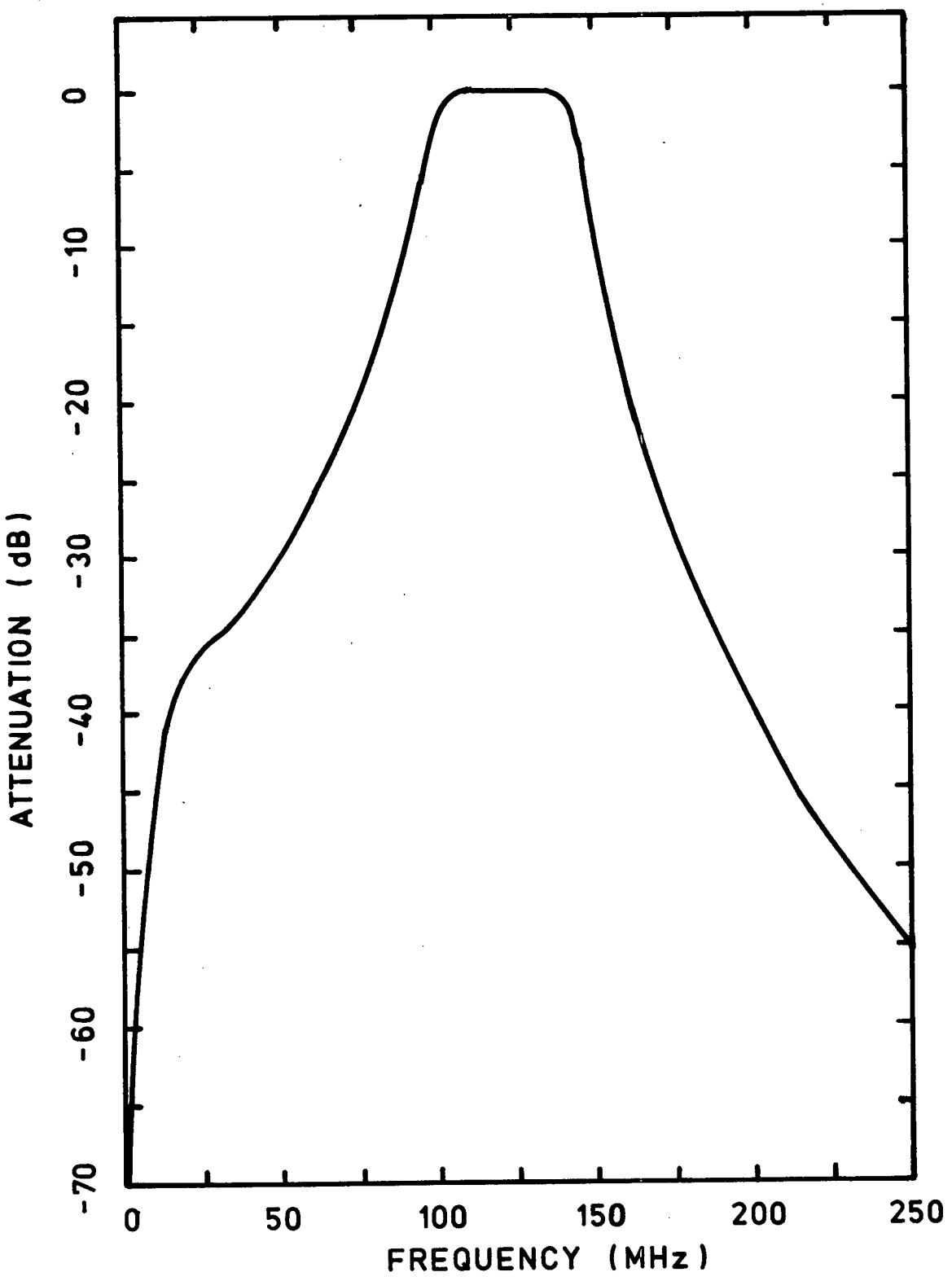

FIG. A1.16 I.F. FILTER BANDPASS CHARACTER

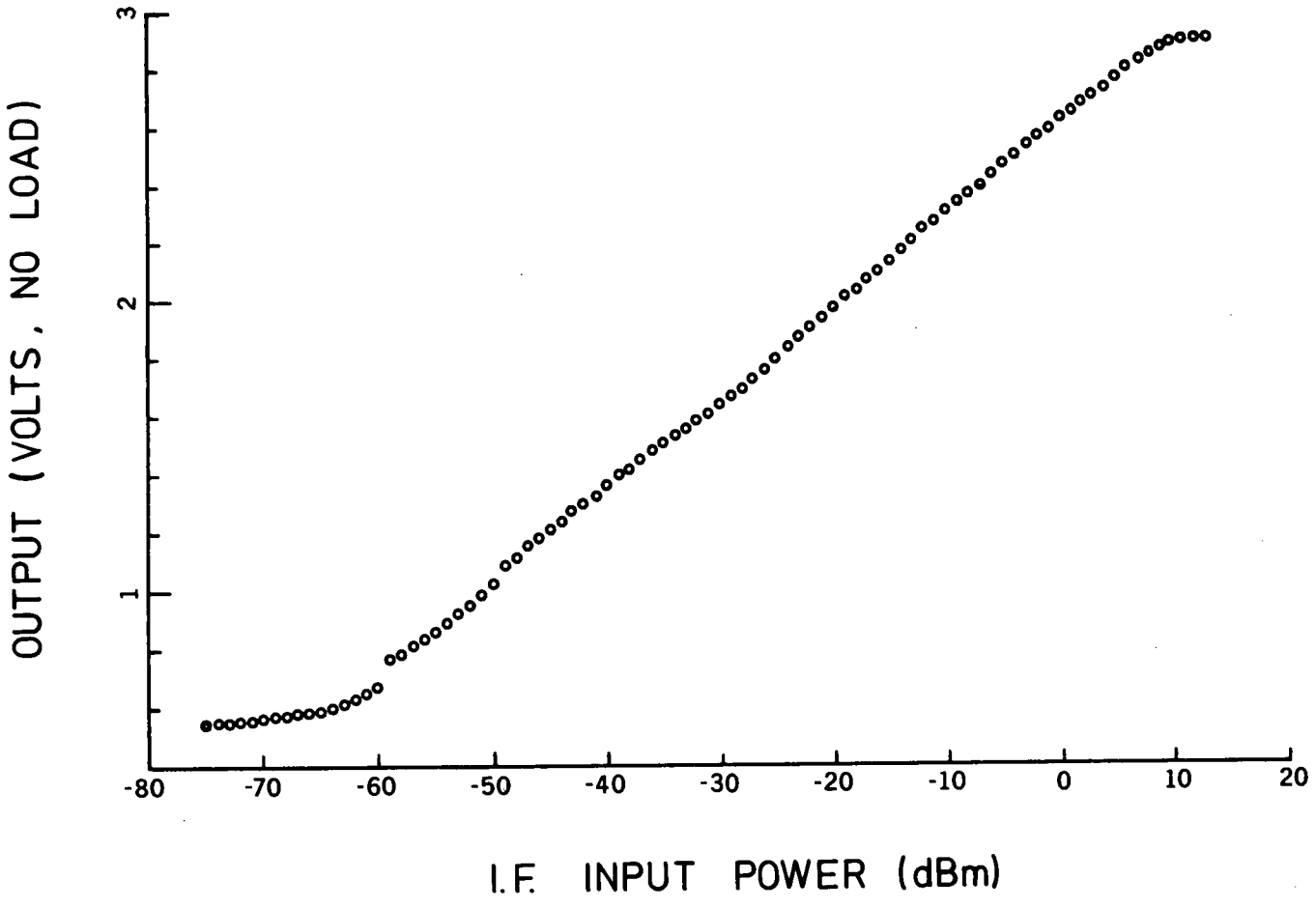

FIG. A1.17 CONTINUOUS WAVE CHARACTERISTIC OF LOG. I.F. AMPLIFIER AT 120 MHz

provides a detected output signal. This signal, the basic video signal, varies from 0.56 V at an I.F. level of -70 dBm (100 pW) to 2.84 V at +10 dBm. The logarithmic accuracy is within ±1 dB over more than 70 dB of dynamic range. The amplifier 3 dB bandwidth is 40.1 MHz at a centre frequency of 120 MHz. The amplifier output risetime is less than 20 ns. The I.F. amplifier is the only component in the RF module requiring DC power. It uses +12 VDC at 60 mA and -12 VDC at 130 mA. Both voltages are generated on the power supply - video amplifier board and are provided to the I.F. amplifier via jumpers to the RF module.

The basic video signal is led by coaxial jumpers to both a front panel connector (V) and to the video amplifier input. The video amplifier (Fig. A1.18) is needed to condition the video signal for modulation of an oscilloscope phosphor intensity, making the image suitable for continuous photographic recording. The prime requirement of the amplifier is a large bandwidth. The operational amplifier used here (Burr Brown 3400A), a monolithic hybrid amplifier, excels at this task having a full power bandwidth of 30 MHz and an output slew rate of 1000 V us^{-1}. The amplifier is configured as an inverting amplifier (required by the Tektronix 475 Z input). R48 is the bias adjustment (Figure C5) and R49 is the gain adjustment of the amplifier. Power for the amplifier is drawn from the 24 VDC to ±15 VDC converter which is on the same board as the amplifier.

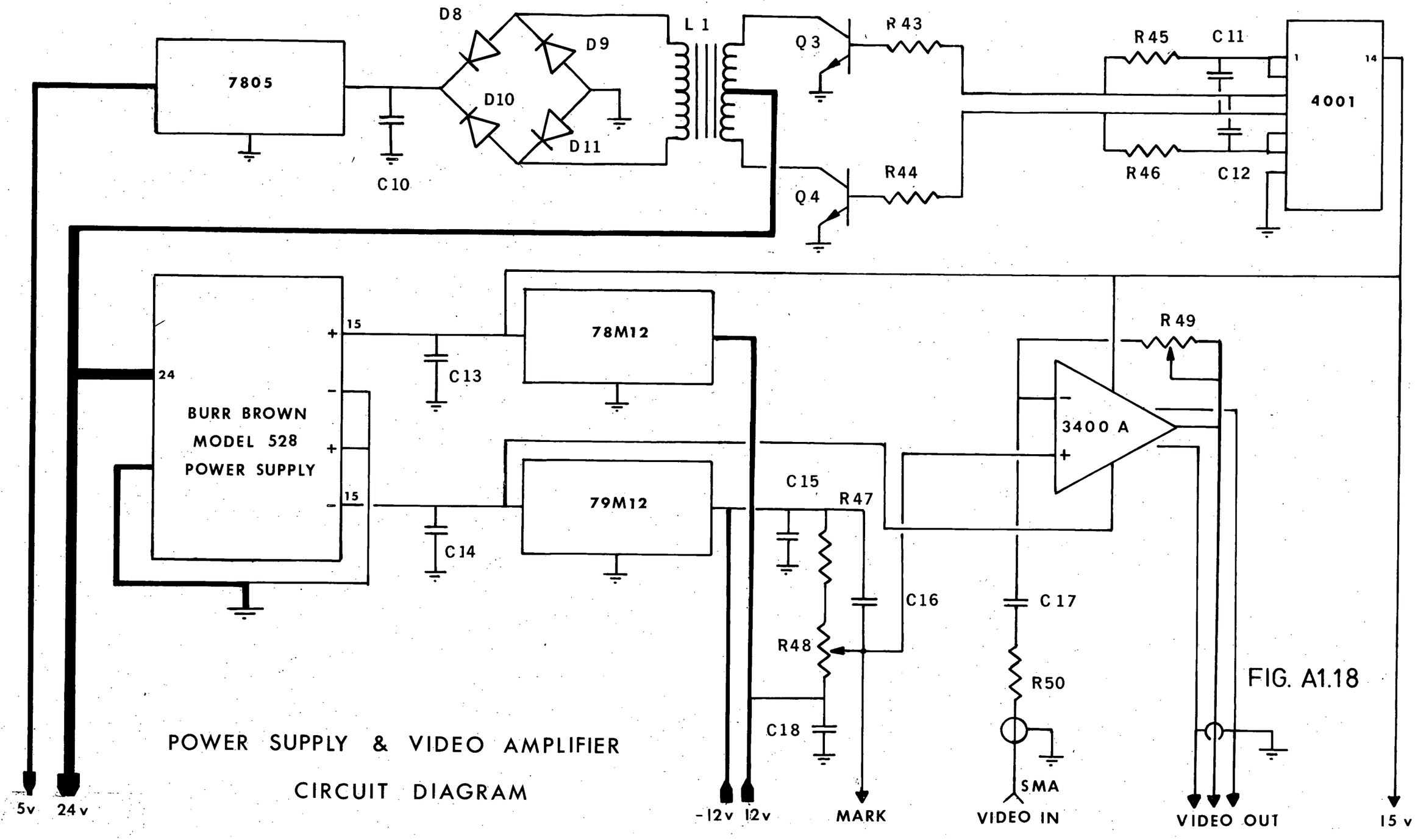

POWER SUPPLY & VIDEO AMPLIFIER

CIRCUIT DIAGRAM

FIG. A1.18

POWER SUPPLY

The receiver power supply provides five DC voltages, ±15 V, ±12 V and +5 V. A Burr-Brown model 528 DC-DC converter provides the ±15VDC from the 24 V to 28 V input, with 200mA maximum output before current limiting goes into effect. The ±12 V supplies are derived from the ±15 V supplies by two three pin regulators, a 78M12 for the +12 V supply and a 79M12 for the -12 V supply.

The +5 V supply uses a separate discrete-component DC-DC converter, with a maximum output of 1 A. An astable oscillator constructed from two NOR gates, two capacitors (C11 and C12) and two resistors (R45 and R46) provides a 400 Hz biphase clock to alternately switch on and off transistors Q3 and Q4. This switching results in a pure AC square wave on the primary of transformer L1. The output square wave is rectified in a full wave bridge and filtered by capacitor C10. At this point the DC voltage may vary from +7 V to +9 V dependng on the input power level. A three pin regulator (7805, TO-220) drops the supply level to +5 V. Current limiting goes into effect at 1 A.

A1.3.2 RECEIVER DIGITAL CIRCUITRY

The function of the digital logic circuitry is to provide the control signals necessary for the setup, display and recording of the radio echo sounder signal on an intensity modulated oscilloscope phosphor. The task can be divided into two areas: the generation and synchronization of a setup

staircase (grey scale) and binary time signal (frame code) with the video signal; the slow scanning of the oscilloscope trace vertically across the screen and the selection of the grey scale, frame code or video signal. The circuitry for each area has been implemented on individual printed circuit boards. The former, called high speed logic, operates with a 1 MHz clock frequency, the latter, called low speed logic, operates with a clock frequency which is a submultiple of 68 Hz. The two boards operate asynchronously and communicate via connections to a fourty conductor flat cable buss.

HIGH SPEED LOGIC

The basic 1 MHz clock frequency is derived using two CMOS inverters and RC relaxation oscillator circuitry (R32, R33, R73, C7, C8) (Fig. A1.19), (Fig. A1.20). The frequency is adjusted by R33 (pulse repetition rate adjust). The oscillator is not temperature compensated so that the 1 MHz frequency should not be used as a timing reference.

The clock frequency is divided by 128 through seven stages of a binary ripple counter (4040) (Fig. A1.21). The grey scale and frame code are derived using output bits 1 through 4. Output bit 7 defines the transmitter pulse repetition rate. When bit 4 is high both the grey scale and the frame code are disabled. When bit 4 is low bits 1, 2 and 3 each translate through a NOR gate and an inverter to drive a three bit resistor-ladder digital to analogue converter (R34, R35, R36,

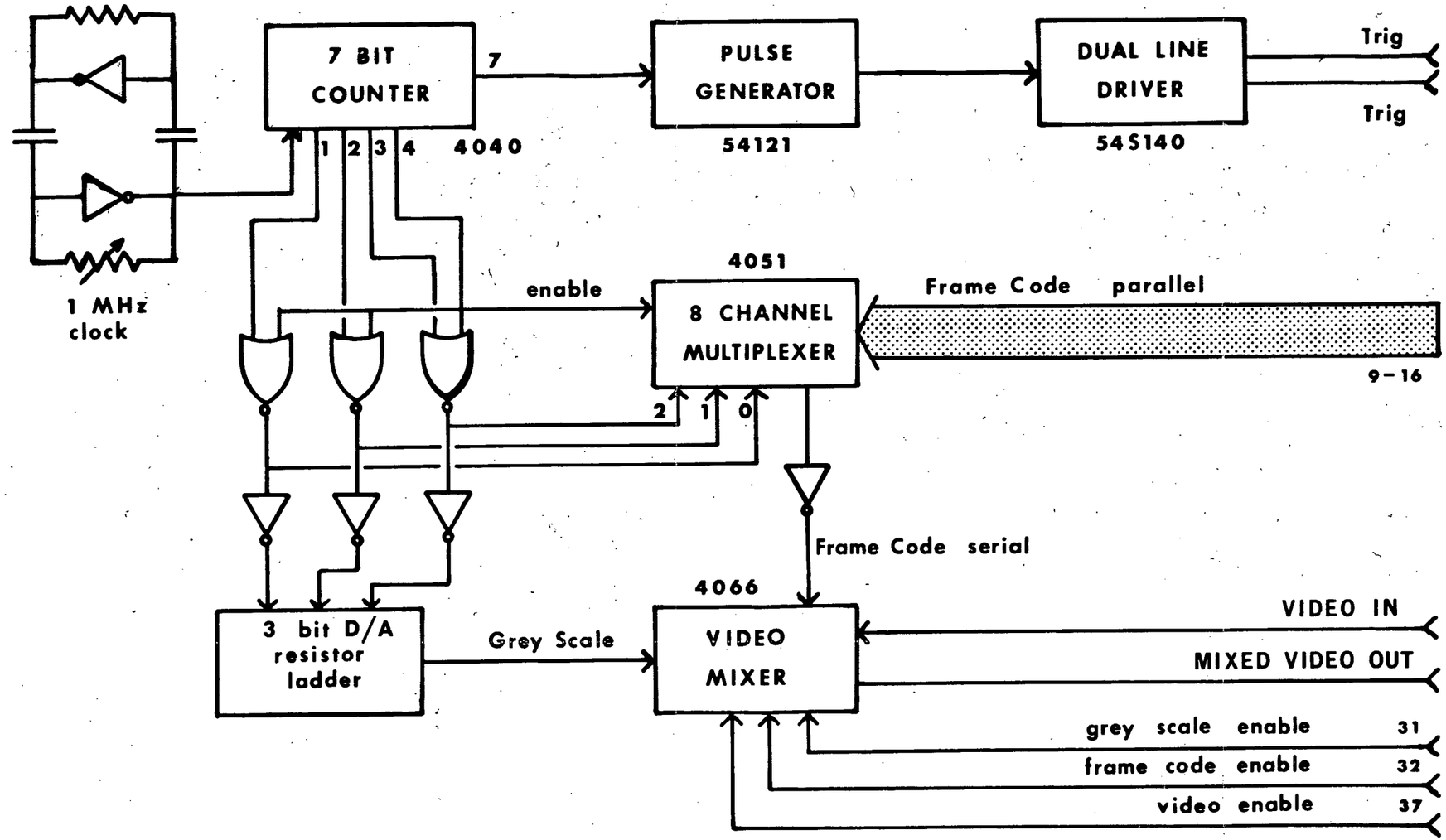

HIGH SPEED LOGIC ; LOGIC DIAGRAM

FIG. A1.19

FIG. A1.20

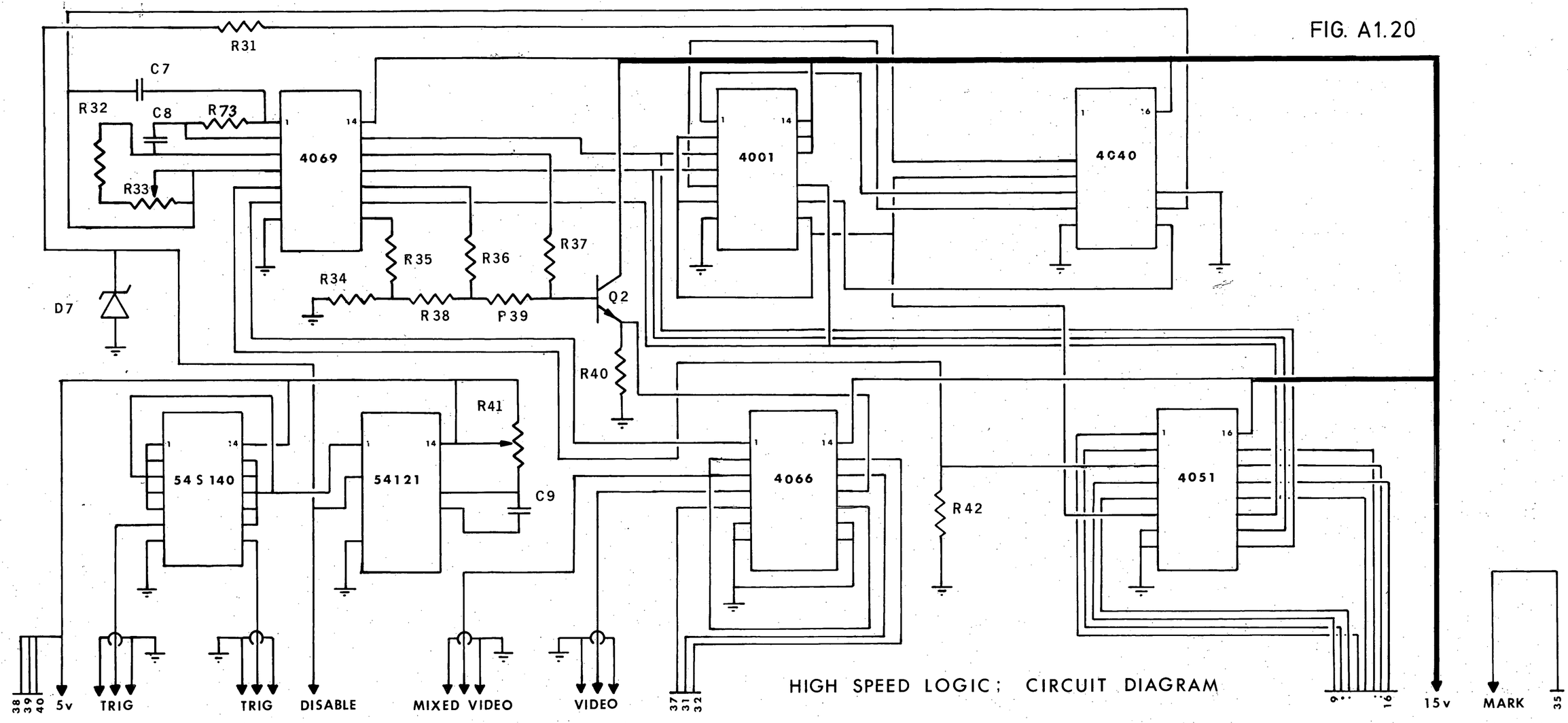

HIGH SPEED LOGIC; CIRCUIT DIAGRAM

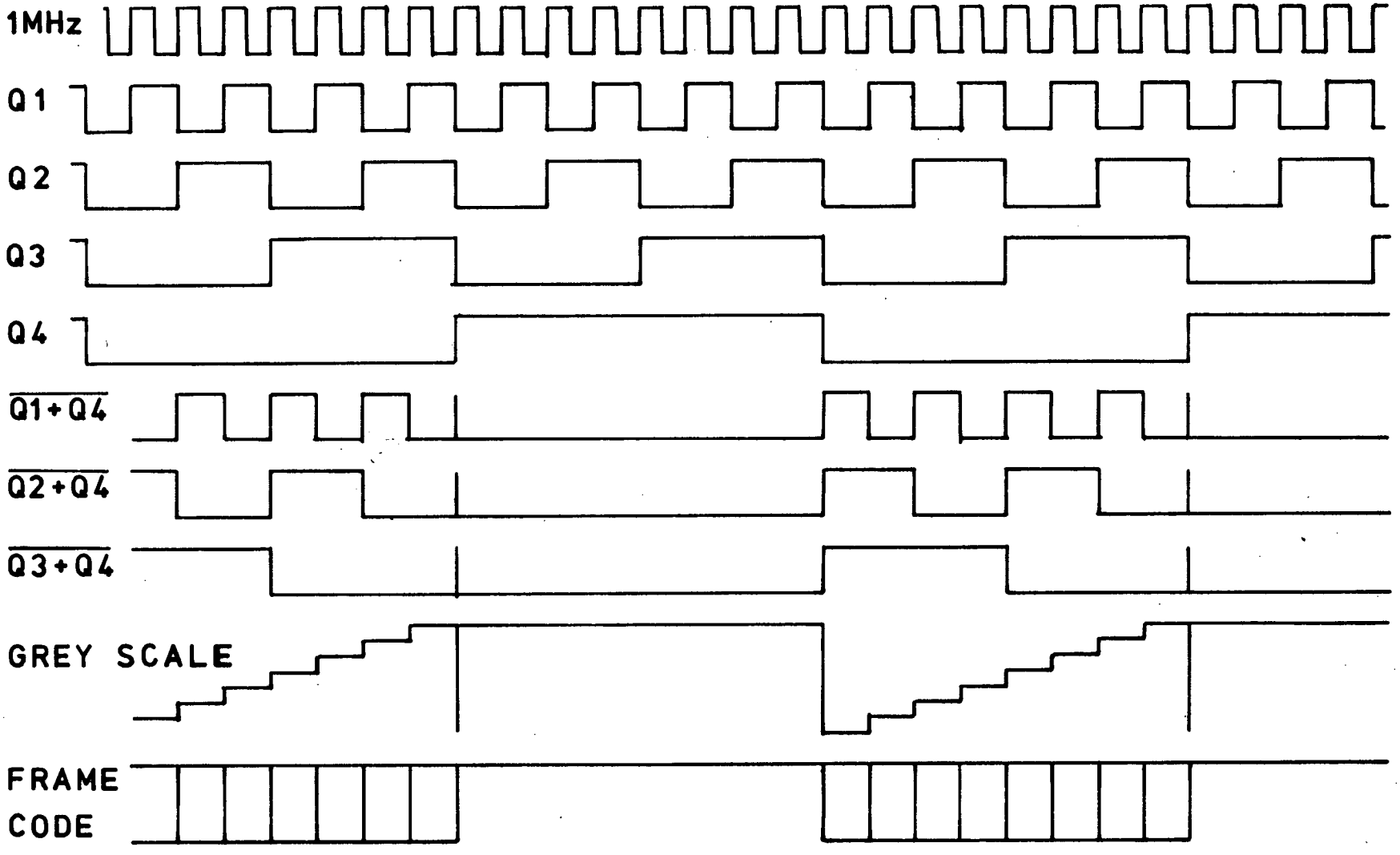

FIG. A1.21 HIGH SPEED LOGIC TIMING DIAGRAM 1

R37, R38 and R39). The output is buffered by high speed switching transistor Q2 and resistor R40. The buffered grey scale is switched as required onto the mixed video line by a bilateral analogue CMOS switch (4066). When bit 4 is high all three signals driving the D/A converter also go high resulting in the grey scale output being at its highest value. This high level signal would blank the oscilloscope phosphor.

The same three signals that drive the D/A converter, except for opposite polarity, also drive the channel select lines on an eight channel multiplexer (4051). This analogue multiplexer has been used to turn incoming information on eight flat cable lines (9-16) into the frame code. Each signal is selected in turn for one usecond by the sequence of binary numbers determined by the counter bits 1, 2 and 3. When bit 4 is high the multiplexer output is forced to a low voltage, which after being inverted will blank the oscilloscope phosphor. As with the grey scale, the multiplexed frame code is switched as required onto the mixed video line by a bilateral analogue CMOS switch (4066).

The video signal which comes from the video amplifier onto the card via the edge connector is also switched onto the mixed video line by an analogue CMOS switch. When line 37 on the flat cable buss is high the video signal passes onto the mixed video line. When lines 31 or 32 go high the grey scale or frame code respectively pass onto the mixed video line. No two of the enabling lines can go high simultaneously.

The leading edges of the grey scale and frame code, which both start on the down transition of the counter bit 4, are synchronized with the transmitter trigger pulse which is started

by an up transition on counter bit 7 (Fig. A1.22). In this way the transmitter repetition period is 128 useconds, within its duty cycle specification. The transmission pulse length is determined by the cycle time of a monostable multivibrator. The 15 V bit 7 transition is reduced to a 0-5 V transition by resistor R31 and Zener diode D7. The rising edge triggers a TTL monostable vibrator (54121) with resistor R41 and silver mica capacitor C9 determining the pulse length. The inverted output of the multivibrator drives the inputs of a dual inverting line driver (54S140). The output pulse from the line drivers are adjustable from 50 ns to 200 ns. They are each capable of driving a 50 Ω line at TTL levels. One output is dedicated as the transmitter trigger. The other is available as a trigger for any other instrument.

LOW SPEED LOGIC

The heart of the low speed logic (Fig. A1.23) is a ramp generator comprising a variable clock, ten-bit counter and a nine-bit D/A converter. The ramp output varies at a constant rate from 0 V through 15 V over one of eight binary multiples of 15 seconds. The ramp provides a means of scanning an intensity modulated oscilloscope trace vertically across the screen, continuously exposing a frame of film. At the end of each vertical scan the ramp resets to 0 V and waits for an operator-supplied restart signal.

The basic clock rate is determined by resistors R26, R28,

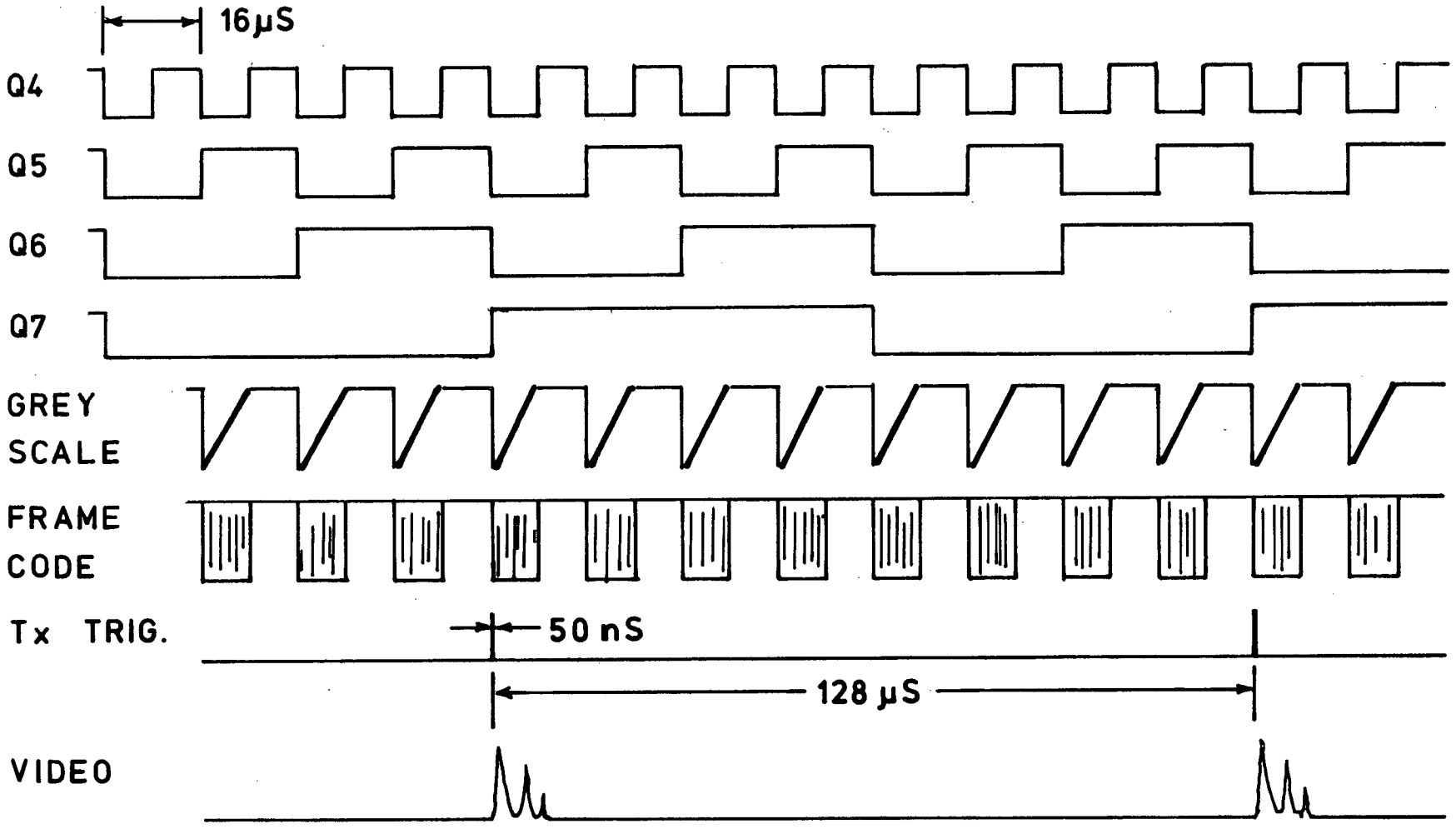

FIG. A1.22 HIGH SPEED LOGIC TIMING DIAGRAM 2

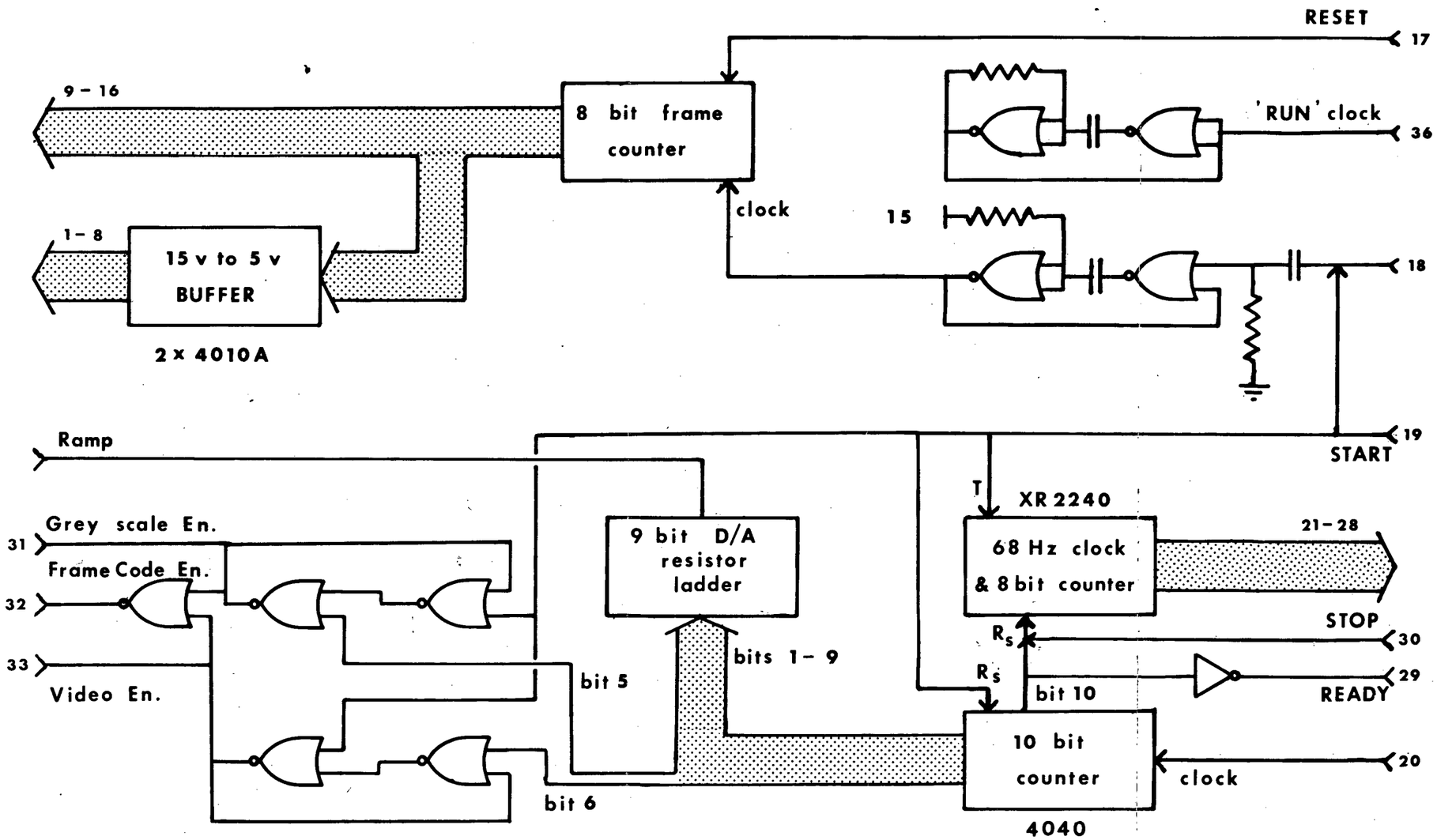

LOW SPEED LOGIC ; LOGIC DIAGRAM

FIG. A1.23

capacitor C6 and linear circuitry in the 2240 triggerable integrated timer circuit (Fig. A1.24). The 2240 timer includes an eight-bit binary counter with open collector outputs. Via flat cable buss lines 21 to 28, the front panel switch S1 selects one of these outputs to clock the ten bit counter (4040). The clock input to the counter is on the return line from S1 (flat cable line 20) along with pull-up resistor R23.

The fastest clock frequency generated by the 2240 timer is approximately 68Hz. This corresponds to a total vertical scan time of about 15 seconds. Each successive output is at exactly half the previous frequency requiring twice the total vertical scan time. The eight scan times available are 15s, 30s, 1m, 2m, 4m, 8m, 16m and 32m.

The scan cycle is as follows. A rising edge on the "start" line (flat cable line 19) passes through diode D2 and capacitor C2 to set a monostable vibrator comprising two NOR gates, capacitor C1 and resistor R1 (Fig. A1.25). In addition the "start" pulse triggers through resistor R27 the 2240 timer into counting mode, sets or resets two other bistable flip-flops and resets the scan counter (4040). The two flip-flops are each formed from two NOR gates. The flip-flop which is set has its output connected to the "grey scale enable" line (flat cable line 31). The flip-flop which is reset has its output connected to the "video enable" line (flat cable line 33). The output of the monostable vibrator is connected to the clock of an eight-bit counter which supplies the frame code information to the high speed logic multiplexer.

Just after the start pulse, then, the frame counter is

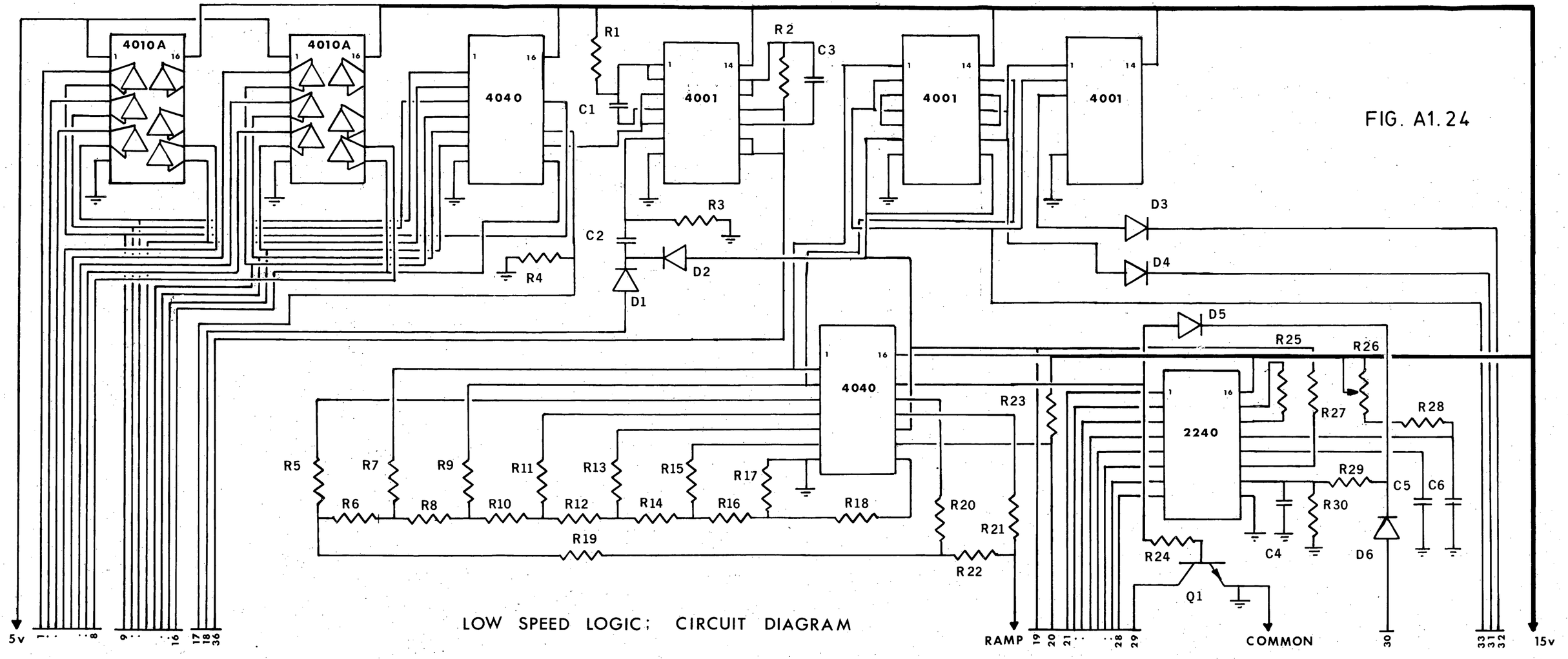

FIG. A1.24

LOW SPEED LOGIC: CIRCUIT DIAGRAM

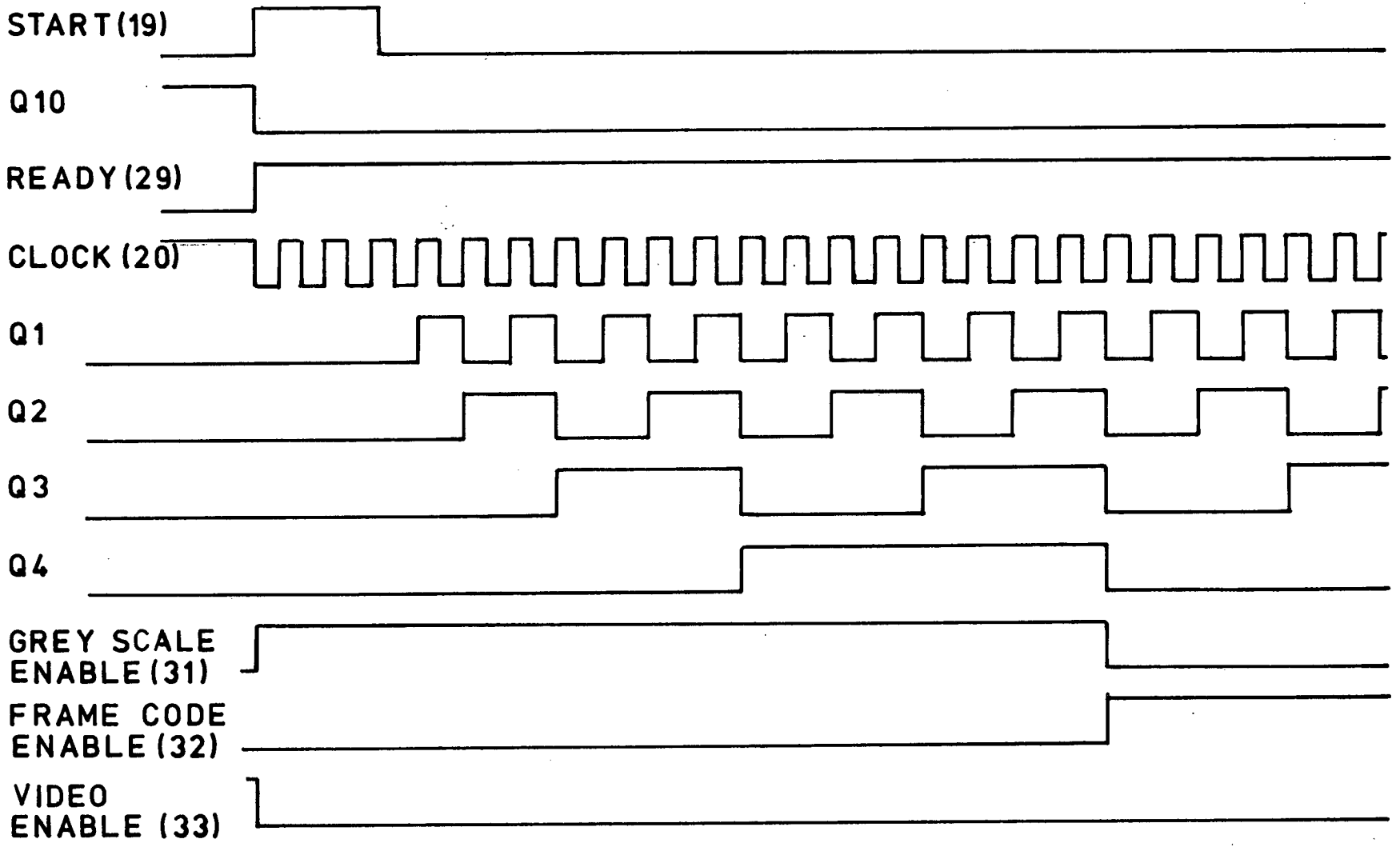

FIG. A1.25 LOW SPEED LOGIC TIMING DIAGRAM 1

incremented by one count, the grey scale is enabled and the video and frame code are disabled. The 10-bit scan counter proceeds to count up from hex'000'. The output of bit 10 is low which turns off transistor Q1 and depowers "ready" indicator lamp B2. When the scan count reaches hex'010' the high level on bit five resets the first flip-flop (Fig. A1.26). This change disables the grey scale and enables the frame code. When the scan count reaches hex'020' the high level on bit six sets the second flip-flop which enables the video and disables the frame code. When the scan count reaches hex'200' the high level on bit ten causes the 2240 timer to stop counting (via diode D5 and resistor R29), transistor Q1 to switch on and "ready" lamp B2 to glow (Fig. A1.27). The D/A resistor ladder, which uses only the low order 9 bits has returned to a 0 V output level.

The frame counter may also be incremented by the front panel switch S4 which connects flat cable lines 18 and 36. In this way a "run" oscillator can increment the counter through diode D1 independent of the rest of the low speed circuitry. The counter outputs connect directly to the high speed frame code multiplexer via flat cable lines 9 to 16. In addition, through two 4010A buffer circuits the frame count is provided at TTL levels on flat cable lines 1 to 8. (It is important to note here that the TTL levels are required for the front panel LED driver circuits. At the time that this circuit was designed no CMOS compatible BCD to seven-segment decoders were available. It is also important to note here that the presence of the 4010A circuits as used here forces the obsolescence of the presented design. The 4010A with separate VDD and VCC are no longer being

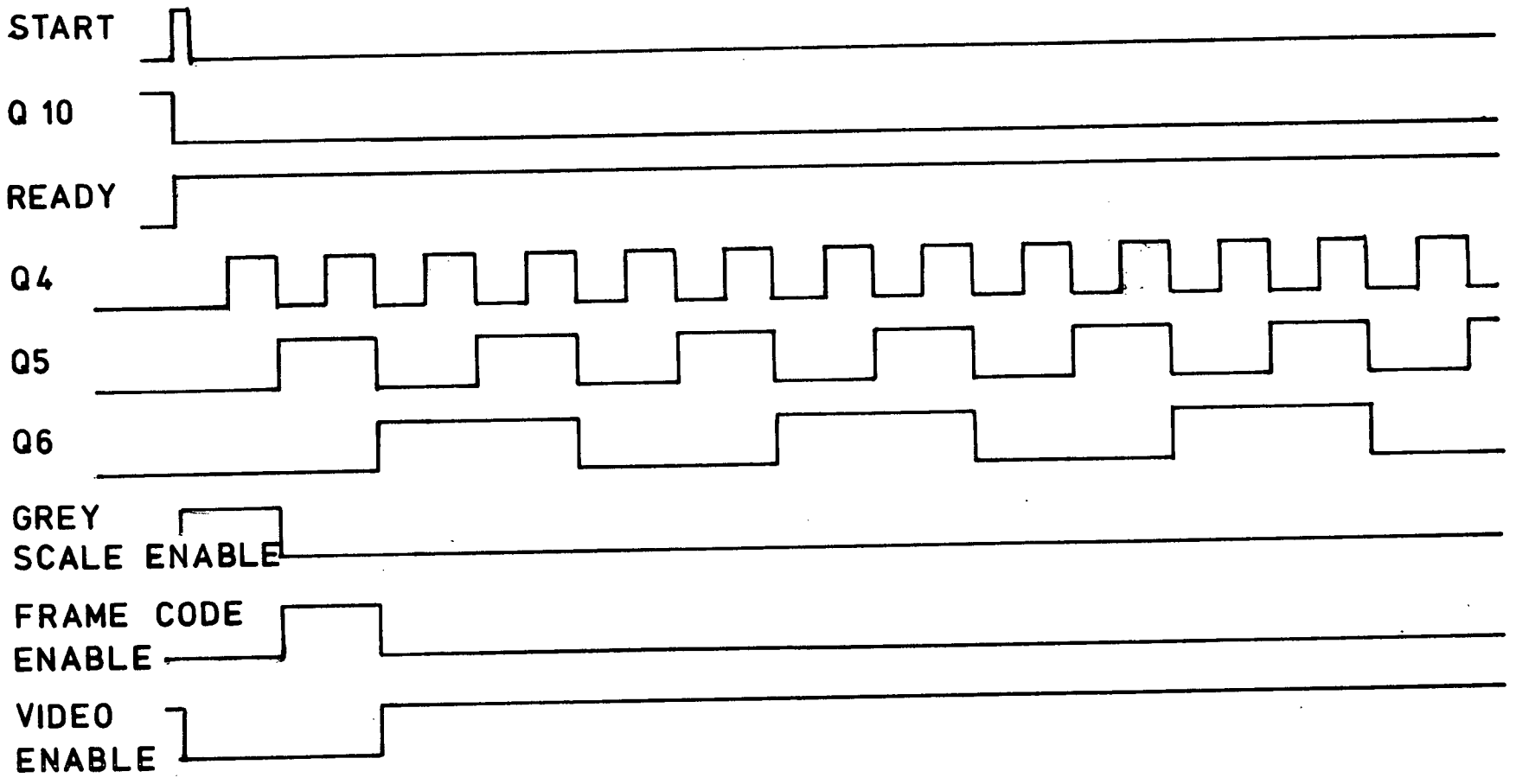

FIG. A1.26 LOW SPEED LOGIC TIMING DIAGRAM 2

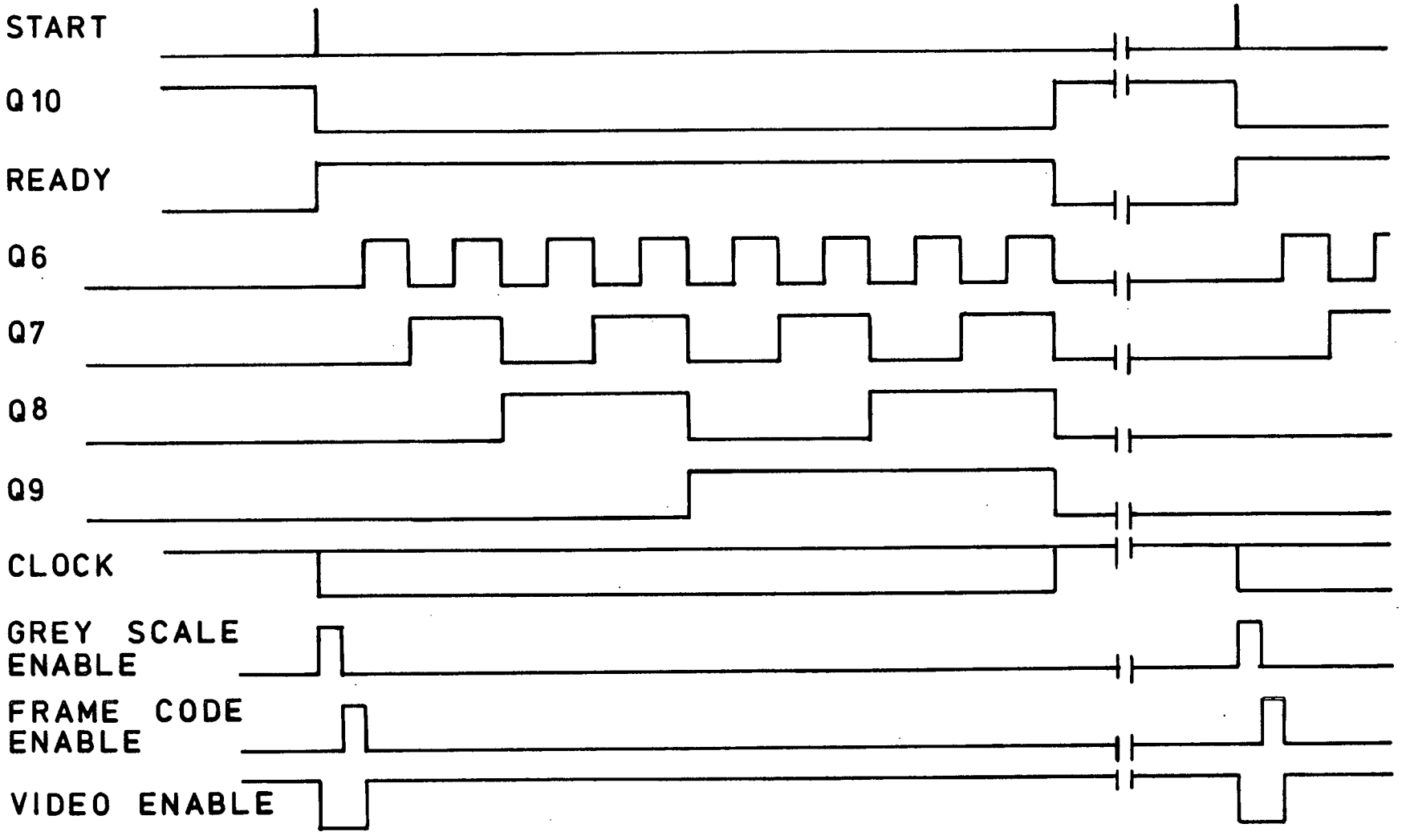

FIG. A1.27 LOW SPEED LOGIC TIMING DIAGRAM 3

made since manufacturers found that there was a tendency for the 4010A to latch when powered up in specific manners. No alternates are available.)

The TTL level frame count is decoded at the front panel into seven-segment octal by three 9317B circuits. The 9317B's drive three seven-segment LED displays (Fig. A1.28) allowing the operator to preset and monitor the frame count. The operator may also reset the frame count with S4 which connects a high level signal onto flat cable line 17.

FIG. A1.28

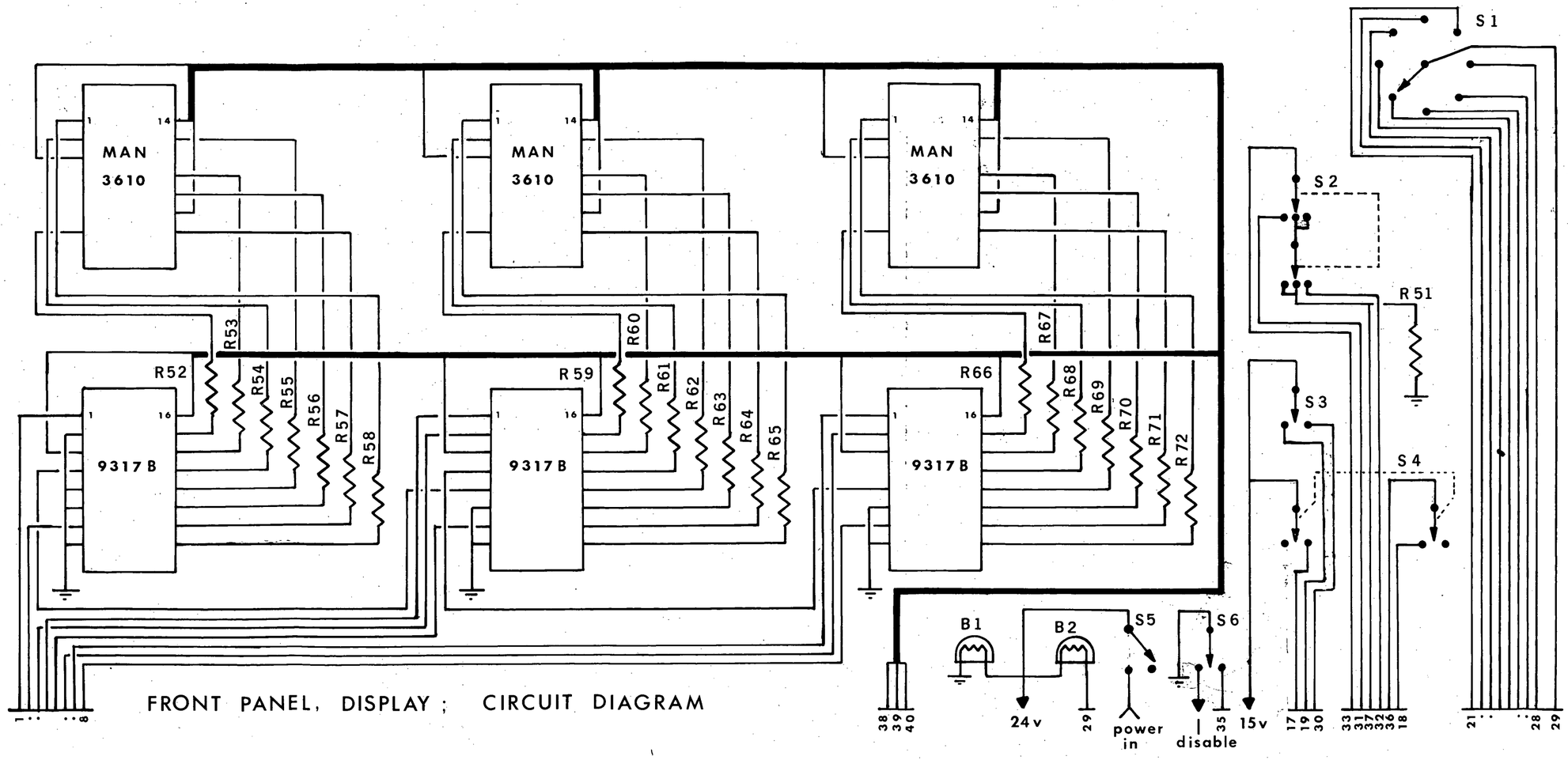

FRONT PANEL, DISPLAY ; CIRCUIT DIAGRAM

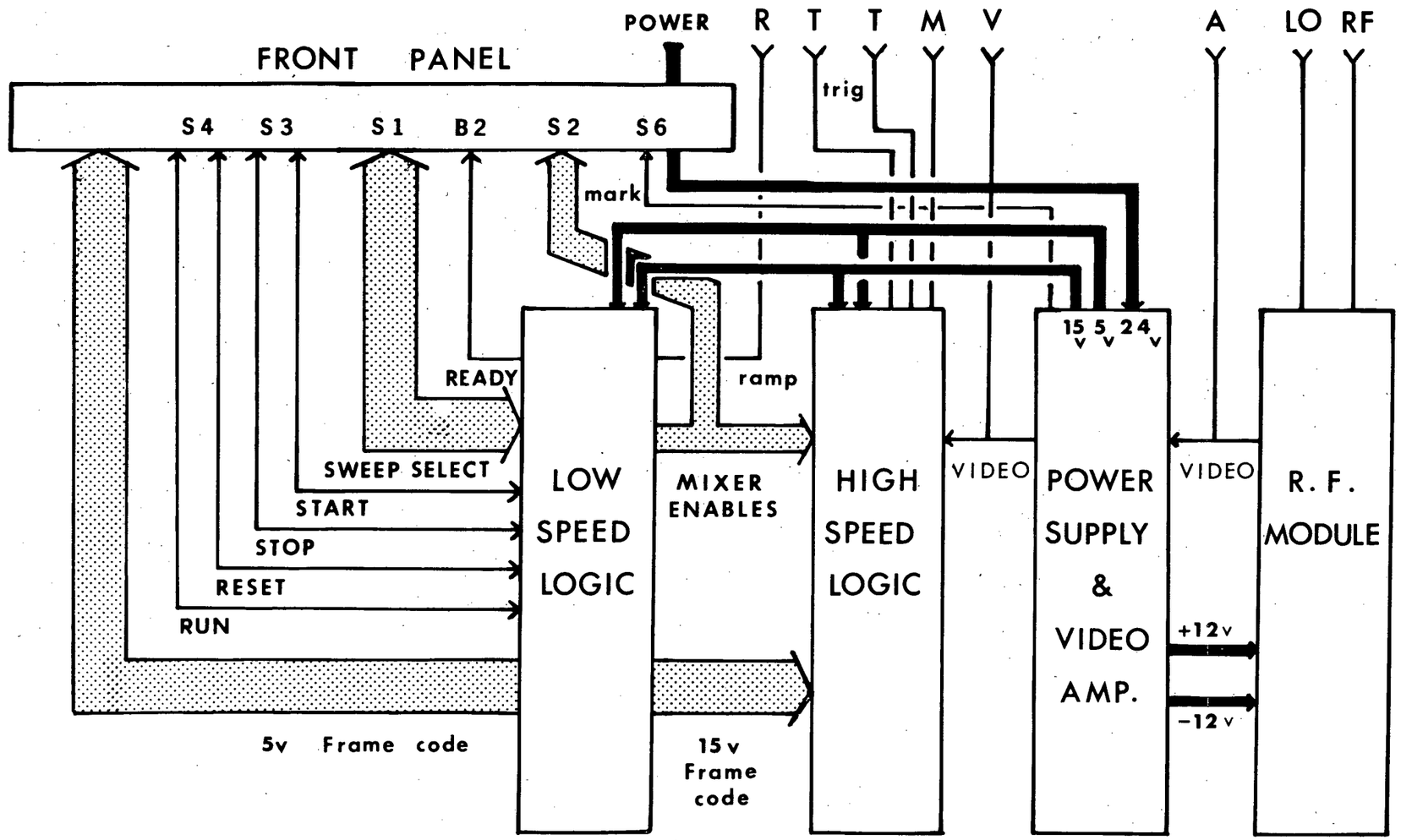

RECEIVER ; CONNECTION DIAGRAM FIG. A1.29

Table A4: Receiver R.F. Module Components

DL1 Diode Limiter MD-30T30 #001

Micro-Dynamics Inc.

Flat leakage 50 mW max. Spike leakage 0.1 erg max.

Recovery time 100 ns max.

Insertion loss 0.5 dB max.

M1 Double Balanced Mixer MA-1

Mini-Circuits Laboratory

Insertion loss 9.0 - 10.0 dB

LO level +10 dB

BP1 Bandpass Filter 3B120-120/40-op/o #5267-1

K & L Microwave Inc.

Pass band 99 MHz to 141 MHz

Insertion loss 0.4 dB

A1 Logarithmic IF Amplifier ICLT12040 #7-511-1

RHG Electronics Laboratory Inc.

Dynamic range -70 dBm to +10 dBm

Pass band 99 MHz to 140 MHz

Rise time 20ns max.

Log. linearity ±1 dB over 70 dB

Output range +0.4 V to +2.8 V

Power required ±12 V @ 130 mA max.

Table A5: Receiver Components: Required Integrated Circuits

7805	+5 VDC Voltage regulator
78M12	+12 VDC Voltage regulator
79M12	-12 VDC Voltage regulator
3400A	Operational amplifier, Burr Brown
4001	CMOS quad NOR gate (x5)
4040	CMOS 12 bit counter (x3)
4010A	level shifting hex buffer (obsolete) (x2)
4051	CMOS analogue multiplexer
4066	CMOS quad bilateral analogue switch
4069	CMOS hex inverter
2240	NMOS timer-counter
54121	TTL monostable vibrator
54S140	TTL dual 5-input NAND line driver
9317B	TTL seven segment from BCD decoder-driver (x3)
MAN3610	LED seven segment display, 0.300", Monsanto (x3)

Required Power Module

Model 528, 28 V to ±15 V DC-DC converter, Burr Brown.

Table A6: Receiver Discrete Components Parts List

Q1 2N4238
Q2 2N3014
Q3 2N4238
Q4 2N4238
C1 17 ufd, 16 V
C2 17 ufd, 16 V
C3 3.3 ufd
C4 1000 pfd
C5 3.3 ufd
C6 3.3 ufd
C7 470 pfd
C8 470 pfd
C9 90 pf silver mica
C10 47 ufd, 16 V
C11 1000 pfd
C12 1000 pfd
C13 22 ufd, 35 V
C14 22 ufd
C15 41 ufd, 16 V
C16 15 ufd, 35 V
C17 1 ufd, 250 V
C18 22 ufd, 16 V

D1 1N914
D2 1N914
D3 1N914
D4 1N914
D5 1N914
D6 1N914
D7 5 V Zener, 1w, DO-7
D8 1A silicon rectifier
D9 1A silicon rectifier
D10 1A silicon rectifier
D11 1A silicon rectifier
R1 27K 0.25w, 5%
R2 27K 0.25w, 5%
R3 33K 0.25w, 5%
R4 100K 0.25w, 5%
R5 100K 0.25w, 0.4%
R6 50K 0.25w, 0.4%
R7 100K 0.25w, 0.8%
R8 50K 0.25w, 0.8%
R9 100K 0.25w, 1%
R10 50K 0.25w, 1%
R11 100K 0.25w, 1%

TABLE A6, CONT.

R12 50K 0.25w, 1%

R13 100K 0.25w, 5%

R14 50K 0.25w, 5%

R15 100K 0.25w, 5%

R16 50K 0.25w, 5%

R17 100K 0.25w, 5%

R18 100K 0.25w, 5%

R19 50K 0.25w, 0.2%

R20 100K 0.25w, 0.2%

R21 100K 0.25w, 0.1%

R22 50K 0.25w, 0.1%

R23 10K 0.25w, 5%

R24 1K 0.25w, 5%

R25 18K 0.25w, 5%

R26 10K ten turn

R27 47K 0.25w, 5%

R28 3900 0.25w, 5%

R29 47K 0.25w, 5%

R30 1M 0.25w, 5%

R31 270 0.25w, 5%

R32 1800 0.25w, 5% (x2)

R33 1K ten turn

R34 10K 0.25w, 5%

R35 10K 0.25w, 5%

R36 10K 0.25w, 5%

R37 10K 0.25w, 5%

R38 4700 0.25w, 5%

R39 4700 0.25w, 5%

R40 470 0.25w, 5%

R41 2K ten turn

R42 4700 0.25w, 5%

R43 5600 0.25w, 20%

R44 5600 0.25w, 20%

R45 220K 0.25w, 5%

R46 220k 0.25w, 5%

R47 0.25w, 5%

R48 10K ten turn

R49 10K ten turn

R50 12K 0.25w, 5%

R51 1K 0.25w, 5%

R52 180 0.25w, 5%

R53 180 0.25w, 5%

R54 180 0.25w, 5%

R55 180 0.25w, 5%

R56 180 0.25w, 5%

R57 180 0.25w, 5%

R58 180 0.25w, 5%

R59 180 0.25w, 5%

TABLE A6, CONT.

R60 180 0.25w, 5%

R61 180 0.25w, 5%

R62 180 0.25w, 5%

R63 180 0.25w, 5%

R64 180 0.25w, 5%

R65 180 0.25w, 5%

R66 180 0.25w, 5%

R67 180 0.25w, 5%

R68 180 0.25w, 5%

R69 180 0.25w, 5%

R70 180 0.25w, 5%

R71 180 0.25w, 5%

R72 180 0.25w, 5%

L1 106S, Hammond

S1 8 position rotary, Grayhill

S2 MTA-206SA, Alco

S3 MTA-206S, Alco

S4 MTA-206S, Alco

S5 push-on, push-off, SPST, Grayhill

S6 MTA-206TA, Alco

B1 28 V tungsten panel lamp

B2 28 V tungsten panel lamp

A1.4 THE SWITCHING REGULATOR POWER SUPPLY

The following descriptions are excerpted in part from the ARRL Radio Amateur's Handbook (1975), and from Delco Electronics Application Note #49, (1971).

Switching regulators are used when it is necessary or desired to minimize power losses which would otherwise occur in the series pass transistor with large variations in input or output voltages. The basic operation of the switching regulator, known as the flyback type, may be understood by referring to Figure A1.30a. Assume that the switch is closed and that the circuit has been in operation long enough to stabilize. The voltage across the load RL, is zero, and the current through L is limited only by RI, the internal resistance of the inductor. At the instant that the switch is opened, the voltage across the load goes to a value higher than the source voltage, E, because of a series-aiding or "flyback" effect of the inductor. When the magnetic lines of flux about the inductor collapse completely, the voltage across RL will be equal to that of the source (minus the small voltage drop across RI). Each time the switch is closed and then opened, the process is repeated. By opening and closing the switch rapidly, voltage pulses may be applied across RL which are higher than the DC input voltage. A capacitor may be connected across RL to produce a DC output voltage. To keep the capacitor from discharging when the switch is closed, a diode can be connected in series with the load and its parallel-connected capacitor.

In a practical switching-regulator circuit the switching is

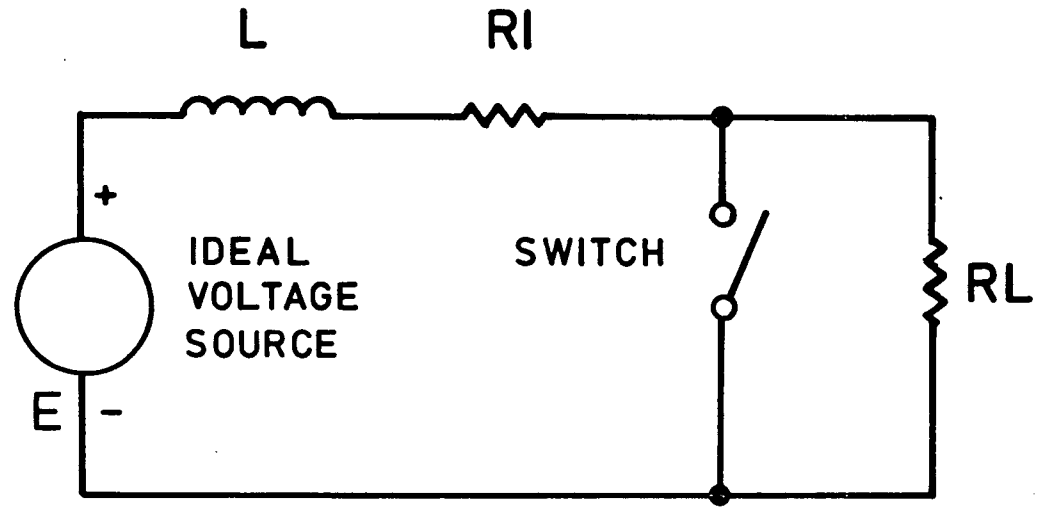

(A)

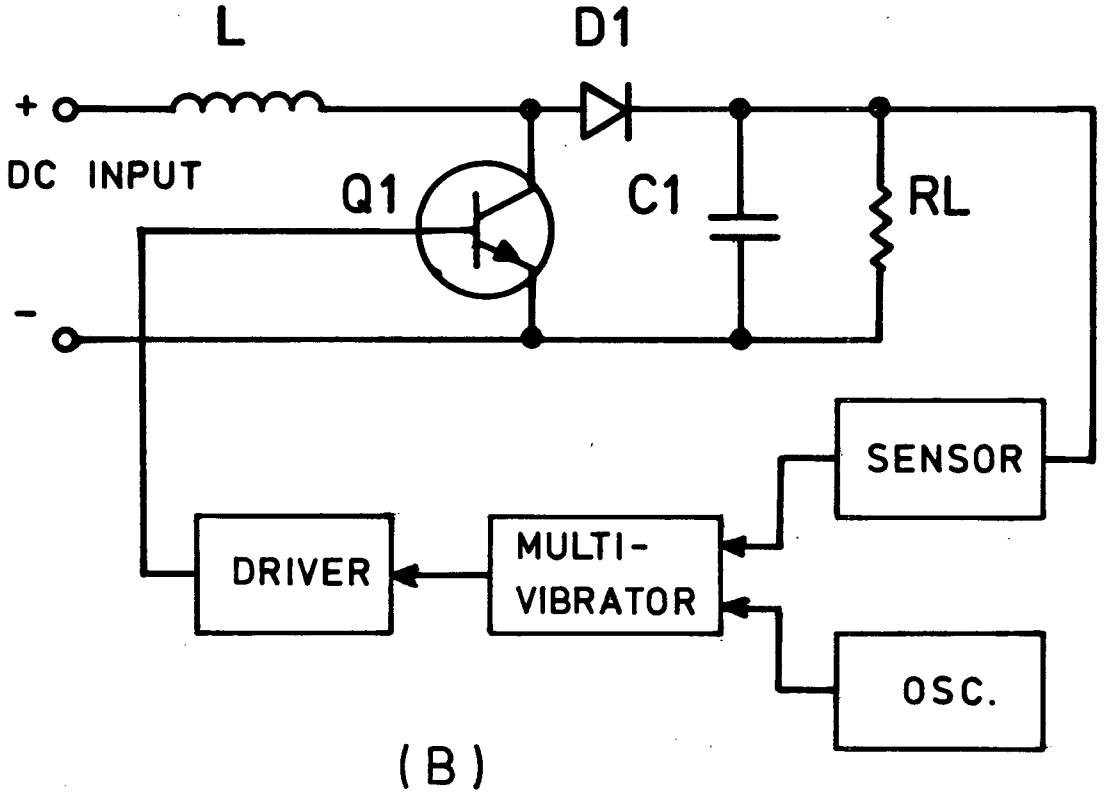

(B)

FIG. A1.30 SWITCHING REGULATOR BLOCK DIAGRAM

performed by a transistor, as shown in Figure A1.30b. The transistor may be driven by any number of circuits. In the circuit used (Fig. A1.31) four sections make up the driving circuit, as shown in the block diagram form in figure A1.30b. The oscillator triggers the monostable multivibrator and determines the frequency of operation. The sensor measures the output voltage and controls the pulse width of the multivibrator accordingly. The monostable multivibrator combines the signals from the oscillator and sensor to produce the correct pulse width. The driver receives the multivibrator output and drives the power transistor Q1.

A1.4.1 PRACTICAL CONSIDERATIONS

The voltage step-up capability of the inductor has been discussed briefly. However, in choosing the value of the inductor, energy is an important consideration. During the time the transistor is turned on, the inductor stores energy. This energy is added to the supply and delivered to the load when the transistor is turned off. The total energy must be enough to supply the load and maintain output voltage. As the load is increased, the transistor must remain on longer in order to store more energy in the inductor.

The required value of inductance depends on frequency of operation, duty cycle, and load. A linear change in current through the inductor is a desirable condition and indicates operation is over a small segment of the inductor's charging and discharging curve. The powdered iron core used for the inductor has a low mu, and therefore a large inductance change is

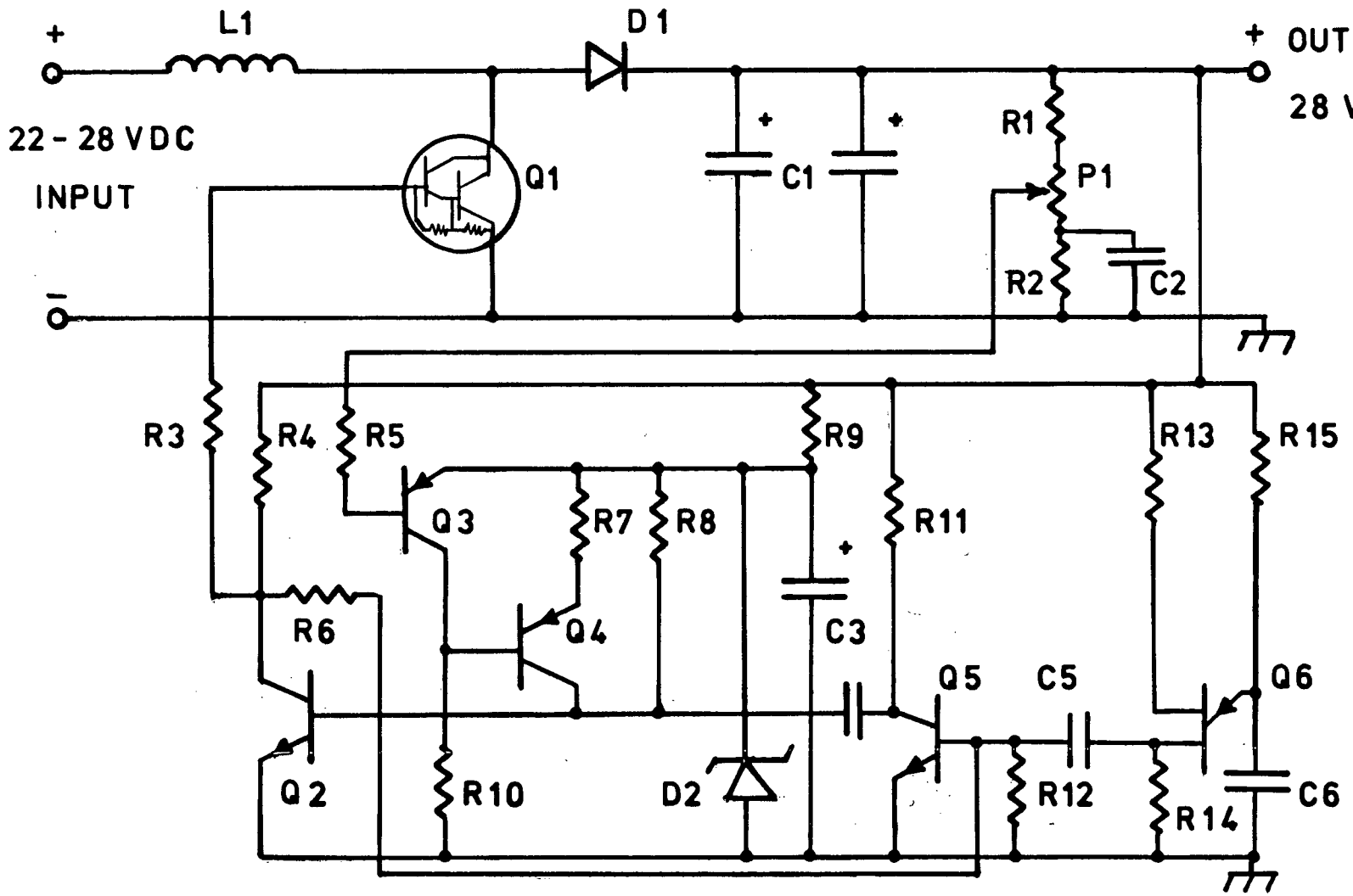

FIG. A1.31 SWITCHING REGULATOR CIRCUIT DIAGRAM

unlikely with increased current.

Efficiency of the circuit depends mainly upon the switching and saturation losses of the power transistor. The peak current through the transistor is considerably greater than the input current. The flyback diode (D1) must have a fast reverse recovery time and low forward drop. There will be a large current spike through the transistor if the diode is slow. The diode used in the circuit has a forward drop of 1.4 V max., but is used because of its trr of 0.1 us.

Output voltage variations resulting from changes in ambient temperature are caused by two major factors: positive temperature coefficient of the Zener diodes, and the negative temperature coefficient of the emitter diodes of the transistors.

The efficiency of the circuit drops off at low power levels. This is due to the fact that the losses of the circuit are not proportional to the output power. Maximum efficiency occurs at about 80% of full power.

Regulation over the power output range is less than 0.6%. Whenever the input voltage increases above 28 volts, the output voltage tracks the input. The difference between the two voltages is the drop in the flyback diode.

A1.4.2 CIRCUIT DETAILS

The principal components, L1, Q1, D1 and C1 are physically large and occupy most of the space in the regulator. Q1 is a 10A Darlington transistor in a TO-3 case. C1 includes two capacitors each one capable of sustaining full load, so that the

regulator can remain serviceable should one of the capacitors fail.

All the transistor driving circuitry has been placed on the printed circuit board. The oscillator, which includes R13, R14, R15, C6 and Q6, is a normal unijunction transistor oscillator operating at about 9 KHz. It is coupled to the monostable multivibrator through C5. Q2, and Q5 are the two transistors, along with biasing and timing components R4, R6, R8, R11, R12 and C4, which form the monostable vibrator. Pulse width modulation is achieved by injecting current into the base of Q2. R1, R2, R7, P1, C2, Q3 and Q4 form the output voltage sensing circuitry. R9, D2 and C3 form a reference voltage.

In the quiescent state Q2 is conducting and Q5 is non-conducting. When Q5 is triggered on by a pulse from Q6, through C5 Q2 is turned off by a negative pulse through C4. The relaxation time of R8 and C4 determine the maximum duty cycle of Q2. If the output voltage is sufficiently high the voltage on the tap of P1 approaches the reference level of D2. Q3 turns off and Q4 turns on, driving the base of Q2 from the collector of Q4 and reducing the "off" duty cycle of Q2. This reduces the "on" duty cycle of Q1 which completes the feedback loop.

Table A7: Switching Regulator Parts List

Q1 DTS 1020, Delco	R3 220 0.5w, 5%
Q2 2N930	R4 1500 0.5w, 5%
Q3 2N3251	R5 6800 0.5w, 5%
Q4 2N3251	R6 1500 0.5w, 5%
Q5 2N930	R7 1800 0.5w, 5%
Q6 2N1671B	R8 150K 0.5w, 5%
C1 22,000 ufd, 35 V (x2)	R9 680 0.5w, 5%
C2 50 ufd, 15 V, 10%	R10 62K 0.5w, 5%
C3 220 ufd, 25 V, 10%	R11 1800 0.5w, 5%
C4 680pfd, 10%	R12 1500 0.5w, 5%
C5 0.0033 ufd, 10%	R13 680 0.5w, 5%
C6 0.033 ufd, 10%	R14 120 0.5w, 5%
D1 1N3889	R15 47K 0.5w, 5%
D2 18 V, 1 watt Zener	P1 500 Ohm, 10 Turn
R1 1200 0.5w, 5%	L1 1.1 mH, 16AWG on
R2 1800 0.5w, 5%	Armaco FBC core

Miscellaneous:

1 - Wafer switch, 4 position, single pole

1 - Tungsten panel lamp, 28 V

1 - Panel meter, 50 VDC, KM-48, Hioki, with diode

1 - HKP Buss fuse holder, with 7.5 amp fuse

A1.5 THE CORNER REFLECTOR ANTENNA

The University of British Columbia radio echo sounder uses a two element, 90° corner reflector antenna. At 840 MHz, reflector type aperture antennae are convenient both in construction and application, and provide a high gain performance with relatively little sophistication. The 90° corner reflector compares favourably in forward gain with the "ideal" parabolic reflector, and also reduces the 90° sidelobe level, important in consideration of air path reflections from valley walls. Forward gain of the University of B. C. antenna is 15 dB over isotropic, 10 dB provided by the corner reflector (Fig. A1.32), 3 dB from the double driven element and 2 dB by the dipole radiators.

A1.5.1 DESIGN DETAILS

The two driven elements, electric half-wave dipole radiators, are located approximately 0.4λ (150 mm) from the apex of the corner. Their centre-to-centre spacing is 1.5 λ (536 mm). At these points the nominal radiation resistance for each dipole is 100 Ω (see figure A1.33). Each dipole is fed separately by a 100 Ω coaxial cable. The 100 Ω coaxial cables form a "T" junction with a 50 Ω coaxial cable at a point which is an exact multiple of a half wavelength from the dipole feed centres. The 50 Ω coaxial cable is the power feed connection from(to) the radar transceiver. In this manner the dipoles are driven in phase with corresponding gain in the forward direction, and with an enhanced null in the E - plane 90° side

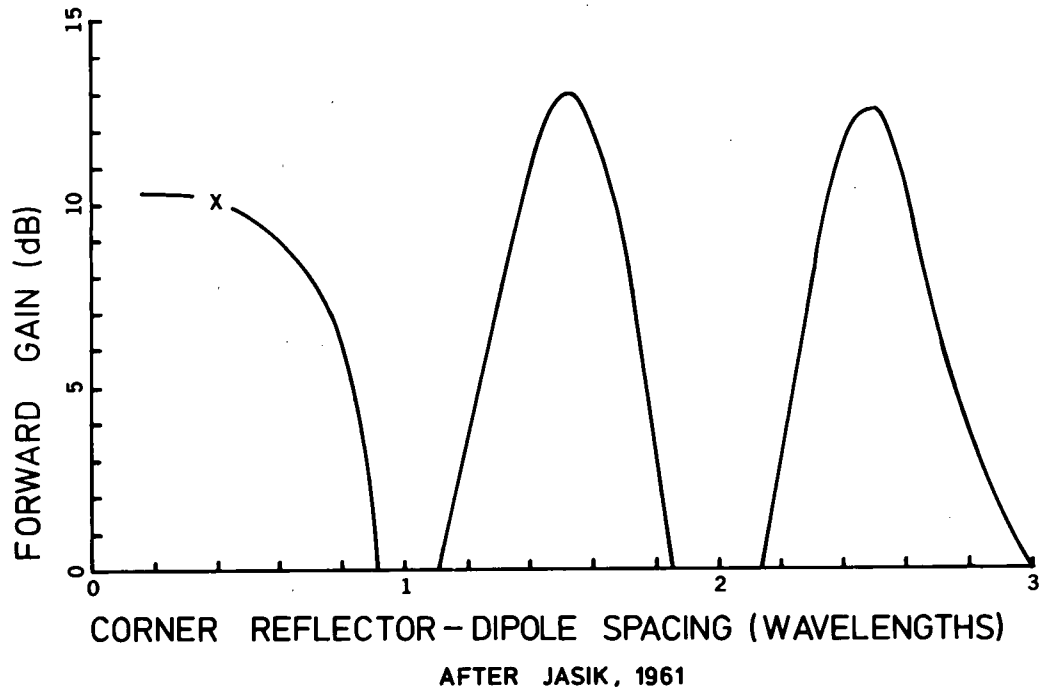

FIG. A1.32 CORNER REFLECTOR GAIN vs SPACING

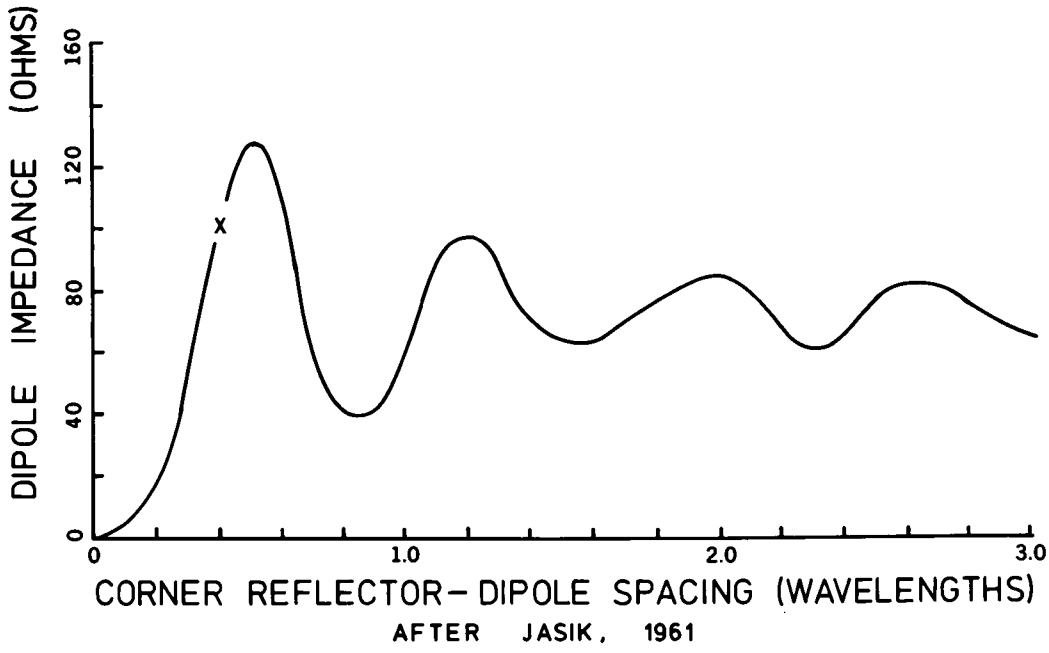

FIG. A1.33 CORNER REFLECTOR IMPEDANCE vs SPACING

lobe direction.

The dipole elements were designed and constructed for the University of British Columbia radio echo sounder by Sinclair Radio Laboratories Ltd., Burnaby, Canada. Each dipole comprises a broadband dipole element, balun and a PVC radome. Construction details are proprietary.

The reflector is fabricated of T6 aluminium tubing and channeling (Fig. A1.34). Each side of the reflector comprises eight 0.375" (9.5 mm) tubes suspended at 1.75" (44 mm) centres in 0.75" x 1.50" (19 mm x 38 mm) channels and held in place by rivets. The reflectors and dipole centre supports are bolted to two galvanized steel brackets, which determine the angle of the reflectors. All hardware is type AN.

In addition to the two driven elements a third parasitic element has been placed precisely half way between the two driven elements, and is held in place by a fibreglass extension of the radomes. The principal function of the extra element is to improve the VSWR of the antenna by isolating the two driven dipoles. The parasitic element consists of an aluminium tube approximately 20 mm diameter and 10% longer than 0.5λ .

The effect of the parasitic element is as follows. In the absence of a parasite, static RF fields around each driven element induce currents with 1.5 cycles delay in the other driven element resulting in power returning into the antenna feed and a poorer VSWR. The parasite interferes with the static field reducing the cross-over currents considerably.

The effect of the parasite on the antenna pattern is minimal. RF fields at the parasite are 0.75 cycles behind in

FIG. A1.34 THE CORNER REFLECTOR ANTENNA

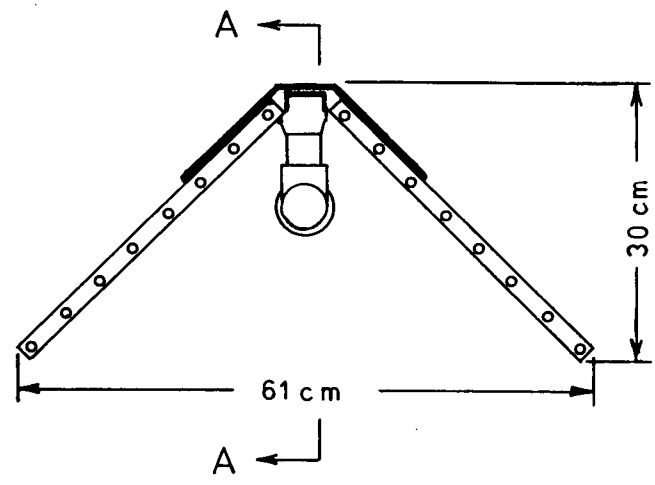

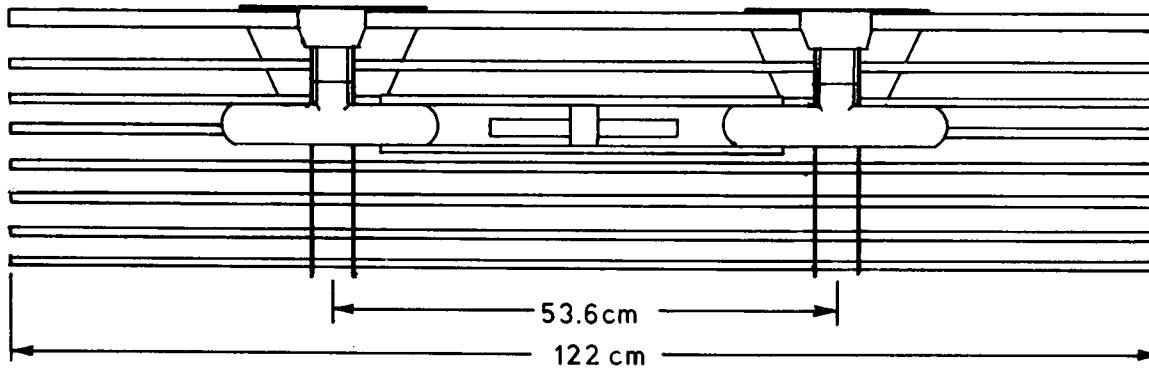

SECTION A-A

phase those being radiated at the driven dipole centres. The parasite must then reradiate power 0.75 cycles ahead of that being radiated from the driven dipoles. The slight elongation (relative to 0.5λ) of the parasitic element requires that the phase of the reradiation be advanced still further (cf. Jasik, H., 1961, reflector elements in Yagi antennae, p. 5-6). The net effect is that power reradiated from the parasitic element interferes constructively in the forward direction, with power being radiated by the driven dipoles. Assuming any reasonable parasitic element parameters however, results in additional forward gain being considerably less than 1 dB. Figure A1.35 shows a series of theoretical antennae patterns based on this model. G and H are E - plane and H - plane patterns respectively, for an antenna with a parasitic element reradiating power with 0.15 cycles phase lag delay and 10% power relative to power radiating from the driven elements. These patterns are probably closest to the real antenna pattern. A is the pattern calculated for the same antenna with no parasitic element.

Overleaf: Figure A1.35. Theoretical patterns for various corner reflector antennae. Each pattern has assumed the presence of an ideal 90° corner at 0.4λ spacing, with two driven dipoles. Only the parasitic dipole parameters have been varied. Pattern A shows the estimated pattern with no parasite present. The number above each of the other patterns represent first the assumed radiated power of the parasite relative to the driven dipoles, second the phase lag of the parasite radiation relative to the driven dipole radiation. The patterns plot relative power versus angle.

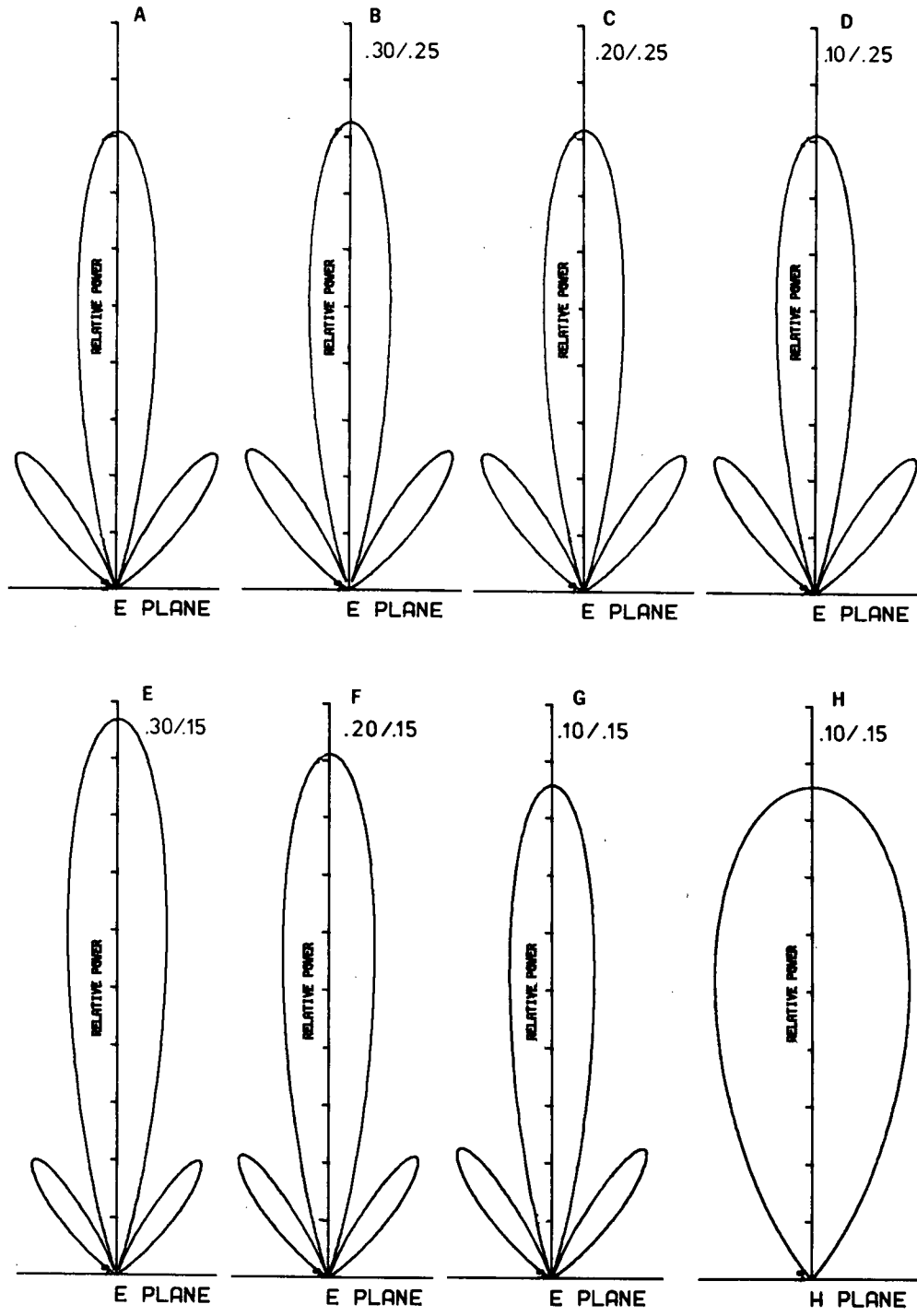
A
B
.30/.25
C
.20/.25
D
.10/.25
RELATIVE POWER
E PLANE
E
.30/.15
F
.20/.15
G
.10/.15
H
.10/.15
H PLANE

FIGURE A1.35

A1.5.2 CALIBRATION: VSWR AND FORWARD GAIN

Voltage standing wave ratios have been provided by Sinclair Radio Laboratories Ltd. VSWR is 1.14 at the centre frequency (840 MHz) and approximately 1.4 at the band edges (±20 MHz).

The forward gain of the antenna has been measured at vertical incidence over a lake by using the relation

$$\frac{P_R}{P_T} = \frac{\lambda^2 G^2}{64\pi^2 r^2} e^{-.10ML}$$

where P_R and P_T are received and transmitted power, r is the antenna altitude and L is the system losses in dB. The water surface has been assumed to be a perfect reflector.

Figure A1.36 is an echogram recorded over Kluane Lake. It was flown at 165 m above the surface (1.1 us delay) and shows a clear specular reflection with received power of +2 dBm ±2 dB. Pertinent data are in Table A8. It follows that

$$2G - (14 + 81) = -64 \text{ dB} \pm 2 \text{ dB or } G = 15.5 \text{ dB} \pm 1 \text{ dB}.$$

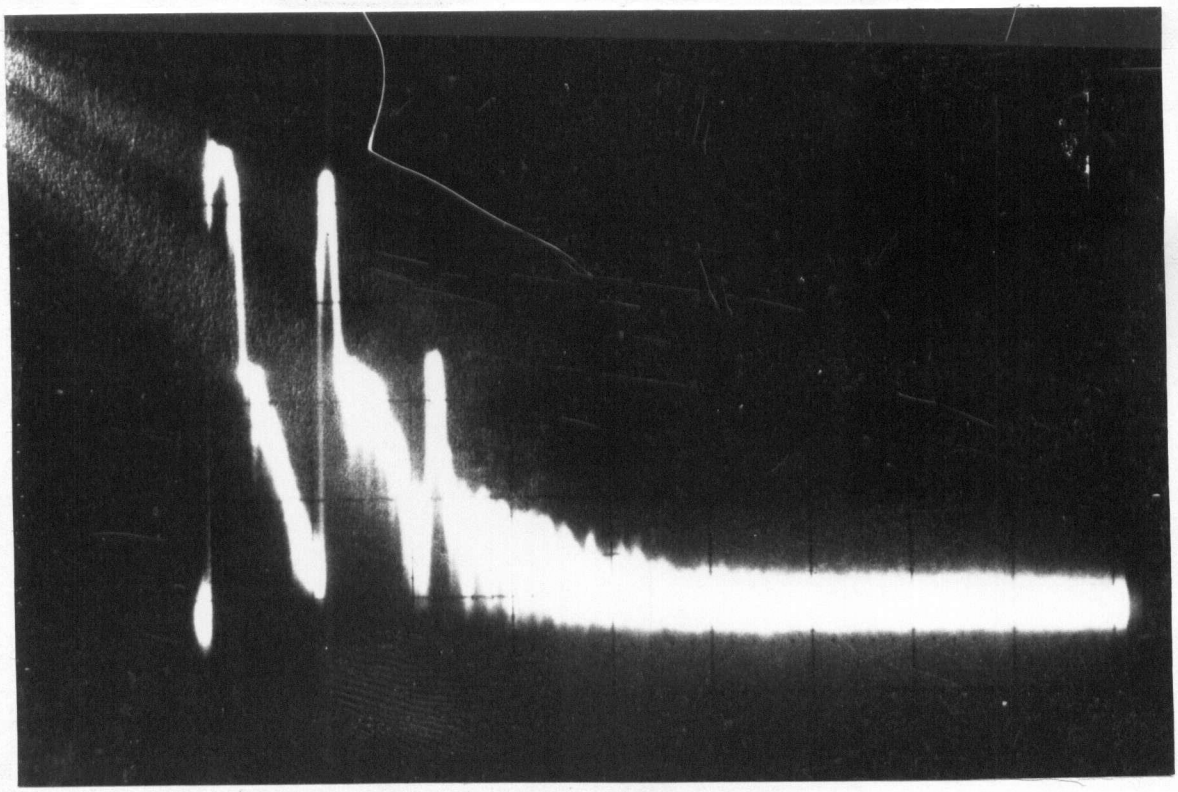

Figure A1.36. An A-scope echogram over Kluane Lake

The first pulse is the transmitted pulse. The second pulse is a +2 dBm reflection from the lake surface. The third pulse is a multiple reflection off the aircraft. The echo delay is 1.1 us indicating an aircraft clearance of 165 m.

Table A8: Forward Gain Measurement Data

Transmitted power (4 KW)	66 dBm
Received Power	2 dBm ±2 dB
System Losses:	
Circulator Insertion Loss	0.50 dB
I.F. Filter Insertion Loss	0.4 dB
Diode Limiter Insertion Loss	0.1 dB
Mixer Conversion Loss	10 dB
Cable Losses	2.7 dB
VSWR Losses	<1 dB
Total Losses:	14 dB
Geometric loss factor	-81 dB

APPENDIX 2: TRAPRIDGE GLACIER AND HAZARD GLACIER FLIGHT LINE MAPS

Figure A2.1 shows the positions of all controlled flight lines on the Trapridge Glacier. The map is a composite of three flights made on August 28 and 29, 1976. Ice depth data was successfully recorded along approximately 80% of these lines.

Figure A2.2 shows the positions of all controlled flight lines on the Hazard Glacier. Depth data were successfully taken along approximately 90% of these lines. The higher density was achieved by arranging for recorder dead time to occur at the glacier boundaries.

The three triangles on Figure A2.2 represent the three drill sites occupied during the surfaced based part of the field work (Napoleoni and Clarke, 1978). The asterisk represents the location of the frontispiece photograph.

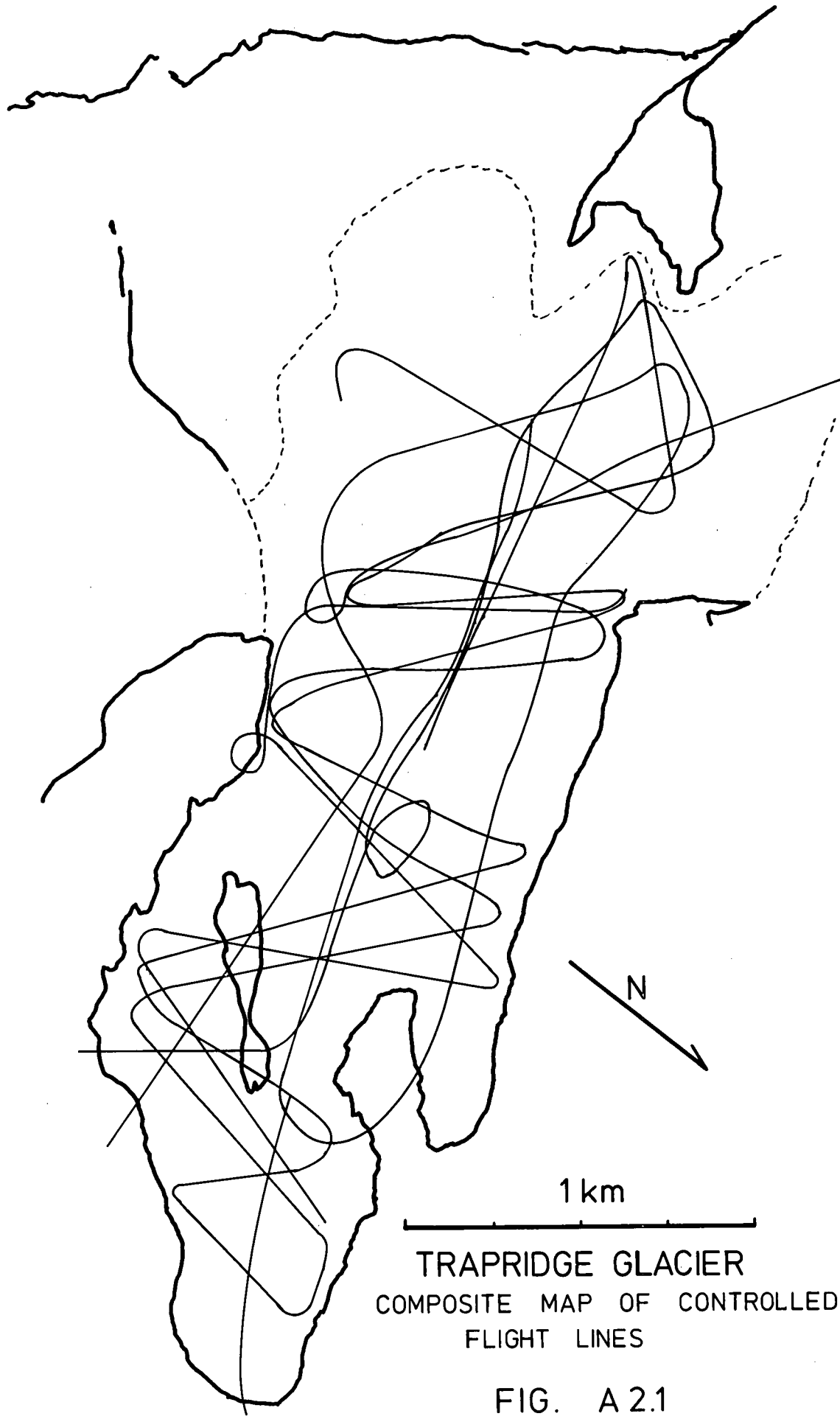

TRAPRIDGE GLACIER
COMPOSITE MAP OF CONTROLLED FLIGHT LINES

FIG. A 2.1

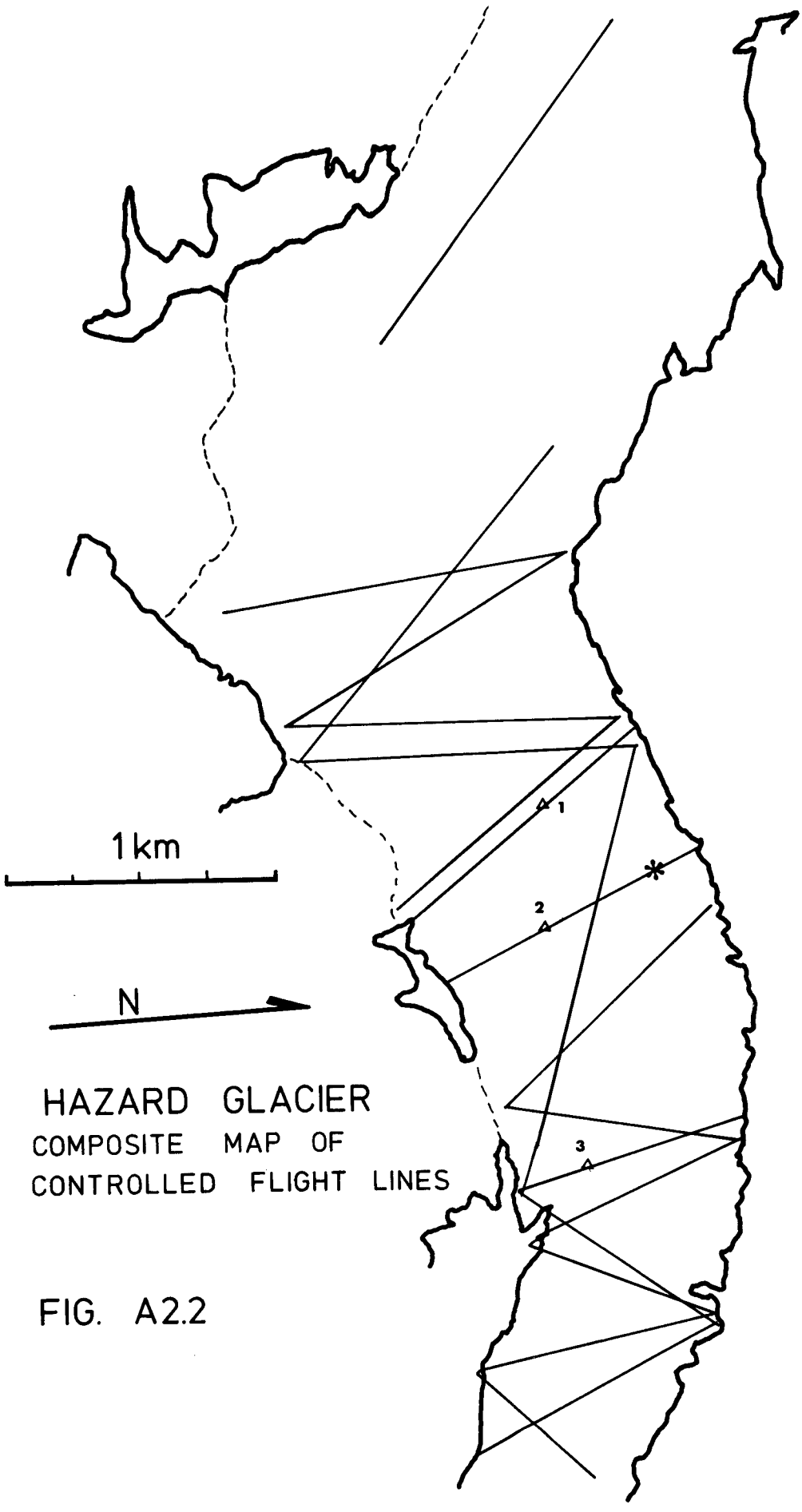

HAZARD GLACIER
COMPOSITE MAP OF
CONTROLLED FLIGHT LINES

FIG. A2.2

APPENDIX 3: DIFFRACTION FROM A LINEAR RIBBON SCATTERER

To decide if it is possible to detect a linear scatterer of spherical waves it becomes necessary to model the diffracted field for predetermined transmitter and receiver antennae. Three assumptions are convenient: that polarization effects are negligible, i.e., we need only to solve for the scalar wave solution (Berry, 1973), that the transmitter and receiver antennae are at the same location, and that the scattering object is horizontal.

The model used here assumes that the linear scatterer may be modelled as a flat, narrow ribbon with unit reflectivity. The width of the ribbon must be small in comparison to the dimension of a Fresnel zone, but sufficiently large that neglected "edge" diffraction terms are small relative to the total diffracted term. (A very thin line scatterer (small diameter relative to λ) scatters radiation always polarized parallel to the line (Huynen, 1978). With our 20 cm wavelength such small line scatterers likely will not exist in glaciers. This does not imply that scattering objects which do preferentially polarize backscattered radiation won't exist. Objects shaped like small dipoles will also have this property.)

A3.1 COORDINATE SYSTEMS

Three systems are useful for the following analysis. A rectilinear system, referenced to the antennae locates a point (X_1, X_2, X_3) on the object (Fig. A3.1). X_1 is the depth of the object below the antennae, X_2 is the distance to the point

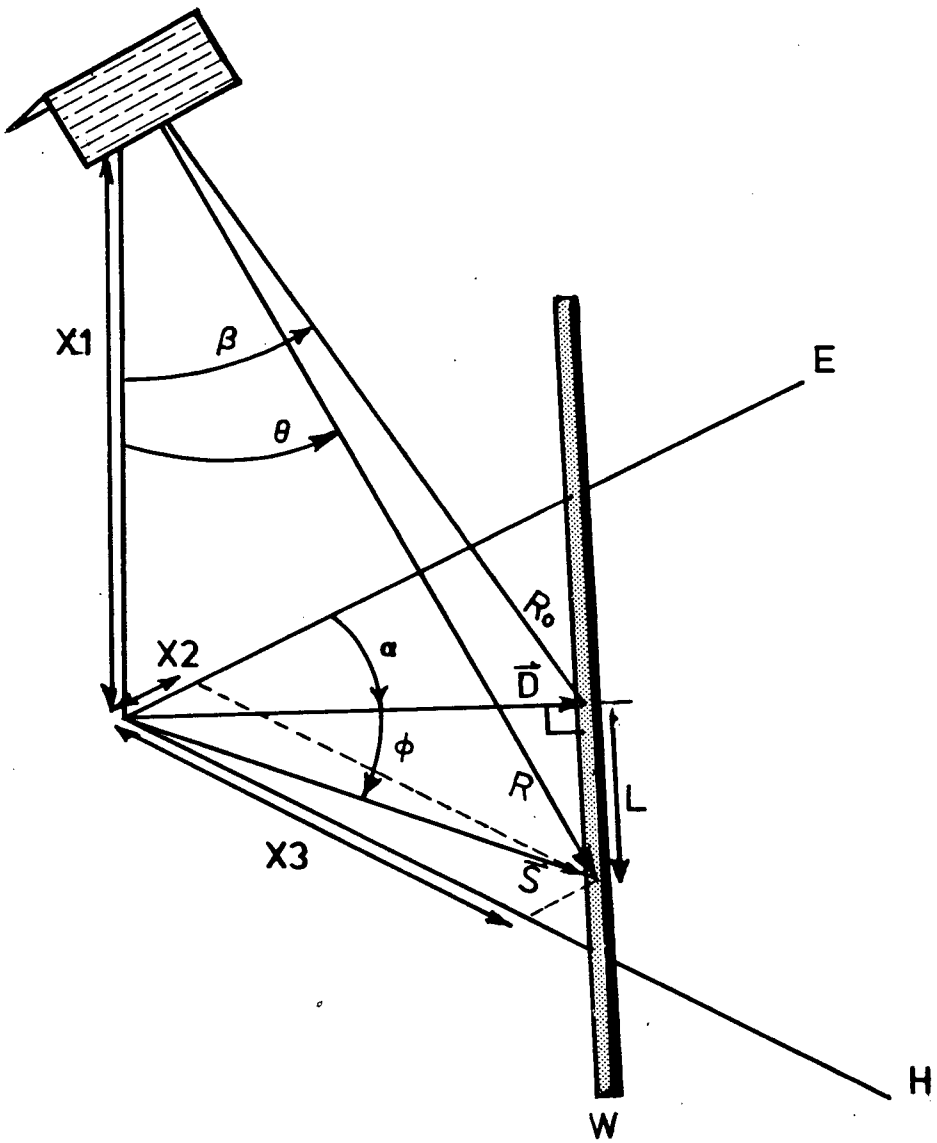

FIG. A3.1 SCHEMATIC OF RIBBON SCATTERER MODEL

parallel to the E-axis of an antenna, X_3 is the distance to the point normal to the E-axis of the antenna. Assume that all distances are measured in wavelengths.

Define a polar system relative to the antenna with θ the off-vertical angle, $\alpha + \phi$ (see below) the azimuth relative to the antenna E-axis, and R the radial distance.

A third system will also locate a point on the scattering object. Let β be the minimum off-vertical angle to points on the object. This defines a horizontal vector $\overline{D}$ normal to the object. Let α be the azimuth of the vector $\overline{D}$ relative to the antenna E-axis. Let the endpoint of $\overline{D}$ define the origin of an L-axis along the object, with L increasing as increases through zero. It follows that

$$\begin{aligned} D &= |\overline{D}| = X_1 \tan\beta \\ X_2 &= -L\sin\alpha + D\cos\alpha \\ X_3 &= L\cos\alpha + D\sin\alpha . \end{aligned} \qquad \text{(A3..1)}$$

It follows that

$$\begin{aligned} \frac{X_2}{X_1} &= \left\{ -\frac{L}{D}\sin\alpha + \cos\alpha \right\} \tan\beta \\ \frac{X_3}{X_1} &= \left\{ \frac{L}{D}\cos\alpha + \sin\alpha \right\} \tan\beta \end{aligned} \qquad \text{(A3.2)}$$

and

$$\tan^2\theta = \frac{X_2^2 + X_3^2}{X_1^2} = \left\{ \frac{L^2}{D^2} + 1 \right\} \tan^2\beta$$
$$= \frac{L^2}{X_1^2} + \tan^2\beta \qquad \text{(A3.3)}$$

and that

$$\tan\phi = \frac{L}{D} = \frac{L}{X_1} \cot\beta \qquad \text{(A3.4)}$$

By introducing a parameter $\xi = L/X_1$ these reduce to

$$\theta = \theta(\xi, \beta) = \arctan(\xi^2 + \tan^2\beta)^{1/2}$$
$$\phi = \phi(\xi, \beta) = \arctan(\xi \cot\beta) \qquad \text{(A3.5)}$$

A3.2 THE KIRCHHOFF INTEGRAL

The following analysis is modelled after Berry (1972). The received electromotive force (EMF) from a linear ribbon scatterer may be estimated with Kirchhoff's formula (see eg. Longhurst, 1957, p. 192, eq'n 10-15). Assuming $X_1 >> \lambda$, which is reasonable during echo sounding,

$$d\Psi = - d\Sigma \frac{F'(t-2R/c)\cos\theta}{2\pi c R^2} \tag{A3.6}$$

where $d\Psi$ is the received contribution from area element $d\Sigma$, and F is a quasisinosoidal wavefunction of finite duration. (See eg. Longhurst, 1957, p. 193, eq'n 10-16; Berry, 1972, eq'n A-1). Integrating over the horizontal plane,

$$\begin{aligned}\Psi(t) &= \frac{-1}{2\pi c}\iint \frac{F'(t-2R/c)}{R^3} X_1 \, d\Sigma \\ &= \frac{-1}{2\pi c}\iint \frac{F'(t-2R/c)}{RX_1}\cdot\frac{X_1^2}{R^2} \, d\Sigma \\ &= \frac{-1}{2\pi c}\iint \frac{F'(t-2R/c)}{RX_1}\left[1-\frac{S^2}{R^2}\right] d\Sigma\end{aligned} \tag{A3.7}$$

where $S=(X_2^2+X_3^2)^{1/2}$ is the length of the horizontal vector $\bar{S}=(X_2,X_3)$ from the subantenna point to a specified point in the horizontal plane. Since

$$S^2 = \bar{S}\cdot\bar{S} = \bar{S}\cdot\bar{\nabla}_s R \tag{A3.8}$$

it follows that

$$\Psi(t) = \frac{-1}{2\pi c}\iint \frac{F'(t-2R/c)}{RX_1}\left[1 - \frac{\bar{S}\cdot\bar{\nabla}_s R}{R^2}\right] d\Sigma \qquad \text{(A3.9)}$$

By vector identity (see, e.g. Panofsky and Phillips, 1962, p. 471, eq'n 7)

$$\bar{\nabla}\cdot(\psi\,\bar{A}) = \bar{A}\cdot\bar{\nabla}\psi + \psi\,\bar{\nabla}\cdot\bar{A}$$

$$-\bar{\nabla}_s\cdot\frac{F(t-2R/c)}{R^2X_1}\bar{S} = \frac{\bar{S}\cdot\bar{\nabla}_s F(t-2R/c)}{R^2X_1} + F(t-2R/c)\,\bar{\nabla}_s\cdot\left[\frac{\bar{S}}{R^2X_1}\right] \qquad \text{(A3.10)}$$

By the divergence theorem the integral over the left side of A3.10 vanishes (see, e.g. Stratton, 1941, p. 429, eq'n 34). Thus

$$\iint F(t-2R/c)\,\bar{\nabla}_s\left[\frac{\bar{S}}{R^2X_1}\right] d\Sigma = -\iint \frac{\bar{S}\cdot\bar{\nabla}_s F(t-2R/c)}{R^2X_1}\, d\Sigma = \frac{2}{c}\iint \frac{F'(t-2R/c)}{R^2X_1}\,\bar{S}\cdot\bar{\nabla}_s R\, d\Sigma \qquad \text{(A3.11)}$$

Thus with A3.9

$$\Psi(t) = \frac{-1}{2\pi c}\iint \frac{F'(t-2R/c)}{R^2 X_1}\, d\Sigma + \frac{1}{4\pi}\iint F(t-2R/c)\,\bar{\nabla}_s\cdot\left[\frac{\bar{S}}{R^2 X_1}\right] d\Sigma \qquad \text{(A3.12)}$$

Evaluating the divergence term in the second integral

$$\bar{\nabla}_s\cdot\left[\frac{\bar{S}}{R^2 X_1}\right] = \frac{\partial}{\partial X_2}\left[\frac{X_2}{X_1(X_1^2+X_2^2+X_3^2)}\right] + \frac{\partial}{\partial X_3}\left[\frac{X_3}{X_1(X_1^2+X_2^2+X_3^2)}\right]$$

$$= \frac{2X_1(X_1^2+X_2^2+X_3^2) - 2X_1X_2 - 2X_1X_3}{X_1^2(X_1^2+X_2^2+X_3^2)^2}$$

$$= \frac{2X_1^3}{X_1^2(X_1^2+X_2^2+X_3^2)^2}$$

$$= \frac{2X_1}{(X_1^2+X_2^2+X_3^2)^2} = \frac{2X_1}{R^4} \qquad \text{(A3.13)}$$

Thus with A3.12

$$\Psi(t) = \frac{-1}{2\pi c}\iint \frac{F'(t-2R/c)}{RX_1}\, d\Sigma + \frac{1}{2\pi}\iint F(t-2R/c)\frac{X_1}{R^4}\, d\Sigma \qquad \text{(A3.14)}$$

Since F is quasi-sinosoidal with predominant frequency, say ω_o ,

$$|F'| \cong \omega_o |F| \tag{A3.15}$$

As assumed $\lambda << X_1, R$ hence

$$\frac{1}{R} \ll \frac{\omega_o}{c} \tag{A3.16}$$

Thus the second term in the integral can be neglected, and

$$\Psi(t) \cong \frac{-1}{2\pi c} \iint \frac{F'(t-2R/c)}{R X_1} \, d\Sigma \tag{A3.17}$$

The effects of antenna patterns weight the integrand. For transmitter pattern $G_T(\theta, \phi)$ then

$$\Psi(t) \cong \frac{-1}{2\pi c} \iint \frac{F'(t-2R/c)}{R X_1} G_T \, d\Sigma \tag{A3.18}$$

If the linear scatterer is modelled as a narrow ribbon of constant width with unit reflectivity on the ribbon and zero reflectivity off the ribbon then $d\Sigma$ can be replaced by dL or by $X_1 d\xi$ and the integral becomes a line integral

$$\Psi(t) \cong \frac{-1}{2\pi c} \int_{-W/2}^{W/2} \int_R \frac{F'(t-2R/c)}{R X_1} G_T \, dL \, dw \tag{A3.19}$$

where dw runs across the width, W, of the ribbon. Two assumptions are required for this expression; that the ribbon is sufficiently narrow that across its width the integrand is

effectively constant, that effects caused by the discontinuity at the ribbon edge can be ignored. The first assumption requires that the width of the ribbon be, at any point, well within one Fresnel zone. The phase difference across the ribbon, P_W

$$P_W = \left\{ X_1^2 + \left[X_2 + \frac{w\cos(\phi+\alpha)}{2} \right]^2 + \left[X_3 + \frac{w\sin(\phi+\alpha)}{2} \right]^2 \right\}^{1/2}$$

$$- \left\{ X_1^2 + \left[X_2 - \frac{w\cos(\phi+\alpha)}{2} \right]^2 + \left[X_3 - \frac{w\sin(\phi+\alpha)}{2} \right]^2 \right\}^{1/2}$$

$$= \left\{ X_1^2 + X_2^2 + X_3^2 + \frac{w^2}{4} + \left[X_2 w\cos(\phi+\alpha) + X_3 w\sin(\phi+\alpha) \right] \right\}^{1/2}$$

$$- \left\{ X_1^2 + X_2^2 + X_3^2 + \frac{w^2}{4} - \left[X_2 w\cos(\phi+\alpha) + X_3 w\sin(\phi+\alpha) \right] \right\}^{1/2} \qquad \text{(A3.20)}$$

The maximum for P_W occurs at $\phi = 0$ since

$$\frac{\partial}{\partial \phi} \left(X_2 w\cos(\phi+\alpha) + X_3 w\sin(\phi+\alpha) \right)$$

$$= -wX_2\sin(\phi+\alpha) + wX_3\cos(\phi+\alpha) = 0 \qquad \text{(A3.21)}$$

if and only if $\phi = 0$. At this point (the L origin)

$$P_{wmax} = \left\{X_1^2 + (D + \frac{W}{2})^2\right\}^{1/2} - \left\{X_1^2 + (D - \frac{W}{2})^2\right\}^{1/2}$$

$$= \left\{X_1^2 + D^2 + \frac{W^2}{4} + Dw\right\}^{1/2} - \left\{X_1^2 + D^2 + \frac{W^2}{4} - Dw\right\}^{1/2}$$

$$\cong \left\{R_o^2 + R_o w \sin\beta\right\}^{1/2} - \left\{R_o^2 - R_o w \sin\beta\right\}^{1/2} \qquad (A3.22)$$

where $R^2 = X_1^2 + D^2$ and we assume $W \ll D, X_1$. It follows that

$$P_{wmax} \cong (R_o + \frac{w\sin\beta}{2}) - (R_o - \frac{w\sin\beta}{2}) \qquad (A3.23)$$

Thus the assumption is satisfied if $W\sin\beta \ll 1$.

Because of its quasi-periodicity we shall take

$$F(t) = A e^{i\omega_o t}$$

Thus the retarded time derivative

$$F'(t) = i\omega_o e^{i\omega_o t} A e^{-i4\pi P(\theta, \phi, X_1)} \qquad (A3.24)$$

where A is an arbitrary amplitude, P is a phase delay function expressed in cycles which determines the retarded potential relative to the L origin (see below), and the time dependence has been factored out. The i indicates a $\pi/2$ phase shift and can be neglected in this calculation.

The effective field strength as measured by the receiver

antenna also weights the contribution from the scatterer by a gain factor $G_R(\theta,\phi)$. Thus

$$\Psi = \frac{\omega_o A w}{2\pi c}\int \frac{G_T G_R}{R}\, e^{-i4\pi P(\theta,\phi,X_1)}\, d\xi \qquad \text{(A3.25)}$$

where the dependence of θ and ϕ on ξ are as stated in A3.5. Finally, if the transmitter and receiver antennae are rotated by α_T and α_R with respect to the linear scatterer then

$$\Psi = K\int \frac{G_T(\theta,\alpha_T+\phi)\, G_R(\theta,\alpha_R+\phi)}{R}\, e^{-i4\pi P(\theta,\phi,X_1)}\, d\xi \qquad \text{(A3.26)}$$

with $K = \omega_o A w/2\pi c$. For the ξ, β coordinate system since

$$R^2 = L^2 + D^2 + X_1^2 \qquad \text{(A3.27)}$$

and

$$(R - cP)^2 = D^2 + X_1^2 \qquad \text{(A3.28)}$$

then

$$\begin{aligned} cP &= (L^2 + D^2 + X_1^2)^{1/2} - (D^2 + X_1^2)^{1/2} \\ &= X_1\left\{\left(\left(\frac{L}{X_1}\right)^2 + \left(\frac{D}{X_1}\right)^2 + 1\right)^{1/2} - \left(\left(\frac{D}{X_1}\right)^2 + 1\right)^{1/2}\right\} \\ &= X_1\left\{(\xi^2 + \tan^2\beta + 1)^{1/2} - (\tan^2\beta + 1)^{1/2}\right\} \\ &= X_1\left\{(\xi^2 + \sec^2\beta)^{1/2} - \sec\beta\right\} \end{aligned} \qquad \text{(A3.29)}$$

The Kirchhoff integral may be rewritten

$$\Psi = \frac{K}{X_1} \int G(\theta, \alpha_T + \phi)\, G(\theta, \alpha_R + \phi) \cos\theta\, e^{-i4\pi P(\theta, \phi, X_1)}\, d\xi \qquad \text{(A3.30)}$$

where the antennae gain functions have been assumed to be identical.

A3.3 NUMERICAL RATIONALIZATION

The integral is not yet numerically tractable because $e^{-i4\pi P}$ is a rapidly varying function of ξ. We wish to let dP become the integrating variable which requires having the inverse function of P. For a given X_1, β we have

$$X_1 \left\{ (\xi^2 + \sec^2\beta)^{1/2} - \sec\beta \right\} = P \qquad \text{(A3.31)}$$

Then

$$\xi = \pm \left\{ \left(\frac{P}{X_1} + \sec\beta \right)^2 - \sec^2\beta \right\}^{1/2} \qquad \text{(A3.32)}$$

and

$$\frac{\partial \xi}{\partial P} = \pm \frac{1}{2\left\{\left(\frac{P}{X_1} + \sec\beta\right)^2 - \sec^2\beta\right\}^{1/2}} \cdot 2\left(\frac{P}{X_1} + \sec\beta\right) \cdot \frac{1}{X_1}$$

$$= \pm \frac{1}{X_1} \cdot \frac{1 + \frac{X_1 \sec\beta}{P}}{\left\{1 + 2\frac{X_1 \sec\beta}{P}\right\}^{1/2}} \qquad \text{(A3.33)}$$

The Kirchhoff integral then becomes

$$\Psi = \frac{K}{X_1^2} \int_0^\infty \left\{G(\theta, \alpha_T + \phi) G(\theta, \alpha_R + \phi) + G(\theta, \alpha_T - \phi) G(\theta, \alpha_R - \phi)\right\}$$

$$\cdot \cos\theta \; e^{-i4\pi P} \cdot \frac{1 + \frac{R_0}{P}}{\left\{1 + 2\frac{R_0}{P}\right\}^{1/2}} \, dP \qquad \text{(A3.34)}$$

where the integral has been rewritten to account for the duplicity of ξ as a function of P. The integral has been written to run from 0 to ∞. The integral from $-\infty$ to 0 has been folded onto the positive limb by adding $G(\theta, \alpha_T - \phi) G(\theta, \alpha_R - \phi)$ to the positive ϕ arguments at the same P value. Again note that θ and ϕ are functions of ξ, and thus are functions of P.

The integral is now in a numerically tractable form. The pole at the origin is removable by subtracting

$$G(\beta,\alpha_T)\,G(\beta,\alpha_R)\cos\beta\, e^{-i4\pi P}\sqrt{\frac{2R_0}{P}} \qquad \text{(A3.35)}$$

from the integrand since as P tends to 0

$$\frac{1+\frac{R_0}{P}}{\left\{1+2\,\frac{R_0}{P}\right\}^{1/2}} \longrightarrow \left\{\frac{R_0}{P}\right\}^{1/2}$$

Note that a factor of two has been absorbed into the radical from the duplicity at $\phi = 0$. The value of the pole is

$$G(\beta,\alpha_T)\,G(\beta,\alpha_R)\cos\beta\int_0^{\infty}\frac{1}{\sqrt{P}}\, e^{-i4\pi P}\,dP \cdot (2X_1\sec\beta)^{1/2}$$

$$= \left[\frac{1-i}{2\sqrt{2}}\right] G(\beta,\alpha_T)\,G(\beta,\alpha_R)\cos\beta\,(2X_1\sec\beta)^{1/2} \qquad \text{(A3.36)}$$

(Gradshteyn and Ryzhik, 1965, p.420, eq'ns 3.757.1 & 3.757.2)

Set

$$J(P) = \left\{G(\theta,\alpha_T+\phi)\,G(\theta,\alpha_R+\phi) + G(\theta,\alpha_T-\phi)\,G(\theta,\alpha_R-\phi)\right\}$$

$$\cdot\cos\theta\cdot\frac{1+\frac{R_0}{P}}{\left\{1+\frac{2R_0}{P}\right\}^{1/2}} - G(\beta,\alpha_T)\,G(\beta,\alpha_R)\cos\beta\left[\frac{2R_0}{P}\right]^{1/2} \qquad \text{(A3.37)}$$

with

$$\sec\theta = \sec\beta\,\left(1+\frac{R_0}{P}\right) \qquad \text{(A3.38)}$$

and

$$\tan\phi = \frac{\left\{1 + 2\frac{R_o}{P}\right\}^{1/2}}{\frac{R_o}{P}} \csc\beta \qquad \text{(A3.39)}$$

A3.38 and A3.39 follow from A3.5 and A3.32. From A3.5

$$\tan^2\theta = \xi^2 + \tan^2\beta$$

$$\rightarrow \sec^2\theta = \xi^2 + \sec^2\beta$$

$$\rightarrow X_1(\sec\theta - \sec\beta) = P$$

$$\rightarrow X_1\sec\theta = P + X_1\sec\beta = P + R_o$$

$$\rightarrow \sec\theta = \left\{\frac{P+R_o}{X_1}\right\} = \sec\beta\left\{\frac{P+R_o}{R_o}\right\} = \sec\beta\left\{1 + \frac{P}{R_o}\right\}$$

Also from A3.5

$$\tan\phi = \xi \cot\beta$$

$$\rightarrow \tan^2\phi = \xi^2\cot^2\beta = \left\{\left(\frac{P}{X_1} + \sec\beta\right)^2 - \sec^2\beta\right\}\cot^2\beta$$

$$= \left\{\frac{P^2}{X_1^2} + \frac{2P}{X_1}\sec\beta\right\}\cot^2\beta = \left\{\frac{P^2}{X_1^2\sec^2\beta} + \frac{2P}{X_1\sec\beta}\right\}\cot^2\beta\sec^2\beta$$

$$= \frac{1 + 2\left\{\frac{P}{X_1\sec\beta}\right\}^{-1}}{\frac{P^2}{X_1^2\sec^2\beta}}\csc^2\beta = \frac{1 + \frac{2R_0}{P}}{\frac{P^2}{R_0^2}}\csc^2\beta$$

$$\rightarrow \tan\phi = \frac{\left\{1 + \frac{2R_0}{P}\right\}^{1/2}}{\frac{R_0}{P}}\csc\beta$$

A3.4 NUMERICAL ANALYSIS

Consider a full cycle of P, i.e. $e^{i4\pi P}$ where P goes from N to $N+\frac{1}{2}$. If we break up the interval into four equal intervals (N,N+1/8), (N+1/8,N+1/4), (N+1/4,N+3/8), (N+3/8,N+1/2) we can evaluate the integral piecewise for the real and imaginary terms. Call $J(N)=J^0$, $J(N+1/8)=J^1$, $J(N+1/4)=J^2$, $J(N+3/8)=J^3$, $J(N+1/2)=J^4$ and assume that the function J is piecewise linear on the subintervals. Then the integral may be evaluated as follows (see Fig. A3.2):

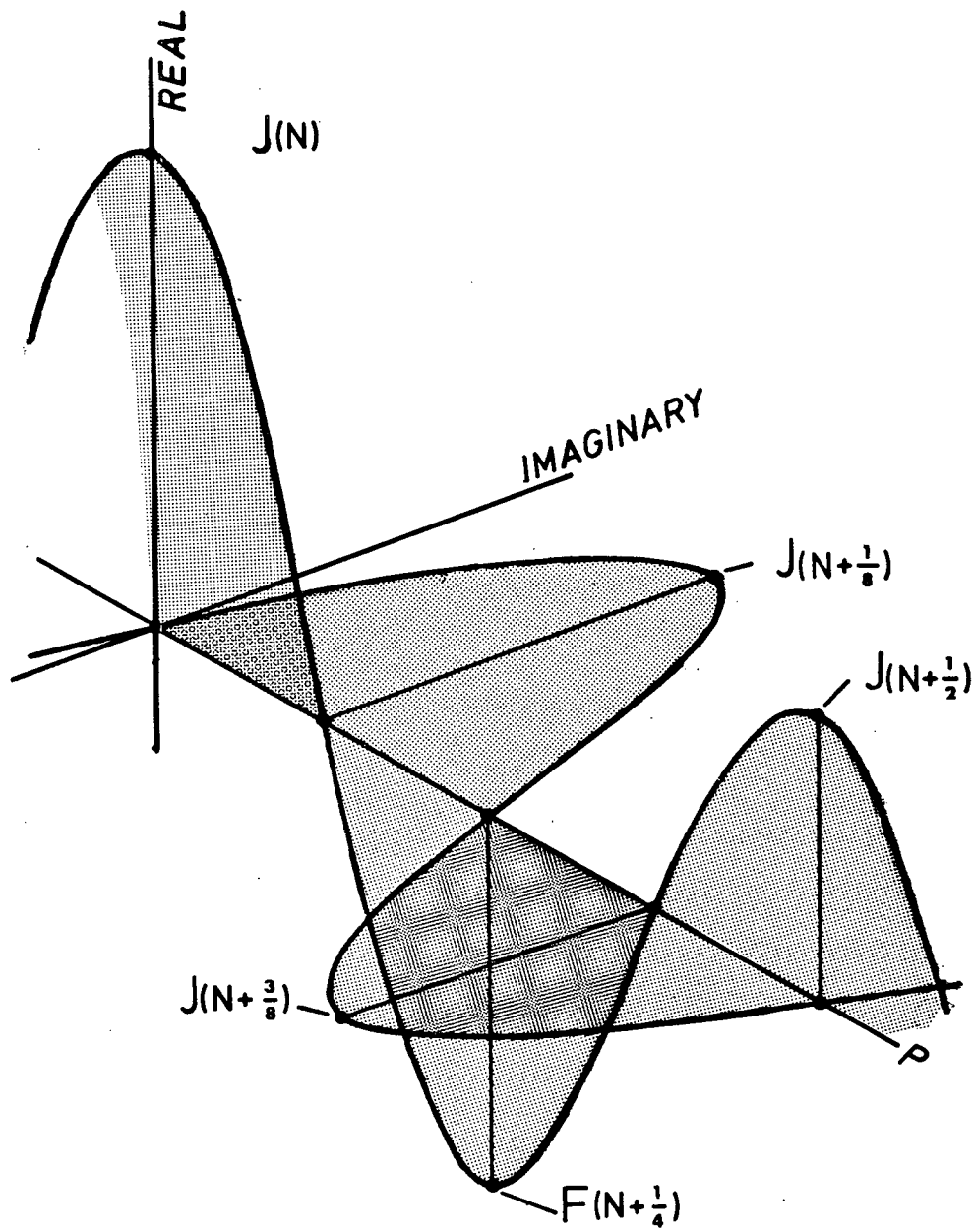

FIG. A3.2 KIRCHHOFF DIFFRACTION PICTORIAL OF NUMERICAL MODEL

Real component =

$$
\begin{aligned}
&(N, N+\tfrac{1}{8}) && \int_0^{1/8} (J^0 + 8P\Delta J^0)\cos 4\pi P\, dP \\
&(N+\tfrac{1}{8}, N+\tfrac{1}{4}) && -\int_0^{1/8} (J^1 + 8P\Delta J^1)\sin 4\pi P\, dP \\
&(N+\tfrac{1}{4}, N+\tfrac{3}{8}) && -\int_0^{1/8} (J^2 + 8P\Delta J^2)\cos 4\pi P\, dP \\
&(N+\tfrac{3}{8}, N+\tfrac{1}{2}) && +\int_0^{1/8} (J^3 + 8P\Delta J^3)\sin 4\pi P\, dP
\end{aligned}
\qquad \text{(A3.40.1)}
$$

Imaginary component =

$$
\begin{aligned}
&-\int_0^{1/8} (J^0 + 8P\Delta J^0)\sin 4\pi P\, dP \\
&-\int_0^{1/8} (J^1 + 8P\Delta J^1)\cos 4\pi P\, dP \\
&+\int_0^{1/8} (J^2 + 8P\Delta J^2)\sin 4\pi P\, dP \\
&+\int_0^{1/8} (J^3 + 8P\Delta J^3)\cos 4\pi P\, dP
\end{aligned}
\qquad \text{(A3.40.2)}
$$

where $\Delta J^N = J^{N+1} - J^N$.

By changing to variable x=8P, the eight components become

Real components:

$$\frac{1}{8}\int_0^1 (J^0 + x\Delta J^0)\cos\frac{\pi}{2}x\,dx$$

$$-\frac{1}{8}\int_0^1 (J^1 + x\Delta J^1)\sin\frac{\pi}{2}x\,dx$$

$$-\frac{1}{8}\int_0^1 (J^2 + x\Delta J^2)\cos\frac{\pi}{2}x\,dx$$

$$+\frac{1}{8}\int_0^1 (J^3 + x\Delta J^3)\sin\frac{\pi}{2}x\,dx$$

Imaginary components:

$$-\frac{1}{8}\int_0^1 (J^0 + x\Delta J^0)\sin\frac{\pi}{2}x\,dx$$

$$-\frac{1}{8}\int_0^1 (J^1 + x\Delta J^1)\cos\frac{\pi}{2}x\,dx$$

$$+\frac{1}{8}\int_0^1 (J^2 + x\Delta J^2)\sin\frac{\pi}{2}x\,dx$$

$$+\frac{1}{8}\int_0^1 (J^3 + x\Delta J^3)\cos\frac{\pi}{2}x\,dx \qquad \text{(A3.41)}$$

Noting that

$$\int_0^1 \cos\tfrac{\pi}{2}x\,dx = \int_0^1 \sin\tfrac{\pi}{2}x\,dx = \int_0^{\pi/2} \tfrac{2}{\pi}\sin y\,dy = \tfrac{2}{\pi}$$

$$\int_0^1 x\cos\tfrac{\pi}{2}x\,dx = \int_0^{\pi/2} \tfrac{4}{\pi^2} y\cos y\,dy = \tfrac{4}{\pi^2}\left[\cos y + y\sin y\right]_0^{\pi/2}$$

$$= \tfrac{4}{\pi^2}\left[\tfrac{\pi}{2} - 1\right]$$

$$\int_0^1 x\sin\tfrac{\pi}{2}x\,dx = \int_0^{\pi/2} \tfrac{4}{\pi^2} y\sin y\,dy = \tfrac{4}{\pi^2}\left[\sin y - y\cos y\right]_0^{\pi/2}$$

$$= \tfrac{4}{\pi^2} \qquad \text{(A3.42)}$$

the eight terms reduce to

Real components:	Imaginary components:
$\frac{1}{4\pi}(J^0 + A\Delta J^0)$	$-\frac{1}{4\pi}(J^0 + B\Delta J^0)$
$-\frac{1}{4\pi}(J' + B\Delta J')$	$-\frac{1}{4\pi}(J' + A\Delta J')$
$-\frac{1}{4\pi}(J^2 + A\Delta J^2)$	$+\frac{1}{4\pi}(J^2 + B\Delta J^2)$
$+\frac{1}{4\pi}(J^3 + B\Delta J^3)$	$+\frac{1}{4\pi}(J^3 + A\Delta J^3)$

(A3.43)

where $A=(1-\frac{2}{\pi})$ and $B=(\frac{2}{\pi})$. Reformulating in terms of the J^N's

Real components:

$$\frac{1}{4\pi}\Big\{J^0(1-A)+J^1A - J^1(1-B)-J^2B - J^2(1-A)-J^3A + J^3(1-B)+J^4B\Big\}$$

Imaginary components:

$$\frac{1}{4\pi}\Big\{J^0(1-B)+J^1B - J^1(1-A)-J^2A + J^2(1-B)+J^3B + J^3(1-A)+J^4A\Big\} \qquad (A3.44)$$

These reduce to

Real components:

$$\frac{1}{4\pi}\Big\{J^0(1-A)+J^1(A+B-1) + J^2(A-B-1)+J^3(1-B-A) + J^4(B)\Big\}$$

Imaginary components:

$$\frac{1}{4\pi}\Big\{J^0(1-B)+J^1(A-B-1) + J^2(1-A-B)+J^3(1+B-A) + J^4(A)\Big\} \qquad (A3.45)$$

But

$$A+B-1 = 1-A-B = 0$$

$$A-B-1 = -\frac{4}{\pi}$$

J^0 and J^4 overlap on consecutive cycles. Thus for real components odd n contributions vanish and for imaginary components even n contributions vanish. All sustained terms have coefficient $1/\pi^2$. Thus a numerical formulation of the integral which assigns a single summation term to each piecewise

FIG. A3.3
FUNCTION "J" FOR CORNER REFLECTOR ANTENNA
$X_1 = 750$, $\alpha = 15°$, $\beta = 10°$

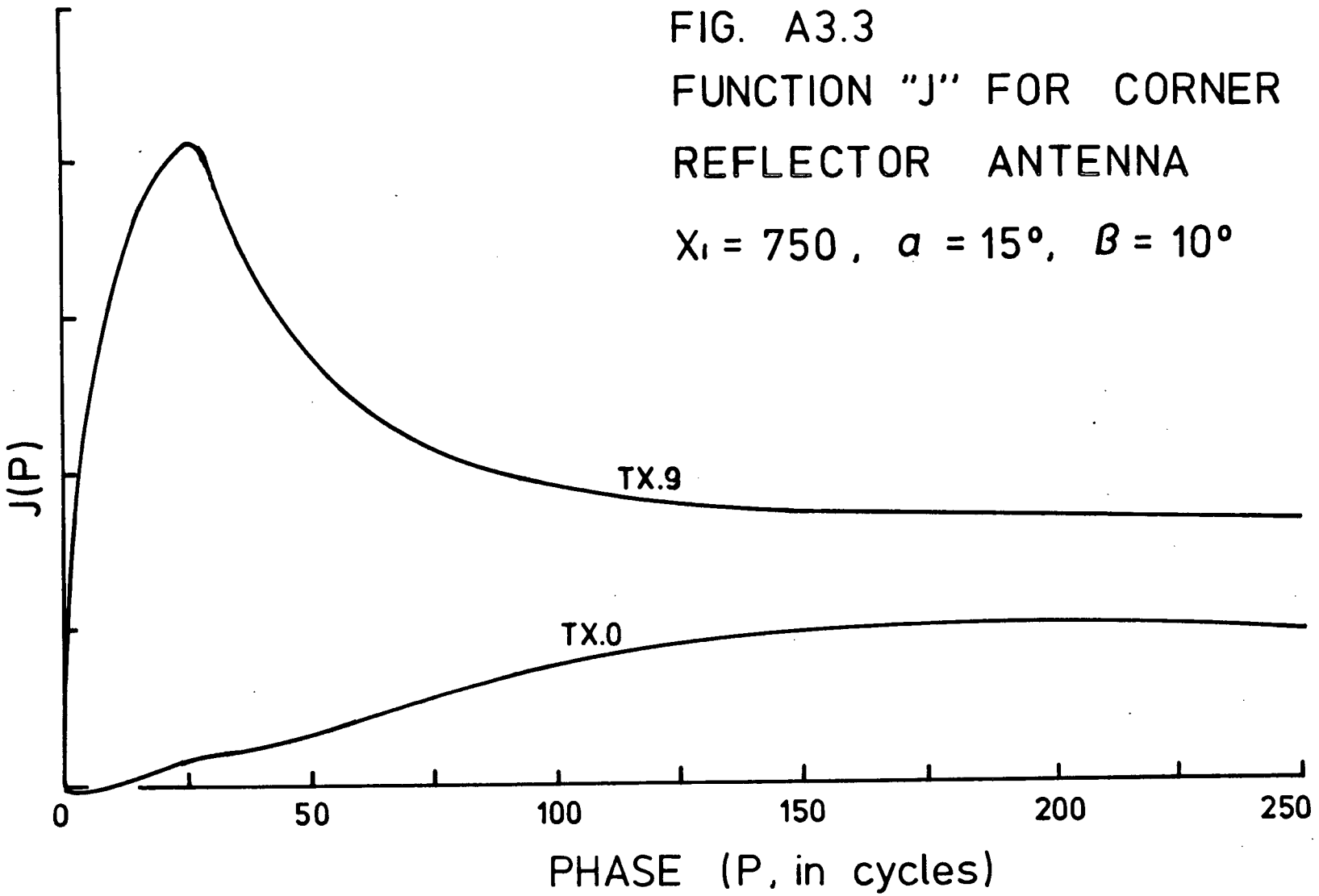

linearly weighted quarter cycle of the integrand is

$$\Psi = \frac{K}{X_1^2}\left\{\left[\frac{1-i}{2\sqrt{2}}\right]G(\beta,\alpha_T)G(\beta,\alpha_R)\cos\beta\,(2X_1\sec\beta)^{1/2} + \frac{1}{\pi^2}\sum_{P=1}^{\infty}J(\tfrac{P}{8})\cdot e^{-i\frac{\pi}{2}P}\right\} \tag{A3.46}$$

A3.5 PHYSICAL REALIZATION

Equation A3.18 is an exact solution for the isotropic radiator since

$$\begin{aligned}\Psi(t) &= \frac{-1}{2\pi c}\iint\frac{F'(t-2R/c)}{X_1 R}\,d\Sigma \\ &= \frac{-1}{2\pi c}\int_0^{\pi/2}\int_0^{\infty}\frac{F'(t-2R/c)}{X_1 R}\,S\,dS\,d\phi \\ &= \frac{-1}{X_1 c}\int_0^{\infty}\frac{F'(t-2R/c)}{R}\,S\,dS \\ &= \frac{-1}{X_1 c}\int_{X_1}^{\infty}F'(t-2R/c)\,dR \\ &= \frac{-1}{X_1 c}\cdot\frac{-c}{2}\cdot F(t-2X_1/c) = \frac{F(t-2X_1/c)}{2X_1}\end{aligned} \tag{A3.47}$$

We can show that A3.18 is also a reasonable expression for a large class of anisotropic radiators. Assume that a radiator

has a $\cos\theta$ distribution. Then

$$\Psi(t) = \frac{-1}{2\pi c}\iint \frac{F'(t-2R/c)}{X_1 R}\cos^2\theta \; d\Sigma$$

$$= \frac{-1}{X_1 c}\int_{X_1}^{\infty} F'(t-2R/c)\cos^2\theta \; dR \qquad \text{(A3.48)}$$

Integrate by parts

$$\Psi(t) = \frac{-1}{X_1 c}\left\{\frac{c}{2}F(t-2X_1/c) + \frac{c}{2}\int_{X_1}^{\infty}\frac{2X_1^2}{R^3}F(t-2R/c)\,dR\right\}$$

$$= \frac{-1}{X_1 c}\left\{\int_{X_1}^{\infty}F'(t-2R/c)\,dR + c\int_{X_1}^{\infty}\frac{X_1^2}{R^3}F(t-2R/c)\,dR\right\} \qquad \text{(A3.49)}$$

But $|F'| \cong \omega_0|F|$, and $\frac{1}{R} \ll \frac{\omega_0}{c}$, hence the second term can be neglected. Thus

$$\Psi(t) = \frac{-1}{2\pi c}\iint \frac{F'(t-2R/c)}{X_1 R}\cos^2\theta \, d\Sigma$$

$$\cong \frac{-1}{2\pi c}\iint \frac{F'(t-2R/c)}{X_1 R}\, d\Sigma = \frac{F(t-2X_1/c)}{2X_1} \qquad \text{(A3.50)}$$

By an identical procedure we can show that for radiators with $\sin\theta$, $\sin\theta\sin\phi$, or $\sin\theta\cos\phi$ distributions $\Psi(t)=0$ within the same accuracy as the $\cos\theta$ distribution. $\sin\theta$ is the distribution of a vertical dipole. $\sin\theta\sin\phi$ and $\sin\theta\cos\phi$ are the complementary distributions for two perpendicular horizontal dipoles. These last three solutions

comprise a basis set for constructing arbitrary dipole solutions. By linear combinations of arbitrary dipoles, each with its own X_1, we can construct a large class of solutions. This is an important result since it means that

$$\Psi(t) = G_T(0,-)\,G_R(0,-)\,\frac{F(t-2X_1/c)}{2X_1}$$

$$\cong \frac{-1}{2\pi c}\iint G_T(\theta,\phi)\,G_R(\theta,\phi)\,\frac{F'(t-2R/c)}{X_1 R}\,d\Sigma \qquad \text{(A3.51)}$$

is a reasonable approximation for any antenna physically realizable from oscillating dipoles.

If P_T is the peak radiated power, then for the isotropic radiator over a perfect reflector

$$\Psi(t,R) = \frac{1}{R}\sqrt{\frac{PZ_0}{4\pi}}\,e^{-i\omega_0(t-R/c)} \qquad \text{(A3.52)}$$

Then

$$\Psi(t) = \frac{-1}{2\pi c}\cdot i\omega_0\iint\sqrt{\frac{P_T Z_0}{4\pi}}\cdot\frac{1}{X_1 R}\,e^{-i\omega_0\left(t-\frac{2R}{c}\right)}\,d\Sigma$$

$$= \frac{-1}{X_1 c}\cdot i\omega_0\int_{X_1}^{\infty}\sqrt{\frac{P_T Z_0}{4\pi}}\,e^{-i\omega_0\left(t-\frac{2R}{c}\right)}\,dR$$

$$= \frac{1}{2X_1}\sqrt{\frac{P_T Z_0}{4\pi}}\,e^{-i\omega_0(t-2X_1/c)} \qquad \text{(A3.53)}$$

and

$$\Psi(t)_{peak} = \frac{1}{2X_1}\sqrt{\frac{P_T Z_o}{4\pi}} \tag{A3.54}$$

and

$$P_R = (\Psi(t)_{peak})^2 \cdot \frac{\lambda^2}{4\pi} \cdot \frac{1}{Z_o}$$

$$= P_T \cdot \frac{\lambda^2}{64\,\pi^2 X_1^2} \tag{A3.55}$$

where $\lambda^2/4\pi$ is the receiving antenna's effective area (Jasik, 1961).

For the anisotropic radiator over a perfect reflector

$$P_R = G_T(0,-)\,G_R(0,-)\cdot P_T \frac{\lambda^2}{64\pi^2 X_1^2} \tag{A3.56}$$

and

$$\frac{P_R}{P_T} = \frac{\lambda^2}{4\pi}\cdot\frac{1}{Z_o}\cdot(\Psi(t)_{peak})^2$$

$$\cong \frac{\lambda^2}{4\pi}\cdot\frac{1}{Z_o}\cdot\left[\frac{1}{2\pi c}\right]^2\cdot(i\omega_o)^2\frac{Z_o}{4\pi}\cdot\left[\iint G_T G_R \frac{e^{-i\omega_o(t-2R/c)}}{X_1 R}\,d\Sigma\right]^2$$

$$= \frac{\lambda^2}{16\pi^2 X_1^2}\cdot\left[\frac{\omega_o}{2\pi c}\right]^2\cdot\left[\iint G_T G_R \frac{e^{-i\omega_o(t-2R/c)}}{R}\,d\Sigma\right]^2 \tag{A3.57}$$

For the ribbon scatterer, combining A3.57 with A3.34

$$\left[\frac{P_R}{P_T}\right]^{1/2} \cong \frac{w\lambda}{4\pi X_i^2}\cdot\frac{\omega_o}{2\pi c}\int_0^{\infty}(G_T^+G_R^+ + G_T^-G_R^-)\cos\theta\, e^{-i4\pi P}\frac{1+R_o/P}{\sqrt{(1+2R_o/P)}}\,dP$$

(A3.58)

Noting that in the nondimensionalized system $\omega_o/2\pi c=1$. Then by invoking A3.46

$$\left[\frac{P_R}{P_T}\right]^{1/2} \cong \frac{w\lambda}{4\pi X_i^2}\left|\left\{\left(\frac{1-i}{2\sqrt{2}}\right)G(\beta,\alpha_T)G(\beta,\alpha_R)\cos\beta\left[\frac{2X_i\sec\beta}{\lambda}\right]^{1/2} + \frac{1}{\pi^2}\sum_{P=1}^{\infty}J(P/8)\,e^{-i\frac{\pi}{2}P}\right\}\right|$$

(A3.59)

where the implicit dimensionless units have been included.